

Experimental and Simulation Validation Tests for MAT 213

by

Nathan Thomas Holt

A Thesis Presented in Partial Fulfillment
of the Requirements for the Degree
Master of Science

Approved July 2018 by the
Graduate Supervisory Committee:

Subramaniam Rajan, Chair
Barzin Mobasher
Christian Hoover

ARIZONA STATE UNIVERSITY

December 2018

ABSTRACT

This research summarizes the validation testing completed for the material model MAT213, currently implemented in the LS-DYNA finite element program. Testing was carried out using a carbon fiber composite material, T800-F3900. Stacked-ply tension and compression tests were performed for open-hole and full coupons. Comparisons of experimental and simulation results showed a good agreement between the two for metrics including, stress-strain response and displacements. Strains and displacements in the direction of loading were better predicted by the simulations than for that of the transverse direction.

Double cantilever beam and end notched flexure tests were performed experimentally and through simulations to determine the delamination properties of the material at the interlaminar layers. Experimental results gave the mode I critical energy release rate as having a range of 2.18 – 3.26 psi-in and the mode II critical energy release rate as 10.50 psi-in, both for the pre-cracked condition. Simulations were performed to calibrate other cohesive zone parameters required for modeling.

Samples of tested T800/F3900 coupons were processed and examined with scanning electron microscopy to determine and understand the underlying structure of the material. Tested coupons revealed damage and failure occurring at the micro scale for the composite material.

DEDICATION

To my parents, Thomas and LeeAnn Holt, for their support, guidance, and encouragement throughout my education.

ACKNOWLEDGEMENTS

I would like to thank my advisor Dr. Rajan for his help and support throughout this project. I would also like to thank my committee members Dr. Hoover and Dr. Mobasher for their teaching. I would like to thank Bilal Khaled and Loukham Shyamsunder for their immense help and mentorship. I would also like to thank Jeff Long and Peter Goguen for their help with laboratory procedures.

TABLE OF CONTENTS

	Page
LIST OF TABLES	VIII
LIST OF FIGURES	XI
CHAPTER	
1. OVERVIEW	1
1.1 Introduction	1
2. LITERATURE REVIEW	4
3. GENERAL EXPERIMENTAL TEST PROCEDURES.....	9
3.1 Sample Preparation	9
3.2 Test Machines, Fixtures, Equipment and Software.....	13
3.3 Typical Test Procedure.....	18
3.4 Post-processing of Test Data.....	18
4. STACKED-PLY EXPERIMENTAL TEST DETAILS AND RESULTS	22
4.1 Overview	22
4.2 Stacked-ply Tension Test	22
4.3 Stacked-Ply Compression Test.....	26
4.4 Stacked-ply Tension – Stress Concentration Test.....	29
4.5 Stacked-ply Compression – Stress Concentration Test.....	36
4.6 Experimental Observations	41
5. QS-RT FRACTURE MODE TEST DETAILS AND RESULTS	43
5.1 Overview	43

CHAPTER	Page
5.2 General Experimental Procedures	44
5.2.1 Sample Preparation.....	44
5.2.2 Test Machines, Fixtures, Equipment and Software	48
5.2.3 Typical Test Procedure	51
5.2.4 Post-processing of Test Data	55
5.3 Experimental Results.....	57
5.3.1 ENF Test.....	57
5.3.2 DCB Test	60
5.4 Simulation Details	67
5.5 Simulation Results.....	72
5.5.1 ENF Test.....	72
5.5.2 DCB Test	75
6. LS-DYNA SIMULATION OF QS-RT STACKED-PLY VALIDATION TESTS	
USING MAT213	79
6.1 LS-DYNA Simulation Overview	79
6.2 General Modeling Techniques	79
6.3 LS-DYNA Simulation of Stacked-ply Tension	82
6.3.1 Simulation Modeling	82
6.3.2 Validation Metrics	85
6.3.3 Results	88
6.3.4 Discussion.....	93
6.4 LS-DYNA Simulation of Stacked-ply Compression	95

CHAPTER	Page
6.4.1 Simulation Modeling	95
6.4.2 Validation Metrics	96
6.4.3 Results	97
6.4.4 Discussion.....	102
6.5 LS-DYNA Simulation of Stacked-ply Tension – Stress Concentration Test ..	102
6.5.1 Simulation Modeling	102
6.5.2 Validation Metrics	105
6.5.3 Results	109
6.5.4 Discussion.....	117
6.6 LS-DYNA Simulation of Stacked-ply Compression – Stress Concentration Test	
119	
6.6.1 Simulation Modeling	119
6.6.2 Validation Metrics	120
6.6.3 Results	122
6.6.4 Discussion.....	131
7. SEM IMAGING FOR MAT213 MODEL VALIDATION.....	133
7.1 Objective	133
7.2 Procedure.....	134
7.3 Results	140
7.3.1 Virgin Sample.....	140
7.3.2 Damaged Sample.....	143
7.3.3 Failed Sample	145

CHAPTER	Page
7.3.4 Failed – Shear Sample	150
8. CONCLUDING REMARKS.....	154
REFERENCES	155

LIST OF TABLES

Table	Page
1.1. T800/F3900 Manufacturer Reported Material Properties	1
3.1. Waterjet Specifications	9
3.2. 80-Grit (US Std) Specifications	9
3.3. Grinding Wheel Specifications	10
3.4. 46 Grit (Grinding Wheel) Specifications	10
3.5. Descriptions of the Parameters Used in this Report	20
4.1. Tension Test Specimen Dimensions	22
4.2. Summary of Tension Test Results	24
4.3. Compression Test Specimen Dimensions.....	26
4.4. Summary of Compression Test Results.....	28
4.5. Tension Stress Concentration Test Specimen Dimensions.....	30
4.6. Summary of Tension Stress Concentration Test Results	33
4.7. Compression Stress Concentration Test Specimen Dimensions	36
4.8. Summary of Compression Stress Concentration Test Results.....	38
5.1. MAT 138 Parameter Summary	44
5.2. ENF Test Specimen Dimensions	57
5.3. Test Summary for ENF Non-precracked Tests.....	59
5.4. Test Summary for ENF Precracked Tests.....	59
5.5. ENF Experimental Regression Specifications	60
5.6. DCB Test Specimen Dimensions.....	61

Table	Page
5.7. DCB Experimental Regression Specifications	64
5.8. Test Summary for DCB Non-precracked Tests	64
5.9. Test Summary for DCB Precracked Tests – Non-linear.....	64
5.10. Test Summary for DCB Precracked Tests – Visible	65
5.11. Test Summary for DCB Precracked Tests – Maximum	65
5.12. ENF and DCB Meshes.....	69
5.13. ENF and DCB Simulation Specifications.....	71
5.14. Simulation Regression Specifications.....	74
5.15. Final Mode II MAT 138 Parameters.....	74
5.16. Simulation Regression Specifications.....	77
5.17. Final Mode I MAT 138 Parameters	77
5.18 MAT138 Input Deck.....	78
6.1. Model Parameter Specifications	80
6.2. FE Model Meshes	84
6.3. Validation Metrics Description.....	85
6.4. Tension Test Metric 1	86
6.5. Tension Test Metric 2	86
6.6. Tension Test Metric 3	87
6.7 Polynomial Regression Fitting of Tension Simulation Metrics.....	94
6.8. FE Model Meshes	95
6.9. FE Model Meshes	104
6.10. Validation Metrics Description.....	108

Table	Page
6.11. Tension Hole Test Metric 1	108
6.12. Tension Hole Test Metric 2	108
6.13. Tension Hole Test Metric 3	109
6.14 Polynomial Regression Fitting of Tension with Hole Simulation Metrics	117
6.15. FE Model Meshes	119
6.16. MAT213 Specifications	122
6.17 Polynomial Regression Fitting of Compression with Hole Simulation Metrics.....	131
7.1. SEM Image Samples.....	133
7.2. Grinding and Polishing Procedure	138

LIST OF FIGURES

Figure	Page
1.1. Microscopy images of T800/F3900 (a) SEM 3600x (b) SEM 65x (c) Optical 1500x (d) Optical 200x	2
1.2. Stacked-ply layup.....	2
3.1. Optical microscopy images of finished edges (after grinding) (a) 200x, (b) 400x, (c) 500x, (d) 1000x.....	11
3.2. Close up of a typical speckled surface	13
3.3. Experimental equipment (a) Test frame, (b) Hydraulic grips,(c) CLC compression fixture top, and (d) CLC fixture front	14
3.4. (a) Two DIC cameras and high-speed camera (b) LED lighting fixture	15
3.5. Typical SGS (a) Tension specimens (b) Compression specimens.....	16
3.6. Dual DIC systems setup.....	17
3.7. Strain measurement areas for stress concentration tests	19
4.1. Typical specimen geometry and layout (all dimensions in inches)	22
4.2. Example image of tension specimen prior to testing	23
4.3. Tension specimens after testing (a)(b)(c) V-T-4, (d)(e)(f) V-T-5, (g)(h)(i) V-T-6 ...	24
4.4. Tension stress-strain curves	25
4.5. Typical specimen geometry and layout (all dimensions in inches)	26
4.6. Compression specimens prior to testing (a) V-C-2, (b) V-C-3, (c) V-C-4	27
4.7. Compression specimens after testing (a) V-C-2 XY surface (b) V-C-2 through thickness (c) V-C-3 XY surface (d) V-C-3 through thickness	28

Figure	Page
4.8. Compression stress-strain curves	29
4.9. Typical specimen geometry and layout (all dimensions in inches)	30
4.10. Compression specimens prior to testing (a) V-TH-2, (b) V-TH-3, (c) V-TH-4	31
4.11. Tension Stress Concentration specimens after testing (a)(b)(c) V-TH-2, (d)(e)(f) V-TH-3, (g)(h)(i) V-TH-4	33
4.12. Tension stress concentration RL of hole ϵ_{yy} vs. time	34
4.13. Tension stress concentration: above hole ϵ_{xx} vs. time	35
4.14. Tension stress concentration: below hole ϵ_{xx} vs. time	35
4.15. Typical specimen geometry and layout (all dimensions in inches)	36
4.16. Compression specimens prior to testing (a) V-CH-5, (b) V-CH-7, (c) V-CH-8	37
4.17. Compression Stress Concentration specimens after testing (a)(b)(c) V-CH-5, (d)(e)(f) V-CH-7, (g)(h)(i) V-CH-8	38
4.18. Compression stress concentration RL of hole ϵ_{yy} vs. time	39
4.19. Compression stress concentration: above hole ϵ_{xx} vs. time	40
4.20. Compression stress concentration: below hole ϵ_{xx} vs. time	40
5.1. Traction-separation law used in MAT 138 [31]	43
5.2. ENF and DCB manufactured boards showing test coupons cut from the original panel	45
5.3. Piano hinges for DCB test	45
5.4. Test machines and fixtures (a) MTS load frame (b) Spring loaded grips front view (c) Spring loaded grips side view (d) 3-point bend fixture	49

Figure	Page
5.5. Typical camera setup for ENF and DCB tests, Tokina 100 mm lens (top) and Schneider 35 mm lens (bottom).....	50
5.6. Tokina 100 mm lens on Point Grey Grasshopper 3 camera	51
5.7. DCB test setup [12].....	51
5.8. DCB test.....	52
5.9. ENF 3-point test setup [33].....	54
5.10. ENF test	55
5.11. Y-displacement DIC data for DCB test	56
5.12. COD tool on ENF specimen	56
5.13. COD tool on DCB specimen.....	57
5.14. Typical specimen geometry and layout	57
5.15. Example image of ENF specimen prior to testing (a) Top surface showing specimen width (b) Side of specimen showing thickness.....	58
5.16. Example image of ENF specimen after testing (a) Top surface showing specimen width (b) Side of specimen showing thickness.....	58
5.17. ENF precrack experimental force vs. displacement	60
5.18. Typical specimen geometry and layout	61
5.19. Example image of DCB specimen prior to testing (a) Top surface showing specimen width (b) Side of specimen showing thickness.....	62
5.20. Example image of DCB specimen after testing (a) Exterior top and bottom surfaces (b) Interior surfaces (c) Film (d) Initial crack area	63
5.21. DCB precrack experimental force vs. displacement.....	63

Figure	Page
5.22. DCB tests crack resistance curve	66
5.23. GIC versus crack tip opening displacement.....	67
5.24. ENF experimental geometry and BC's	68
5.25. ENF simulation geometry and BC's	68
5.26. DCB experimental geometry and BC's	69
5.27. DCB simulation geometry and BC's	69
5.28. DCB Mesh 1 - 1 cohesive zone layer.....	70
5.29. DCB Mesh 4 - 23 cohesive zone layers	71
5.30. Mode II sensitivity study (a) ET (b) S	72
5.31. Force vs. displacement simulation and experimental comparison.....	73
5.32 Mode II Final Traction Separation Curve	74
5.33. Mode I sensitivity study (a) EN (b) T	75
5.34. Force vs. displacement simulation and experimental comparison.....	76
5.35 Mode I Final Traction Separation Curve	77
6.1. Elevation XZ plane view of the FE model.....	80
6.2. Energy plot for tension simulation.....	81
6.3. Experimental test conditions, XY plane	83
6.4. Experimental test conditions, YZ plane.....	83
6.5. Simulation test conditions, XY plane	84
6.6. Simulation test conditions, YZ plane.....	84
6.7 VIC 3D digital extensometers used for metric 2	87
6.8. Metric 3 y-reaction nodes	88

Figure	Page
6.9. Metric 1 - ϵ_{xx} comparison.....	89
6.10. Metric 1 - ϵ_{yy} comparison.....	89
6.11. Metric 2 - x-displacement comparison	90
6.12. Metric 2 - y-displacement comparison	91
6.13. Metric 3 - stress-strain comparison.....	92
6.14. Y-Strain fringe plot of tension test, at $t = 250$ s (a) Simulation (b) Experiment	93
6.15. Compression comparison node and element.....	97
6.16. Metric 1 - ϵ_{xx} comparison.....	98
6.17. Metric 1 - ϵ_{yy} comparison.....	98
6.18. Metric 2 - x-displacement comparison	99
6.19. Metric 2 - y-displacement comparison	99
6.20. Metric 3 - stress-strain comparison.....	100
6.21. Y-Strain fringe plot of compression test, at $t = 150$ s (a) Simulation (b) Experiment	101
6.22. Experimental test conditions, XY plane	103
6.23. Experimental test conditions, YZ plane.....	103
6.24. Simulation test conditions, XY plane	104
6.25. Simulation test conditions, YZ plane.....	104
6.26. Coarse mesh validation measurement locations	106
6.27. Medium mesh validation measurement locations.....	106
6.28. Fine mesh validation measurement locations	107
6.29. DIC measurement areas	107

Figure	Page
6.30. Metric 1 - ϵ_{xx} comparison.....	110
6.31. Metric 1 - ϵ_{yy} comparison.....	110
6.32. Metric 1 - ϵ_{xy} comparison.....	111
6.33. Metric 2 - above hole ϵ_{xx} comparison	111
6.34. Metric 2 - above hole ϵ_{yy} comparison	112
6.35. Metric 2 - above hole ϵ_{xy} comparison	112
6.36. Metric 2 - below hole ϵ_{xx} comparison.....	113
6.37. Metric 2 - below hole ϵ_{yy} comparison.....	113
6.38. Metric 2 - below hole ϵ_{xy} comparison.....	114
6.39. Metric 3 - x-direction displacement.....	115
6.40. Metric 3 - y-direction displacement.....	115
6.41. Y-Strain fringe plot of tension-hole test, at $t = 325$ s (a) Simulation (b) Experiment	117
6.42. Coarse mesh validation measurement locations	121
6.43. Medium mesh validation measurement locations.....	121
6.44. Fine mesh validation measurement locations	122
6.45. Metric 1 - ϵ_{xx} comparison.....	123
6.46. Metric 1 - ϵ_{yy} comparison.....	123
6.47. Metric 1 - ϵ_{xy} comparison.....	124
6.48. Metric 2 - above hole ϵ_{xx} comparison	125
6.49. Metric 2 - above hole ϵ_{yy} comparison	125
6.50. Metric 2 - above hole ϵ_{xy} comparison	126

Figure	Page
6.51. Metric 2 - below hole ϵ_{xx} comparison.....	127
6.52. Metric 2 - below hole ϵ_{yy} comparison.....	127
6.53. Metric 2 - below hole ϵ_{xy} comparison.....	128
6.54. Metric 3 - x-direction displacement.....	129
6.55. Metric 3 - y-direction displacement.....	129
6.56. Y-Strain fringe plot of compression-hole test, at $t = 155$ s (a) Simulation (b) Experiment.....	131
7.1. Epoxy set components (a) Resin (b) Hardener	135
7.2. Epoxy embedding equipment (a) Vacuum chamber (b) Sample holder.....	136
7.3. Grinding and polishing equipment (a) Allied machine specimen holder (b) Allied machine	137
7.4. Polishing materials (a) RedLube (b) Diamond suspension (c) Colloidal silica suspension.....	137
7.5. Example of half polished specimen	139
7.6. SEM imaging equipment (a) XL30 ESEM FEG (b) Sputter coater	140
7.7. Virgin sample before cutting	141
7.8. Virgin sample cutting layout.....	141
7.9. Virgin sample 500x.....	142
7.10. Virgin sample (a) 3500x (b) 5000x.....	142
7.11. Virgin sample (a) 5000x (b) 6500x.....	143
7.12. Damaged sample before cutting.....	144
7.13. Damaged sample cutting layout.....	144

Figure	Page
7.14. Damaged sample (a) 800x (b) 5000x	144
7.15. Damaged sample (a) 2500x (b) 6500x	145
7.16. Failed sample before cutting (a) Width (b) Through thickness	146
7.17. Failed sample cutting layout	146
7.18. Failed sample 36x damage away from complete fracture zone	147
7.19. Failed sample (a) 250x (b) 50x	148
7.20. Failed sample (a) 36x (b) 250x	148
7.21. Failed sample (a) 250x (b) 2000x	149
7.22. Failed sample (a) 1000x (b) 3500x	149
7.23. Failed-shear sample before cutting (a) Whole specimen (b) Gage area	150
7.24. Failed-shear sample cutting layout	151
7.25. Failed-shear sample (a) 36x (b) 650x	151
7.26. Failed-shear sample (a) 1200x (b) 1200x	152
7.27. Failed-shear sample (a) 40x (b) 1000x	153

1. Overview

1.1 Introduction

This document summarizes (a) the experimental procedures and results obtained from testing various structural forms of the T800-F3900 composite material manufactured by Toray Composites, Seattle, WA, and (b) numerical simulation of these tests using the MAT213 material model implemented in the LS-DYNA finite element program [MAT213 V1.3a-1]. The tests were performed at quasi-static (QS) and room temperature (RT) conditions and include stacked-ply tension and compression tests, as well as fracture mode analysis tests. Details of the MAT213 material model and its implementation in LS-DYNA are available publicly (Goldberg et al. [1]; Harrington et al. [2]; and Hoffarth et al. [3]) and are not duplicated in this report.

The material properties reported by Toray Composites are shown in Table 1.1 and are the averages of multiple replicates.

Table 1.1. T800/F3900 Manufacturer Reported Material Properties

Characteristic	Reported Value
Resin Content Beginning (%)	34.8
Resin Content Ending (%)	35.4
Ultimate Tensile Strength (psi)	434 000
Tensile Modulus (psi)	22 000 000
Tensile Strain at Failure (in/in)	0.0177
Ultimate Compressive Strength (psi)	214 000

The structure of the composite is shown in Fig. 1.1. The images show the composite at varying levels of magnification with Fig. 1.1(a) and (b) captured using a Scanning Electron Microscope (SEM) and Fig. 1.1(c) and (d) captured using optical microscopy. The images depict the fibers, matrix, and the interlaminar layers.

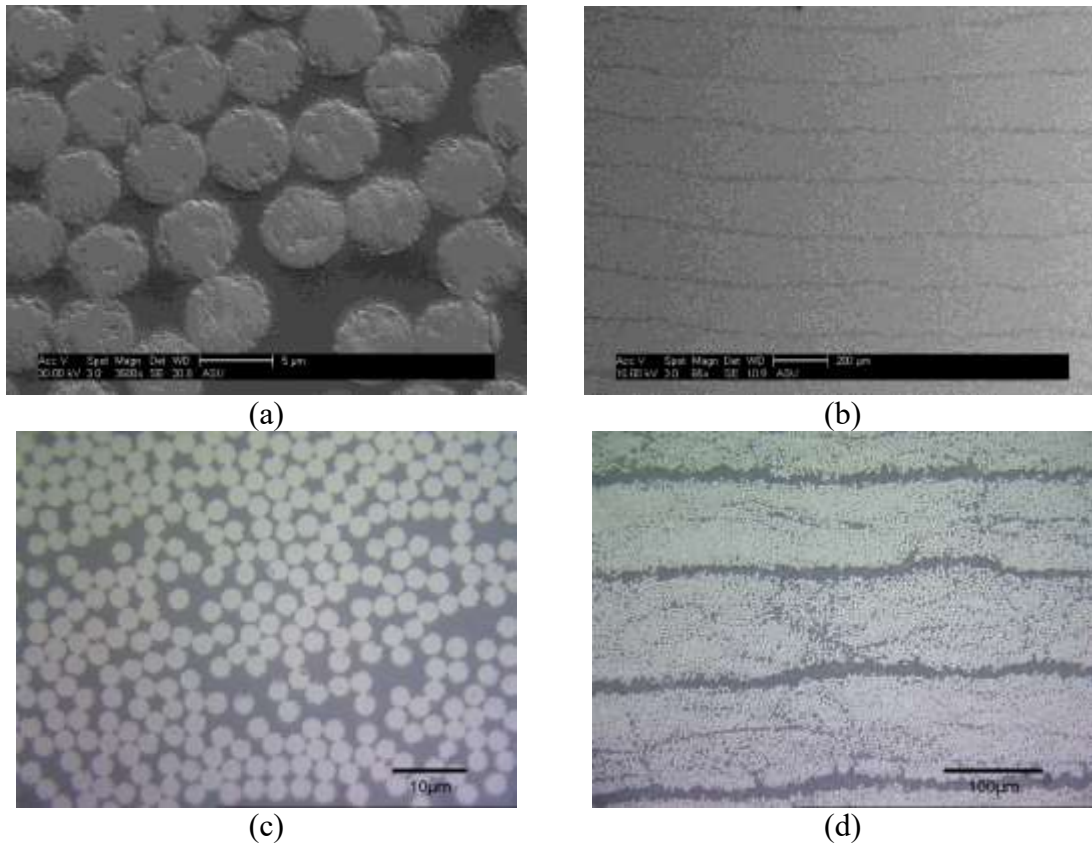


Fig. 1.1. Microscopy images of T800/F3900 (a) SEM 3600x (b) SEM 65x (c) Optical 1500x (d) Optical 200x

All stacked-ply validation tests had a laminate lay-up that was $[0/90/45/-45]_s$. The 8-ply layup is shown in Fig. 1.2.

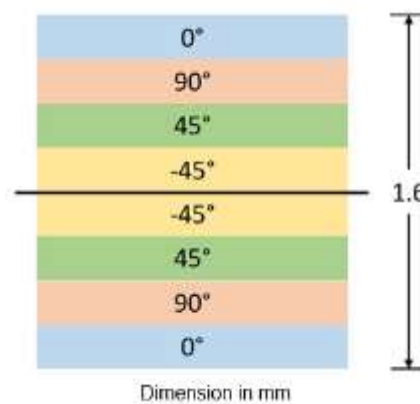


Fig. 1.2. Stacked-ply layup

Four types of stacked-ply validation tests were performed: tension, compression, open-hole tension, and open-hole compression. Dimensions of the test coupons were specific to the type of test performed. These tests served to provide validation data for MAT213's deformation, damage, and failure sub-models. The tension and compression tests validated the model's ability to predict stress-strain relationships for simple geometries, while the stress concentration tests provided validation for more complicated geometries.

Two types of fracture analysis tests were conducted - the end notched flexure test (ENF) and the double cantilever beam test (DCB). Results from these tests are used in developing and calibrating the cohesive zone models (CZM) that were used to characterize composite delamination in the validation tests.

Additionally, an examination of damaged and failed specimens was performed using a scanning electron microscope. The study helped in gaining an understanding of the microstructure of the composite.

2. Literature Review

Stacked-ply Validation

The use of stacked-ply coupons to compare results with virtual models of fiber-reinforced composites under quasi-static loading conditions has been shown to be a reliable method of model validation. Bruyneel et al. [4] discuss the development of a damage model formulated in SAMCEF, a finite element analysis software, in which they use stacked-ply coupons to validate their model. Using stress-strain curves, based on both longitudinal and transverse strains, they compared simulation and experimental results. The same metric was used by Ladeveze and LeDantec [5] in their stacked-ply validation of a continuum damage mechanics theory.

Open-hole tests have also been used as validation tests for predicting the response of stacked-ply coupons. Achard et al. [6] used open hole tension tests for validating their method of Discrete Ply Modeling, a study in which they compared normalized stress-strain in the longitudinal direction as well as failure patterns and delamination around the hole. In similar fashion, Clay and Knoth [7] used stacked-ply, open-hole compression and tension tests to evaluate composite progressive damage analysis methods. In this study, bulk stiffness and strength are used as comparison metrics between simulated and experimental data. In addition, x-ray tomography radiographs are used to evaluate damage and failure of the test coupons near the hole.

Fracture Mode Tests

The double cantilever beam (DCB) and end notched flexure (ENF) test are well established methods of characterizing fracture in both mode I and mode II fracture,

respectively. While these tests have proven to be very useful, an understanding of their deficiencies is critical to analyzing the results of these tests.

The use of the ENF test alone for mode II fracture has a few disadvantages. Zabala et al. [8] state that the mode II strain energy release rate is typically characterized by four tests - the ENF, stabilized end notched flexure (SENF), end loaded split (ELS) and four point bend end notched flexure (4ENF). Kageyama et al. [9] describe a limitation of the ENF test in that crack growth is unstable during the test, thus the test will not produce an R-curve but will only yield an initiation value of the strain energy release rate. In addition to unstable crack growth, Schuecker and Davidson [10] studied the effect of friction in the ENF and 4ENF tests. The authors concluded that though friction effects were larger for the traditional ENF test, it was insignificant in both tests and the differences between the results of the ENF and 4ENF were due to other experimental factors.

O'Brien et al. [11] used ENF tests to characterize mode II interlaminar fracture toughness of rotorcraft material. In this study they followed ASTM standards to produce results for both non-precracked and precracked specimens. For their study, the authors used a polytetrafluoroethylene film at the mid-plane of a specimen to act as the source of initial delamination.

ASTM D5528 [12] on the DCB test describes four methods for calculating the strain energy release rate including modified beam theory, rotation corrected modified beam theory, compliance calibration, and modified compliance calibration. Yoshihara and Satoh [13] described these methods and their use in correcting the crack tip deformation. In order to use the modified beam theory, it is important that the strain

energy release rate be uniform along the entire crack front. Sun and Zheng [14] studied the role of the ply layup in creating a uniform strain energy release front at the crack tip and recommended a repeated 0° -ply layup.

A study by Nandakumar [15] on rate effects on interlaminar fracture toughness included the T800/F3900 composite. This study found a mode I fracture toughness of 2.5 to 5 lb/in including a decrease with increasing displacement rate and a mode 2 fracture toughness of 9 to 20 lb/in including an increase with increasing displacement rate. The study also found that fiber bridging had lesser effect with lower displacement rates. Tamuzs et al. [16] studied the effect of fiber bridging on double cantilevered beam specimens and found that fiber bridging can have a significant impact on the later stages of the traction-separation law.

Existing studies have shown that there are multiple ways to model interlaminar layers of fiber-reinforced composites, and the use of cohesive zone elements has proven to be effective. Wasseem and Kumar [17] produced one such study in which cohesive zone elements were used to model the delamination zone for the double cantilevered beam test. The use of the DCB and ENF tests to calibrate the parameters of cohesive zone elements has been studied and used effectively. On a commercial level, Veryst Engineering [18] employs the use of model calibration to get the properties of the interlaminar layer of composites from DCB and ENF tests. They use load and displacement data from experimental tests to produce the traction-separation law of these materials.

While calibration using experimental data has proven to be effective, a new procedure to get the traction-separation law developed by Arrese et al. [19] could be used. The procedure developed by the authors of this study employs an analytical approach to directly obtain strain energy release rate, crack opening displacement, and, by way of differentiation, the traction-separation law from experimental data. This approach, however, was only shown for the double cantilevered beam test.

Many existing studies have found success using a bilinear model of the traction-separation law for both the DCB and ENF models. Meo and Thieulot [20] produced one such study in which they used a bilinear softening model in DYNA3D to model the cohesive elements for a double cantilevered beam specimen.

SEM Imaging

In order to efficiently identify types and extent of damage to the fiber-reinforced material, an understanding of the formulation and types of micro damage in these materials was needed. In a study on fatigue damage mechanisms on thermoset and thermoplastic composites, Jollivet et al. [21] discussed the progression of damage in these materials. They explained that the first damage to occur requires low energy consumption, primarily interface and matrix failure, while higher energy damage such as fiber breakages occur later. The authors also described the development of intralaminar and interlaminar cracks.

Other studies showed SEM images of failed or damage specimens, which gave insight on what specific types of damage typically looked like using a SEM. Llorca et al. [22] produced a study on modeling composites at all scales and SEM images of damaged

specimens. This study showed images of fiber interface decohesion as well as formation of matrix damage.

To produce quality SEM images of the composite material depicting the level of damage and types of failure in each specimen, other studies with SEM images were sought out to develop strategies for imaging. One such study, by Li et al. [23] showed that a voltage of 20 kV produced good images of carbon fibers, among other SEM settings and methods they used.

3. General Experimental Test Procedures

3.1 Sample Preparation

Waterjet was used to cut the test coupons. The waterjet specifications are shown in Table 3.1. The cut speed used for the validation test samples was Quality 3.

Specifications of the abrasive used in the waterjet are shown in Table 3.2. Additionally, when necessary, the waterjet cut edges were ground using a grinding wheel matching the specifications shown in Table 3.3. Particle size statistics of the abrasive used on the grinding wheel are shown in Table 3.4. Test samples were generated with planar cut, smooth edges, and free of any visible damage.

Table 3.1. Waterjet Specifications

Specification	8-ply Samples
Approximate Thickness (in)	0.125
Abrasive Size (grit)	80 (US Std)
Nozzle Diameter (in)	0.03
Minimum Nozzle Pressure (psi)	30000
Maximum Nozzle Pressure (psi)	45000
Cut Speed (in/min)	
Quality 1	135.43
Quality 2	116.15
Quality 3	72.87
Quality 4	52.34
Quality 5	40.5

Table 3.2. 80-Grit (US Std) Specifications

Sieve Size (US Std)	Sieve Mesh Diameter (in)	% Retained
8	0.0937	0
12	0.0661	0
14	0.0555	0
16	0.0469	0
20	0.0331	0
30	0.0234	0
40	0.0165	0-5

50	0.0117	10-35
60	0.0098	20-40
80	0.007	20-50
120	0.0049	0-15
Pan	-	0-3

Table 3.3. Grinding Wheel Specifications

Frequency of Rotation (rpm)	~3500
Abrasive Grit (grit)	46 (US Std)
Tolerance (in)	± 0.005
Operation	Manual

Table 3.4. 46 Grit (Grinding Wheel) Specifications

Minimum Particle Size (in)	0.0095
Maximum Particle Size (in)	0.022
Average Particle Size (in)	0.014

Fig. 3.1 shows cross-sectional images of a typical cut sample captured using an optical microscope under various magnifications.



(a)



(b)



(c)



(d)

Fig. 3.1. Optical microscopy images of finished edges (after grinding) (a) 200x, (b) 400x, (c) 500x, (d) 1000x

When required, G10 FR4 fiberglass tabs¹ were used with the sample. The fiberglass tabs acted as compliant surfaces that prevented specimens from crushing when placed in the test frame hydraulic grips. The tabs were bonded to the specified specimen surfaces using a two-part epoxy adhesive.

3M DP460 Scotch Weld toughened two-part epoxy² was used to bond fiberglass tabs to the specimens. In an earlier study [24], the guidelines set forth in ASTM D3528-96 were used to carry out the adhesive strength study using a double lap shear test. This study proved the DP460 epoxy had an adequate bond strength with G10 fiberglass.

All stacked-ply specimens were prepared in the same manner unless otherwise noted. The following list outlines the steps taken to fully prepare the specimens for testing.

1. The regions on a typical specimen where fiberglass tabs were bonded, and the surfaces of the fiberglass tabs being bonded to the specimen were lightly sanded using 120 grit sandpaper. Sanding the surfaces ensured a complete bond between the specimen and the tabs.
2. The surfaces that were sanded, were then cleaned using cotton swabs soaked with isopropyl alcohol. The surfaces were allowed to air dry until there was no visible moisture on the bonding surfaces.

¹ G10, FR4 Laminate Sheets 36"x 48", Epoxyglas™; NEMA Grade FR4, Mil-I-24768/27, <http://www.accum.com/>

²<http://multimedia.3m.com/mws/media/66122O/3mtm-scotch-weld-tm-epoxy-adhesive-dp460-ns-and-off-white.pdf>

3. The 3M epoxy was mixed in accordance to the manufacturer's recommendation.
A thin layer of the mixed epoxy was applied to the prepared surface of the tabs using a wooden applicator.
4. The tabs were then placed on the specimen and positioned until the surfaces of the specimen and the tabs were in complete contact and aligned properly in the desired region.
5. The specimens were allowed to cure at room temperature and atmospheric pressure for 24 hours.
6. Next, the gage region of the specimen was painted and speckled. Speckling of the specimen involved first spraying the surface of the specimen with a layer of white paint with a flat finish. Paint was sprayed onto the surface until the specimen could no longer be seen. The paint was allowed to completely dry at room temperature.
7. After the white paint dried, black paint, with a flat finish, was sprayed onto the dry white paint. The black paint was sprayed in a manner which resulted in random array of black dots being deposited on the white area of the specimen.
8. After painting the specimens, they were allowed to finishing curing for another 24 hours as recommended by the manufacturer. A close up of a typical speckled surface is shown in Fig. 3.2.



Fig. 3.2. Close up of a typical speckled surface

3.2 Test Machines, Fixtures, Equipment and Software

All stacked-ply validation experiments were performed using the same test frame and a similar camera system. Post processing of the experimental images was performed using the same software as described next.

Test Frame: The experimental procedures for the stacked-ply tests were performed using an MTS 810 universal testing frame (Fig. 3.3(a)). Flat tension specimens were held in the frame with MTS 647.10A hydraulic grips (Fig. 3.3(b)). The hydraulic grips were aligned by clamping a rigid, flat steel plate and allowing the heads to freely rotate into position. After aligning the hydraulic grips, the specimen was placed into the test frame. The specimen was gripped up to the end of the fiberglass tabs. Compression specimens were tested using a Wyoming Test Fixtures combined loading compression fixture (CLC) as shown in Fig. 3.3(c) and Fig. 3.3(d). The CLC fixture transfers load into the compression specimens through both shear load transfer and end load transfer, thus decreasing the need for large clamping forces.

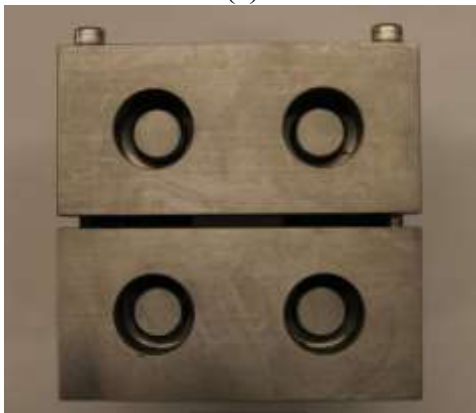
Force data was gathered using an MTS 661.21A-03 load cell. All experiments were performed under displacement control conditions. The displacement rate refers to the rate of displacement of the test frame actuator and was set using the MTS system controller.



(a)



(b)



(c)



(d)

Fig. 3.3. Experimental equipment (a) Test frame, (b) Hydraulic grips, (c) CLC compression fixture top, and (d) CLC fixture front

Digital Image Correlation (DIC) Equipment: Two Point Grey Grasshopper 3³ cameras were used to capture images of the specimen throughout the duration of the experiment as shown in Fig. 3.4(a). LED lamps were used to properly illuminate the specimen during the experiment. The cameras and lights were fixed to the same frame (Fig. 3.4(b)). The frame was leveled using a bubble level in order to ensure the field of view of the cameras was both horizontal and vertical respectively. A high-speed camera was used to capture the specimen state at the moment of failure (Fig. 3.4(a)). Unless otherwise noted, images were captured at five second intervals throughout the experiment using Vic-Snap 8 [25].



(a)



(b)

Fig. 3.4. (a) Two DIC cameras and high-speed camera (b) LED lighting fixture

Post Processing: The images captured during the experiment were processed to obtain full strain field using Vic-3D v7 [25] software system. The Lagrangian definition of

³ <https://www.ptgrey.com/grasshopper3-gige-vision-cameras>

strain was chosen to perform the analysis. Vic-3D software was used to smooth the strain data using a decay filter algorithm. For the initial processing, the entire speckled region of the specimen was analyzed. After the analysis and smoothing were completed, a smaller region with constant strain was taken as the representative strain induced in the specimen during the experiment. The region of interest was typically chosen so that the strain field was as uniform in that region as possible. Typically, this region is away from the edges of the specimen and away from areas of strain concentrations that may have been present where the specimens were gripped. In this report, this area or region (from which the strain values are obtained and reported) is referred to as the *strain gage section* (SGS). Sample images showing various SGS are shown in Fig. 3.5.

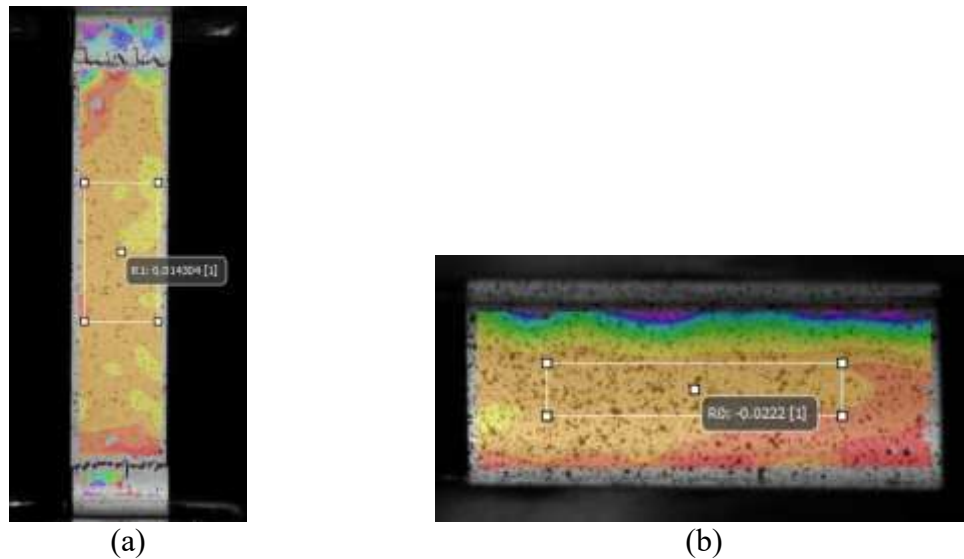


Fig. 3.5. Typical SGS (a) Tension specimens (b) Compression specimens

The tension tests were performed using a dual DIC setup that allowed images on two faces of the specimen to be captured. Two sets of two Point Grey Grasshopper 3 cameras and LED lights were positioned on either side of the testing frame and directed at the specimen. The resulting images from one side were labeled as System 1 (*Sys1*) and those

from the other side were labeled as System 2 (*Sys2*). The goal of this dual system was to measure the strains on two opposite faces of the test specimen to identify the extent of variability between the strains of the two sides. This variability would indicate the extent to which the samples may have been warped during the manufacturing process or misaligned in the test fixture. Post processing of *Sys1* and *Sys2* data was completed independently. The dual DIC setup is shown in Fig. 3.6.

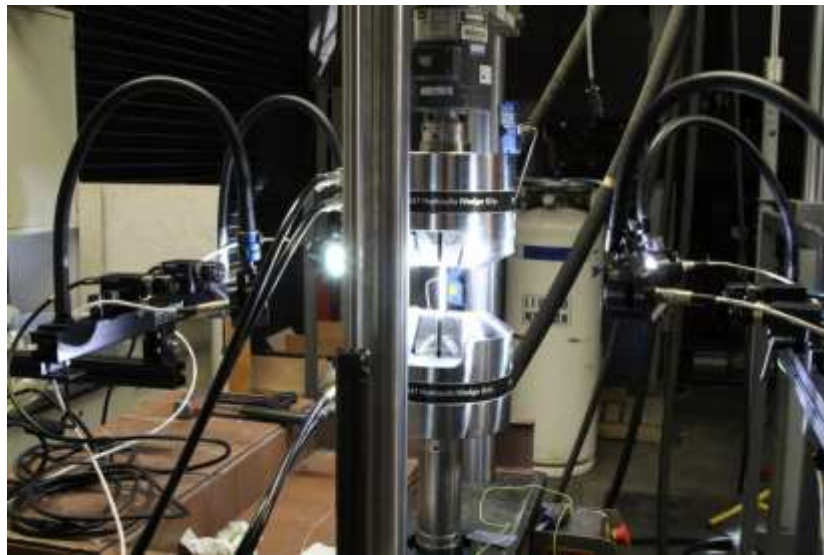


Fig. 3.6. Dual DIC systems setup

Measurement Instruments: Several instruments were used to obtain specimen dimensions, specimen mass, and optical microscope images. Specimen dimensions were measured using a Pittsburgh 4” Digital Caliper⁴. The caliper has a resolution of 0.0005 in. All optical microscopy images were obtained using an Olympus MX50 optical microscope⁵.

⁴ <https://www.harborfreight.com/4-inch-digital-caliper-47256.html>

⁵ <https://www.olympus-ims.com/en/service-and-support/obsolete-products/>

3.3 Typical Test Procedure

The procedure for conducting experiments are the same for each specimen unless otherwise noted. For all experiments, prior to loading the specimen, the DIC system was calibrated using Vic 3D v7 software system. Calibration was done only when the cameras were moved, or when the use of new fixtures would cause the plane of the specimen to be different from when the cameras were calibrated. All experimental tests were conducted under displacement-controlled conditions.

3.4 Post-processing of Test Data

Force data was obtained as a function of time from the MTS controller, and strain data was obtained as a function of time from DIC analysis. The stress in the specimen was taken as the average stress across the respective cross section of the specimen. For tension and compression specimens, the cross section perpendicular to the direction of loading was used to calculate the cross-sectional area. The average stress was calculated as

$$\sigma = \frac{F}{A} \quad (3.1)$$

where F is the normal force reported by the load cell at the current time-step and A is the initial cross-sectional area. The strain reported from Vic 3D v7 in the region of interest was used in conjunction with the calculated stress to generate an engineering stress-strain curve for any given specimen.

Post-processing of test data was handled differently for the stress concentration experiments. The purpose of these tests was primarily in evaluating the ability of MAT213 to predict strain concentrations. For these experiments, strain vs. time plots

were used as part of the validation process with these plots being constructed for several regions within the gage area. An example of the areas where strain was measured and analyzed is shown in Fig. 3.7.

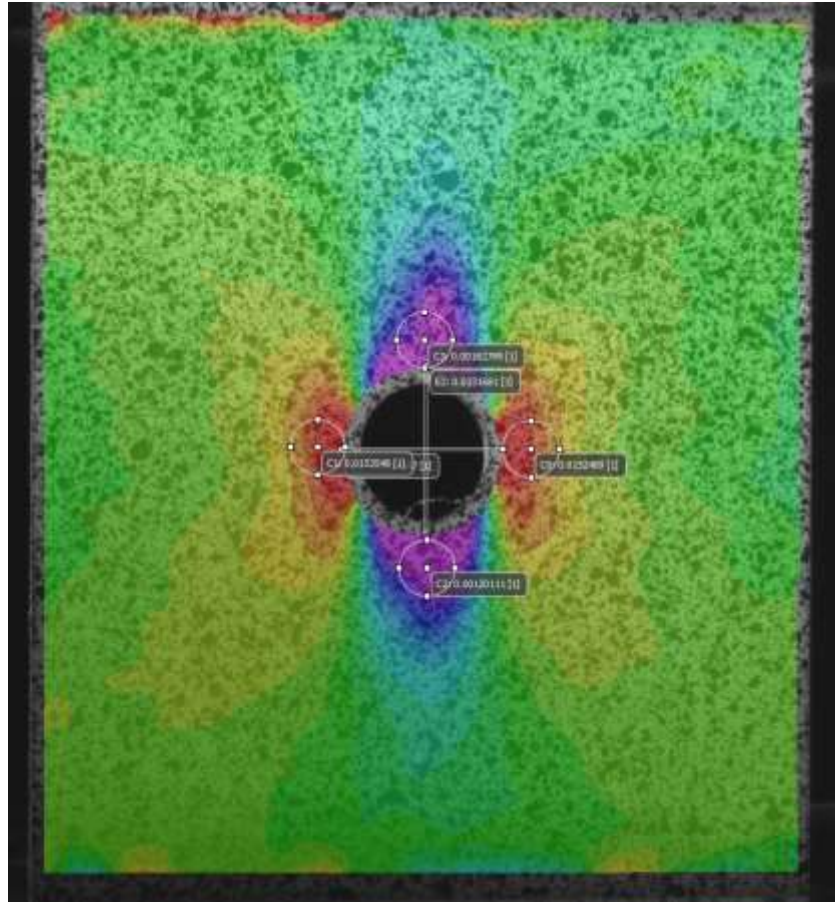


Fig. 3.7. Strain measurement areas for stress concentration tests

There were three areas where SGS's were used to capture strain data - directly to the left and right of the hole, above the hole (top), and below the hole (bottom). Strain data from the left and right of the hole is always averaged together and represented by the abbreviation *RL*. The area above the hole is synonymous with “top” in this report and is abbreviated by *T*. The area below the hole is synonymous with “bottom” in this report and is abbreviated by *Bot*. Data from the right and left areas was averaged because of

symmetry along the vertical axis of the test for the geometry and loading condition. The top and bottom areas were not averaged because the loading was not symmetric about the horizontal axis as shown in Fig. 3.7. In the test frame, the top grip was fixed while the bottom fixture was subjected to a displacement-controlled condition.

In addition to the stress-strain curve, several parameters were obtained from the stress-strain curves of each individual specimen to determine how consistent the data is.

Table 3.5 describes each parameter and how they were obtained.

Table 3.5. Descriptions of the Parameters Used in this Report

Parameter	Definition	Method
Loading rate	Constant rate at which the actuator on the test frame is displaced.	Chosen by the experimenter as a fixed parameter at the beginning of the procedure. The rate is prescribed as a displacement over a certain period of time.
Strain rate	The rate at which strain is induced in the specimen during a given experiment.	The strain measure of interest is plotted as a function of time and the average strain rate during the experiment is obtained by performing a linear regression. The slope of the resulting best fit line is taken as the average strain rate.
Modulus, E	The slope of the initial linear region of the true stress-strain curve.	The analyst determines the region in the initial portion of the curve and performs a linear regression. The slope of the resulting best fit line is taken as the modulus.
Peak stress	Maximum stress achieved during a given experiment.	Selected from stress data obtained through scaling the force data reported by the load cell.
Ultimate strain	Strain measured at peak stress.	Selected as the largest strain when the specimen exhibits brittle failure with no post-peak strength.
Failure strain	Strain measured when the specimen fails.	Selected as the strain when there is a large drop in stress and the specimen no longer loads back up to that peak stress point. Typically, this occurs when the test is terminated and is used when specimen does not exhibit brittle failure.
Transverse strain	Strain induced in the specimen perpendicular to the direction of loading in tension and compression tests.	Obtained through DIC measurements.

Longitudinal strain	Strain induced in the specimen parallel to the direction of loading in tension and compression tests.	Obtained through DIC measurements.
---------------------	---	------------------------------------

Throughout this report, “EXP” refers to experimental tests and “SIM” refers to LS-DYNA simulations.

4. Stacked-Ply Experimental Test Details and Results

4.1 Overview

Details of each test are discussed in this section. Applicable ASTM standards were used for experimental procedures. Deviations from the standards are noted in the report.

4.2 Stacked-ply Tension Test

Specimen Geometry: ASTM D3039 standard [26] is applicable for this test. The specimen geometry and layout are shown in Fig. 4.1. Shaded regions indicate where fiberglass tabs were bonded to the specimen.

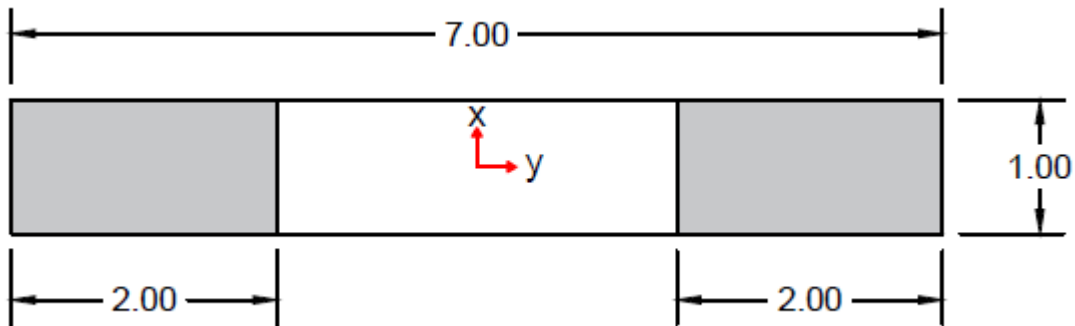


Fig. 4.1. Typical specimen geometry and layout (all dimensions in inches)

The average specimen dimensions in the gage section are shown in Table 4.1.

Table 4.1. Tension Test Specimen Dimensions

Replicate ID	Width (in)	Thickness (in)	Cross Sectional Area (in ²)
V-T-4	0.9990	0.0660	0.0659
V-T-5	0.9987	0.0633	0.0632
V-T-6	1.0022	0.0632	0.0634
Average	1.0000	0.0642	0.0642
Standard Deviation	0.0019	0.0016	0.0015
Coefficient of Variation (%)	0.19	2.47	2.39

The stroke rate of the MTS machine for this test was 0.02 in/min. The DIC image capture rate varied between one frame per five seconds and one frame per second.

Specimen Photographs: The specimen photographs before the tests are shown in Fig. 4.2. Post-test images include images of the gage area in the XY plane, zoomed in images of this plane, and images of the through thickness. Fig. 4.3 shows the specimens after testing.

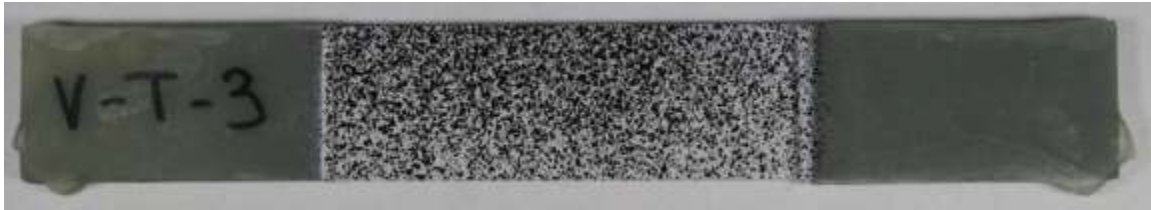


Fig. 4.2. Example image of tension specimen prior to testing



(a)



(b)



(c)



(d)

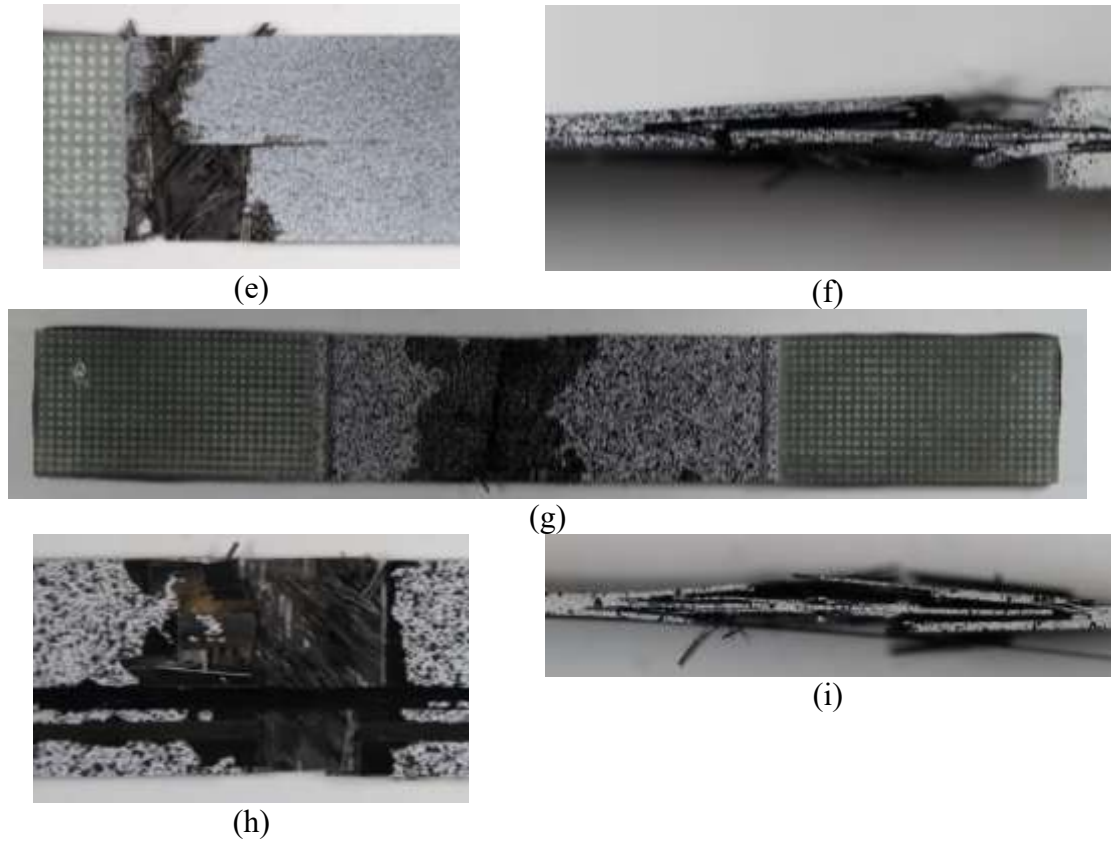


Fig. 4.3. Tension specimens after testing (a)(b)(c) V-T-4, (d)(e)(f) V-T-5, (g)(h)(i) V-T-6

Observations during the test and examination of the tested specimens suggested that the 0^0 -plies failed first. Once these plies failed, the redistribution of stress caused the other plies to fail subsequently.

Test Results: The summary of the test results is shown Table 4.2.

Table 4.2. Summary of Tension Test Results

Replicate ID	Loading Rate (in/min)	Strain Rate $\left(\frac{1}{s}\right)$	E_{yy} (psi)	Ultimate Strain	Peak Stress (psi)
V-T-4	0.02	7.67E-05	6923262	0.0169	117015
V-T-5	0.02	7.96E-05	7437892	0.0164	119019
V-T-6	0.02	8.23E-05	7100700	0.0178	125852

Average	-	7.95E-05	7153951	1.7039E-02	120628
Standard Deviation	-	2.80E-06	261415	7.0138E-04	4633
Coefficient of Variation (%)	-	3.52	3.65	4.12	3.84

Fig. 4.4 shows the individual stress-strain curves for the three specimens. The strain was the longitudinal strain measured on the surface of the specimen. The stress was the overall laminate stress; thus, the area used to find the stress was the combined area of all 8 plies.

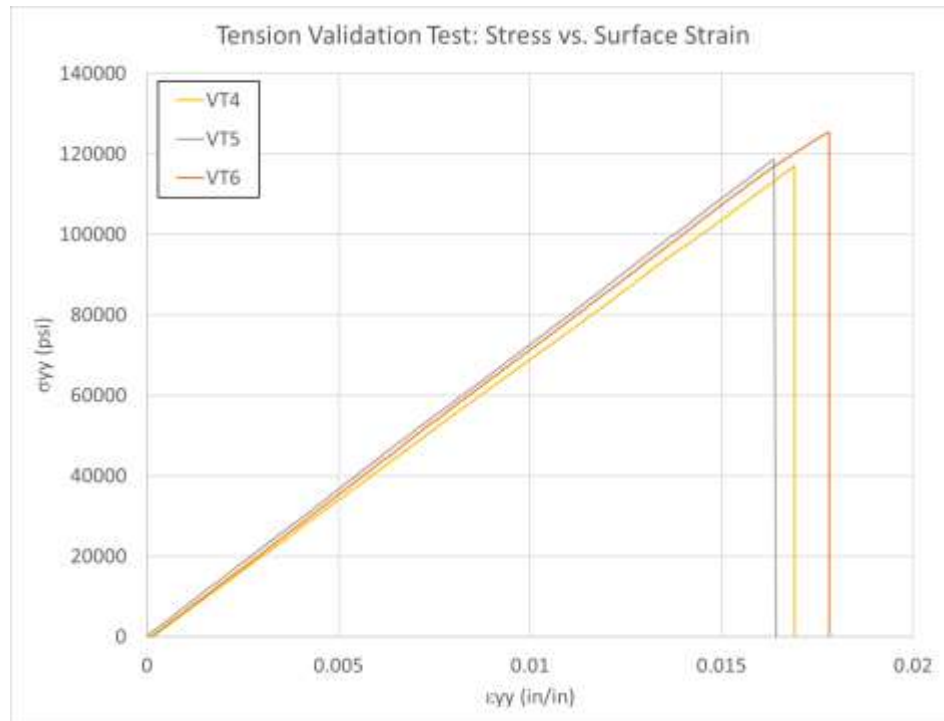


Fig. 4.4. Tension stress-strain curves

Fig. 4.4 shows the response was mostly linear since the 0° plies, oriented along the axis of loading, dominate the response of the composite laminate.

4.3 Stacked-Ply Compression Test

Specimen Geometry: ASTM D3410 and D6641 [27,28] standards are applicable for this test. The specimen geometry and layout are shown in Fig. 4.5. Shaded regions indicate where the specimen was gripped in the fixture.

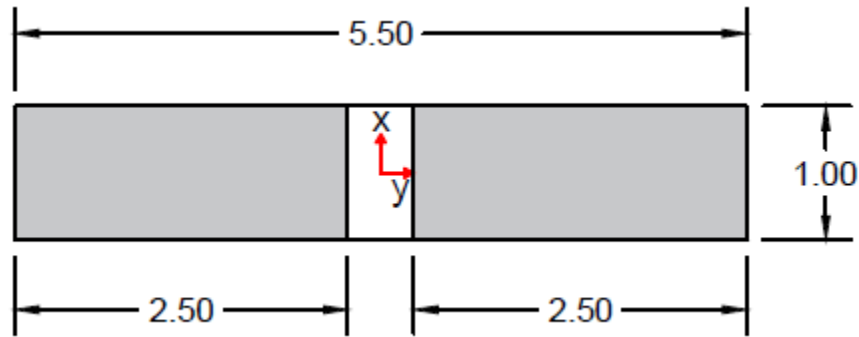


Fig. 4.5. Typical specimen geometry and layout (all dimensions in inches)

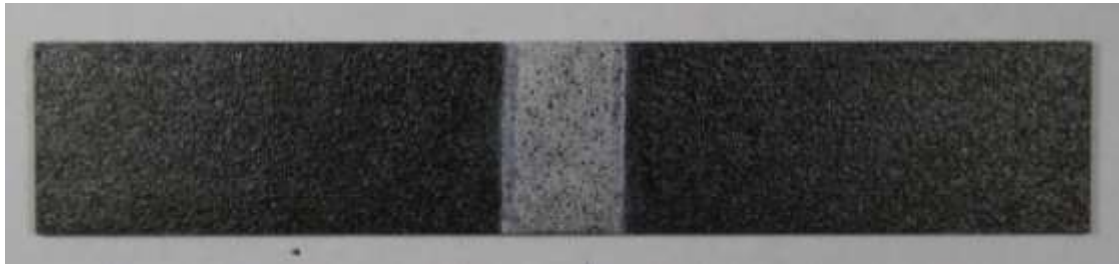
The average specimen dimensions in the gage section are shown in Table 4.3 for the tested replicates.

Table 4.3. Compression Test Specimen Dimensions

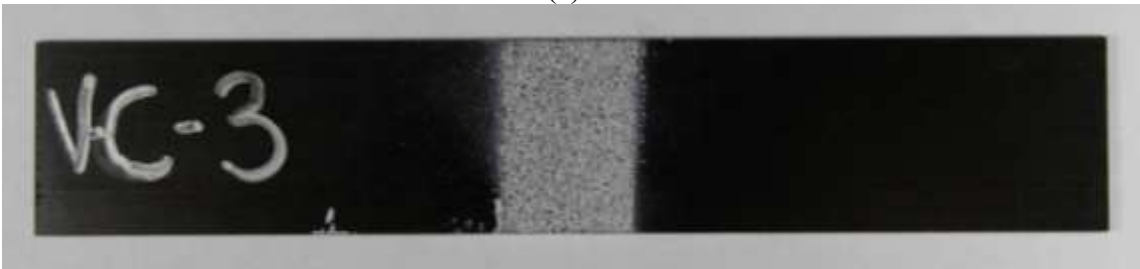
Replicate ID	Width (in)	Thickness (in)	Cross Sectional Area (in ²)
V-C-2	0.9982	0.0632	0.0631
V-C-3	0.9988	0.0624	0.0623
V-C-4	0.9984	0.0616	0.0615
Average	0.9985	0.0624	0.0623
Standard Deviation	0.0003	0.0008	0.0008
Coefficient of Variation (%)	0.03	1.28	1.27

The stroke rate of the MTS machine for this test was 0.01 in/min. The DIC image capture rate was one frame per five seconds.

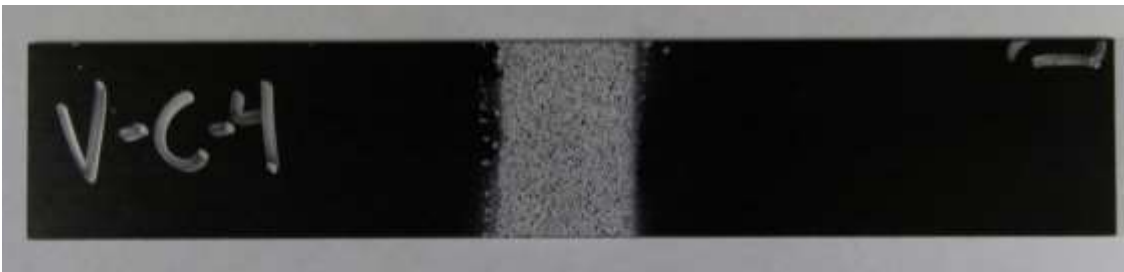
Specimen Photographs: The specimen photographs before the tests are shown in Fig. 4.6. Post-test images include images of the gage area in the XY plane and images of the through thickness state of the specimens. Fig. 4.7 shows the specimens after testing.



(a)

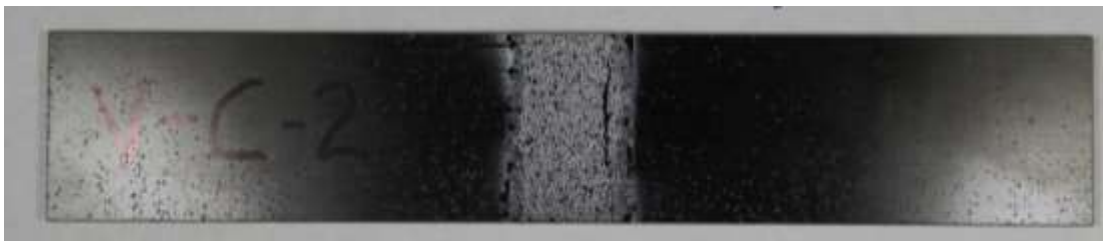


(b)

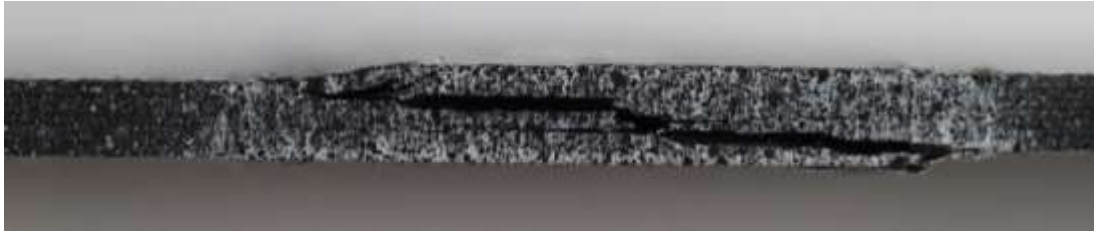


(c)

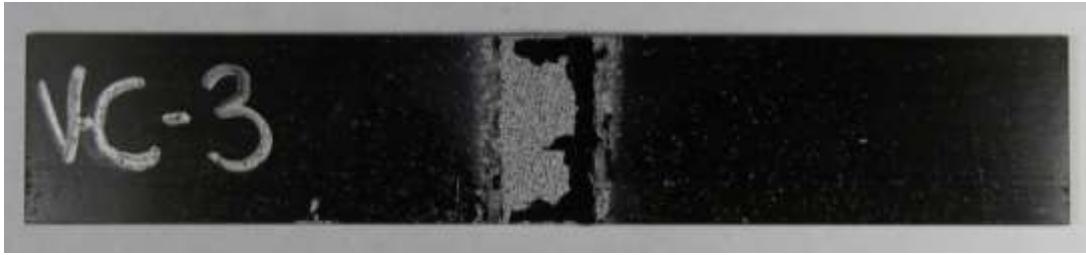
Fig. 4.6. Compression specimens prior to testing (a) V-C-2, (b) V-C-3, (c) V-C-4



(a)



(b)



(c)



(d)

Fig. 4.7. Compression specimens after testing (a) V-C-2 XY surface (b) V-C-2 through thickness (c) V-C-3 XY surface (d) V-C-3 through thickness

The failure pattern of Fig. 4.7(d) suggested that outer 0^0 and 90^0 -plies failed first, followed by out-of-plane buckling.

Test Results: The summary of the results from the tests is shown in Table 4.4.

Table 4.4. Summary of Compression Test Results

Replicate ID	Loading Rate (in/min)	Strain Rate $\left(\frac{1}{s}\right)$	E_{yy} (psi)	Ultimate Strain	Peak Stress (psi)
V-C-2	0.01	4.02E-05	6318793	-0.0064	-40609
V-C-3	0.01	3.17E-05	6076000	-0.0062	-40840
V-C-4	0.01	3.83E-05	6084202	-0.0060	-39085

Average	-	3.67E-05	6159665	-0.0062	-40178
Standard Deviation	-	4.46E-06	137870	0.0002	954
Coefficient of Variation (%)	-	12.15	2.24	2.89	2.37

Fig. 4.8 shows the individual stress-strain curves for each of the specimens that produced reliable results. The strain was the longitudinal strain measured on the surface of the specimen. The stress was the overall laminate stress (area of all 8 plies).

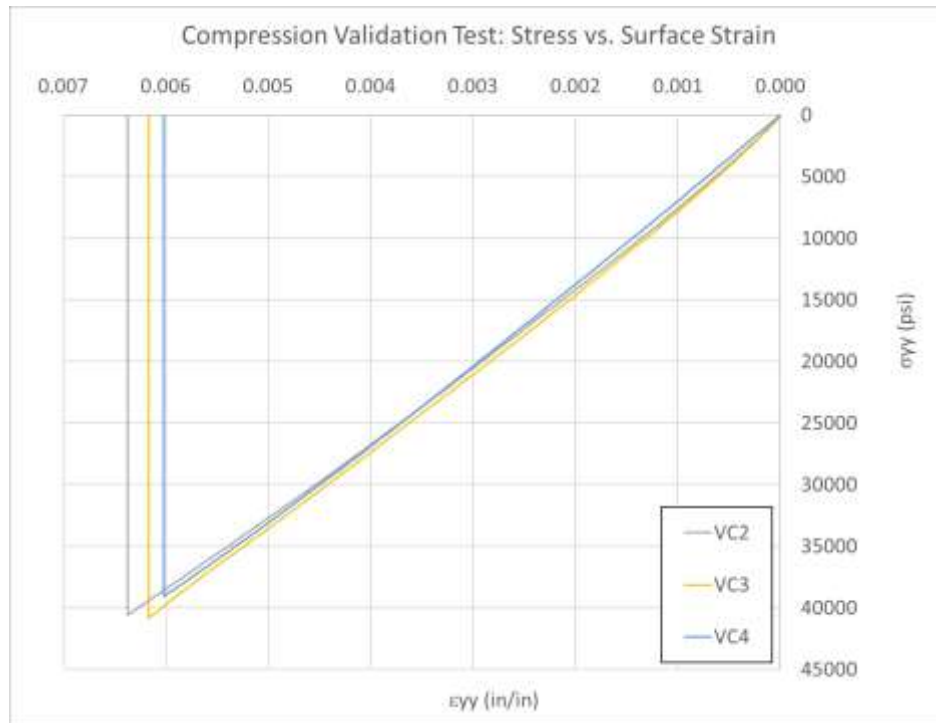


Fig. 4.8. Compression stress-strain curves

4.4 Stacked-ply Tension – Stress Concentration Test

Specimen Geometry: ASTM D3039 and D5766 standards [26,29] are applicable for this test. The specimen geometry and layout are shown in Fig. 4.9. Shaded regions indicate where fiberglass tabs were bonded to the specimen.

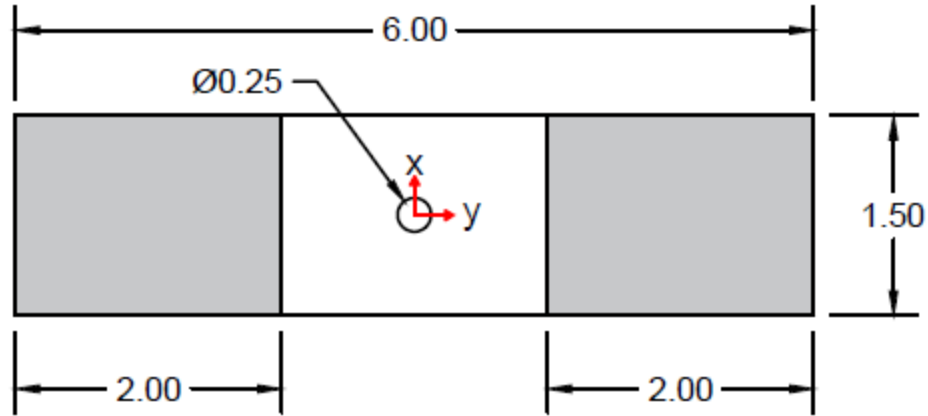


Fig. 4.9. Typical specimen geometry and layout (all dimensions in inches)

The average specimen dimensions in the gage section are shown in Table 4.5 for the tested replicates.

Table 4.5. Tension Stress Concentration Test Specimen Dimensions

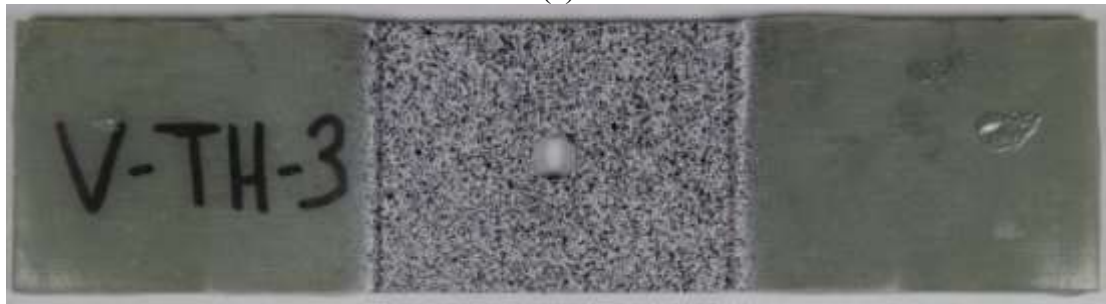
Replicate ID	Width (in)	Thickness (in)	Cross Sectional Area (in ²)	Hole Diameter (in)
V-TH-2	1.5027	0.0649	0.0975	-
V-TH-3	1.4981	0.0620	0.0929	-
V-TH-4	1.4980	0.0623	0.0933	-
Average	1.4996	0.0631	0.0946	0.25
Standard Deviation	0.0027	0.0016	0.0025	-
Coefficient of Variation (%)	0.18	2.53	2.69	-

The stroke rate of the MTS machine for this test was 0.01 in/min. The DIC image capture rate was one frame per five seconds.

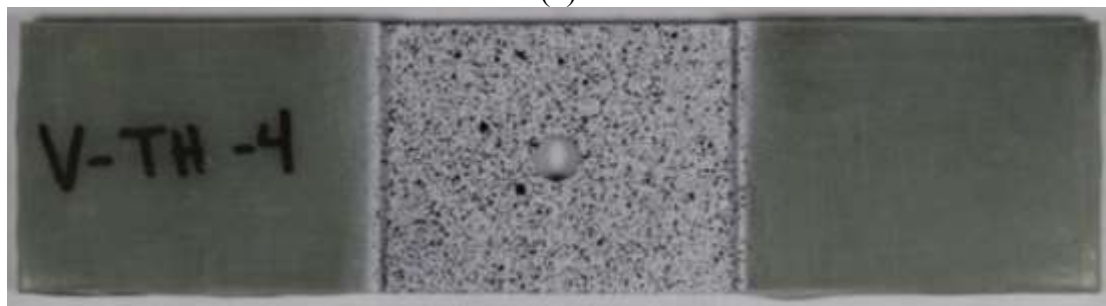
Specimen Photographs: The specimen photographs before the tests are shown in Fig. 4.10. Post-test images include images of the gage area in the XY plane, zoomed in images of this plane, and images of the through thickness state of the specimens. Fig. 4.11 shows the specimens after testing.



(a)



(b)



(c)

Fig. 4.10. Compression specimens prior to testing (a) V-TH-2, (b) V-TH-3, (c) V-TH-4



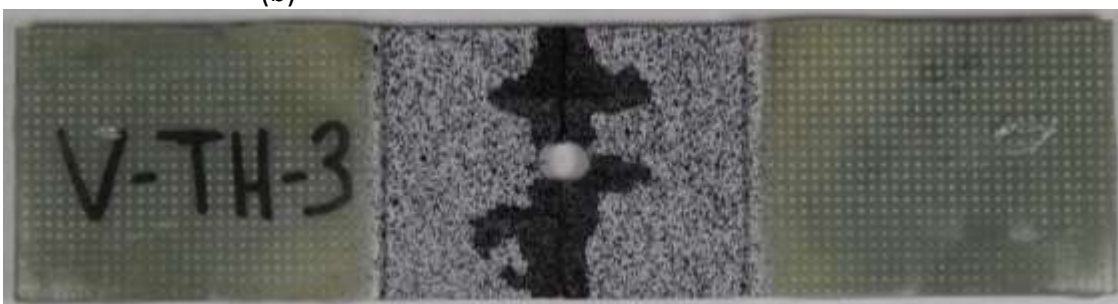
(a)



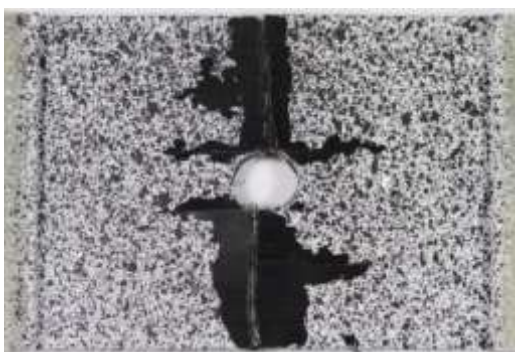
(b)



(c)



(d)



(e)



(f)



(g)

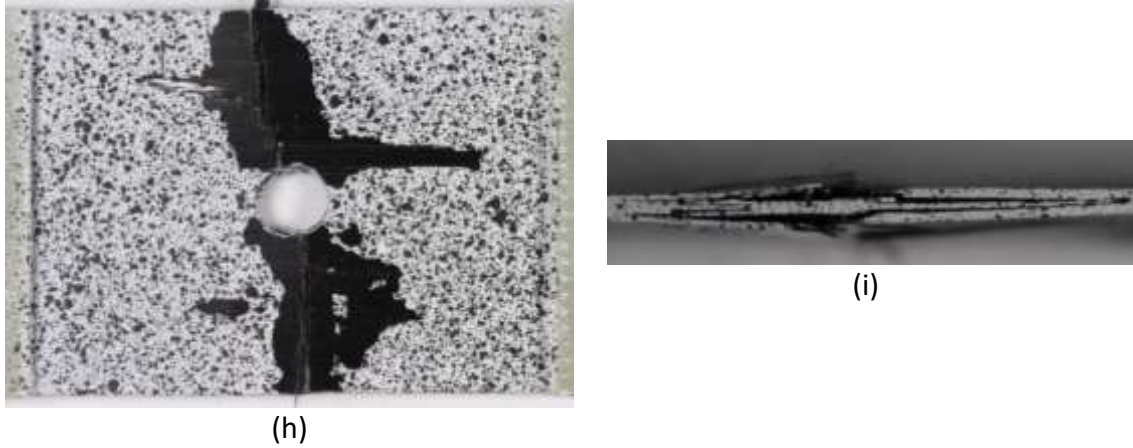


Fig. 4.11. Tension Stress Concentration specimens after testing (a)(b)(c) V-TH-2, (d)(e)(f) V-TH-3, (g)(h)(i) V-TH-4

Test Results: The summary of the test results is shown in Table 4.6

Table 4.6. Summary of Tension Stress Concentration Test Results

Replicate ID	Loading Rate (in/min)	Strain Rate ϵ_{yy} (RL of Hole) (1/s)	Strain Rate ϵ_{xx} Magnitude (T of Hole) (1/s)	Maximum ϵ_{yy} (RL of Hole)	Maximum ϵ_{xx} (T of Hole)
V-TH-2	0.01	5.60E-05	1.26E-05	1.60E-02	-4.55E-03
V-TH-3	0.01	5.42E-05	1.29E-05	1.51E-02	-4.05E-03
V-TH-4	0.01	5.73E-05	1.29E-05	1.62E-02	-4.52E-03
Average	-	5.58E-05	1.28E-05	1.58E-02	-4.37E-03
Standard Deviation	-	1.56E-06	1.73E-07	5.86E-04	2.80E-04
Coefficient of Variation (%)	-	2.79	1.35	3.72	6.41

Strain data in the x and y directions were obtained for areas to right and left of the hole as well as above and below the hole. It was found that in these areas, the x and y strains matched closely with the principal strains.

The average strain within the gage area in the y direction for the areas to the left and right of the hole is shown in Fig. 4.12.

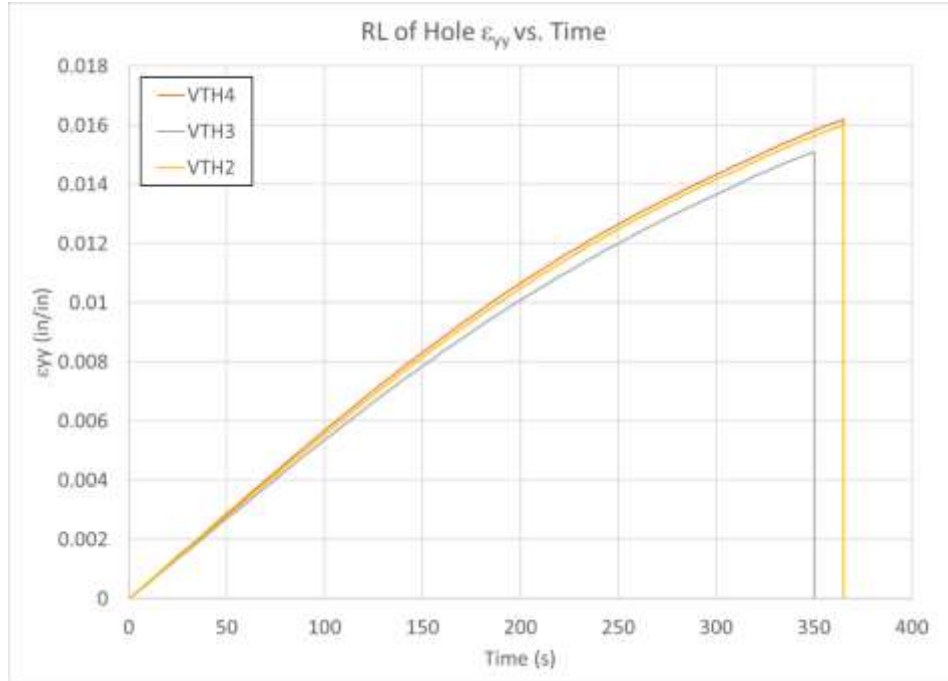


Fig. 4.12. Tension stress concentration RL of hole ϵ_{yy} vs. time

The x strain for the area above the hole is shown in Fig. 4.13 and for the area below the hole in Fig. 4.14.

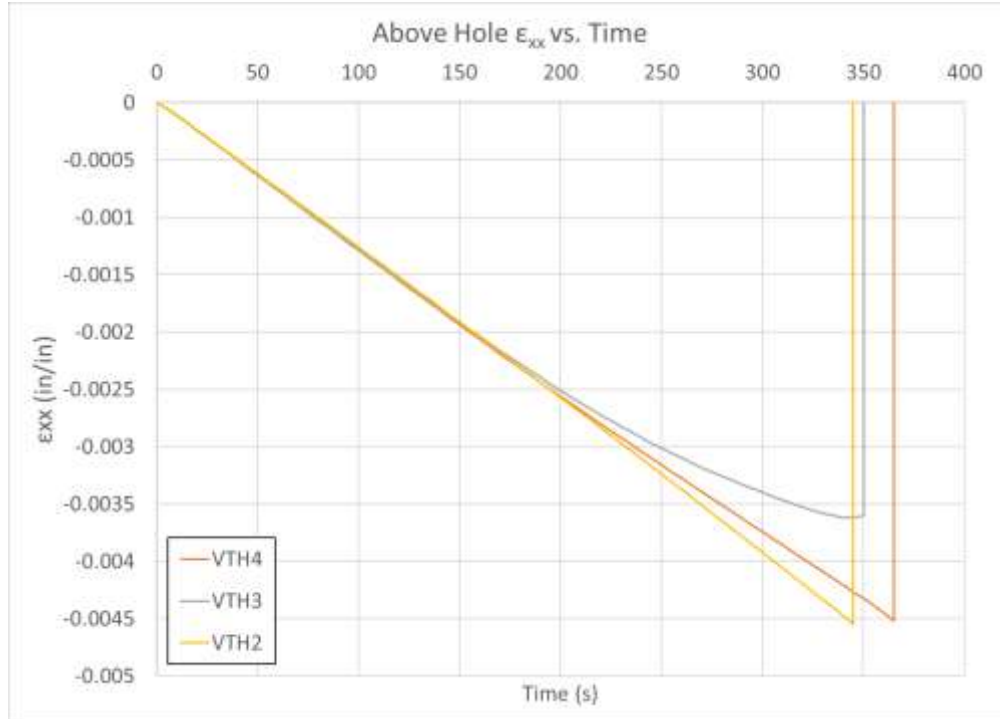


Fig. 4.13. Tension stress concentration: above hole ϵ_{xx} vs. time

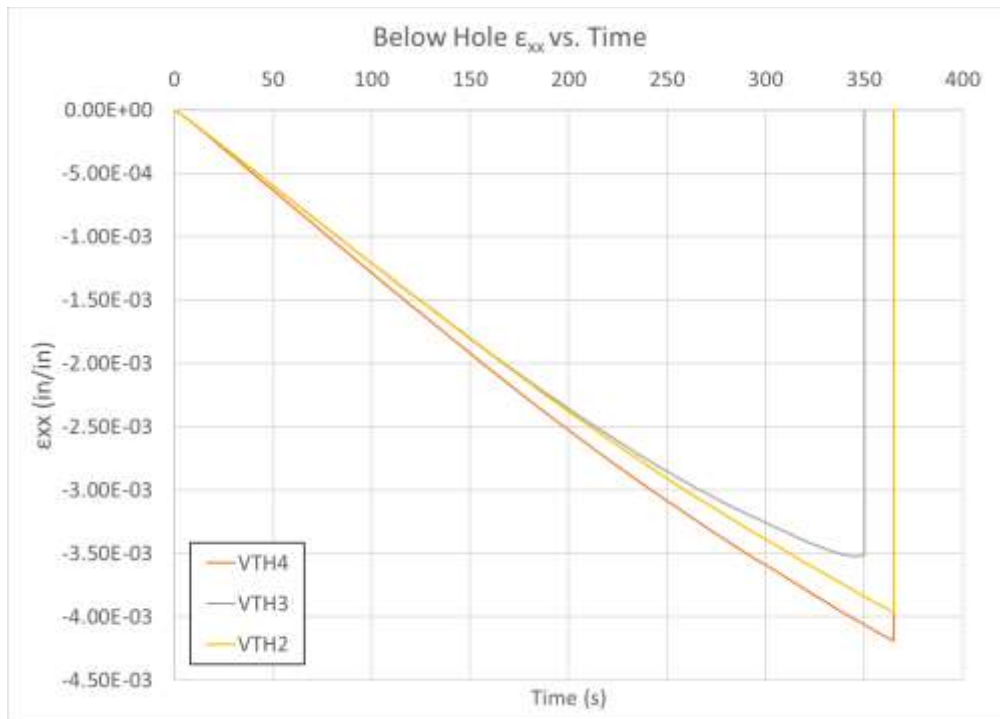


Fig. 4.14. Tension stress concentration: below hole ϵ_{xx} vs. time

4.5 Stacked-ply Compression – Stress Concentration Test

Specimen Geometry: ASTM D6641 and D6484 [27,30] standards were applicable for this test. The specimen geometry and layout are shown in Fig. 4.15. Shaded regions indicate where the fixture gripped the specimen and applied loading through shear and compression at the ends.

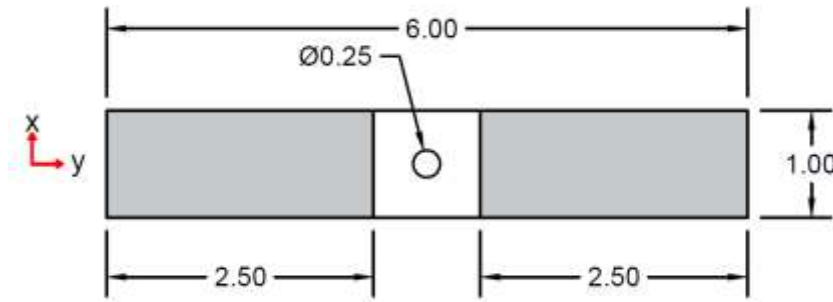


Fig. 4.15. Typical specimen geometry and layout (all dimensions in inches)

Three replicates were tested with the stated geometry. The average specimen dimensions in the gage section are shown in Table 4.7.

Table 4.7. Compression Stress Concentration Test Specimen Dimensions

Replicate ID	Width (in)	Thickness (in)	Cross Sectional Area (in ²)	Hole Diameter (in)
V-CH-5	0.9990	0.0599	0.0598	-
V-CH-7	1.0011	0.0624	0.0624	-
V-CH-8	1.0013	0.0634	0.0634	-
Average	1.0005	0.0619	0.0619	0.25
Standard Deviation	0.0013	0.0018	0.0019	-
Coefficient of Variation (%)	0.13	2.91	3.04	-

The stroke rate of the MTS machine for this test was 0.01 in/min. The DIC image capture rate was one frame per second.

Specimen Photographs: The specimen photographs before the tests are shown in Fig. 4.16. Post-test images include images of the gage area in the XY plane, zoomed in

images of this plane, and images of the through thickness. Fig. 4.17 shows the specimens after testing.

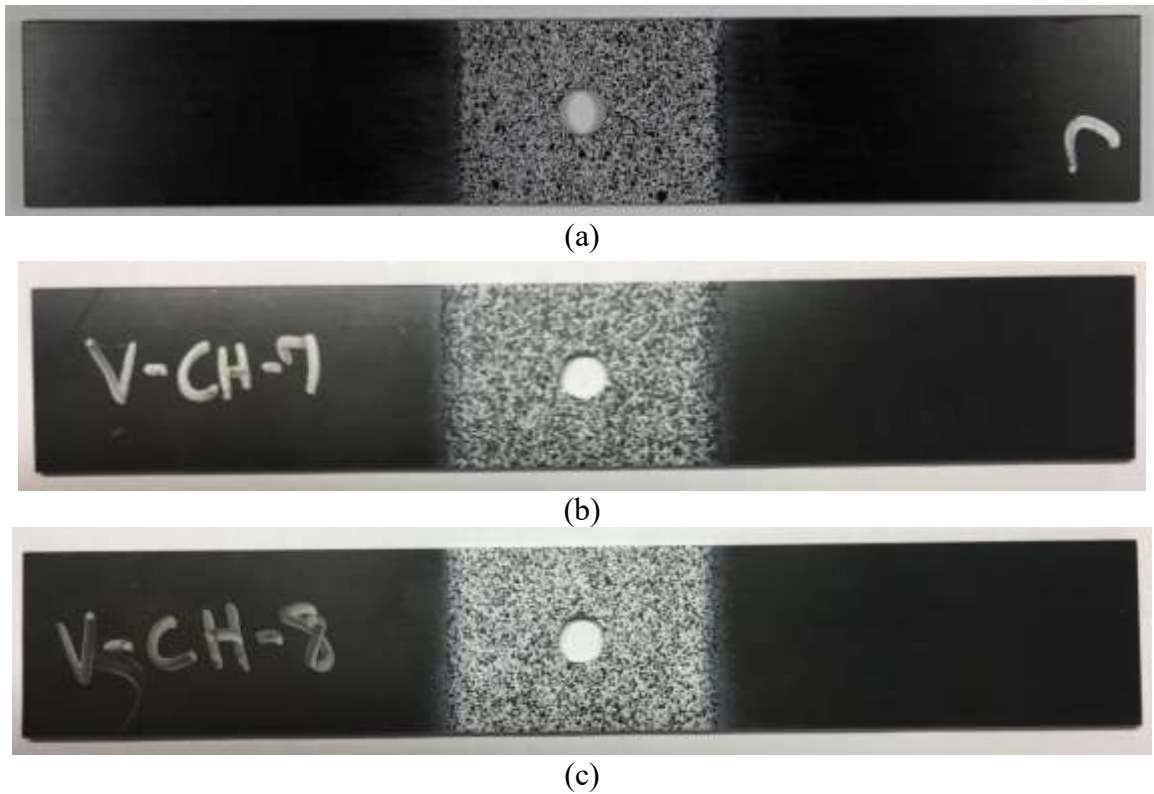
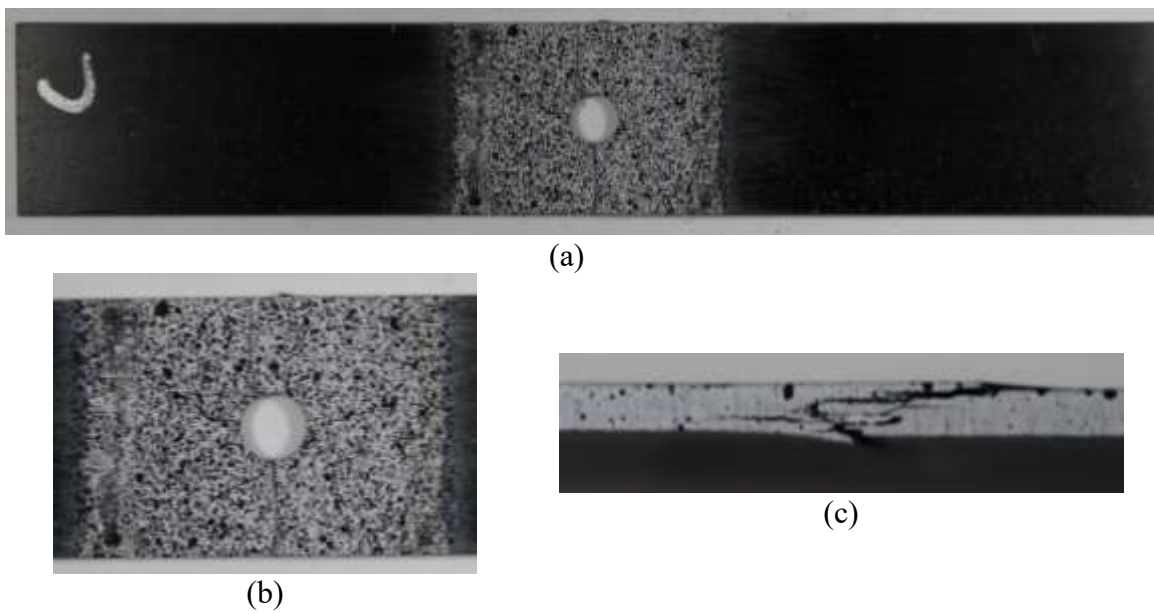


Fig. 4.16. Compression specimens prior to testing (a) V-CH-5, (b) V-CH-7, (c) V-CH-8



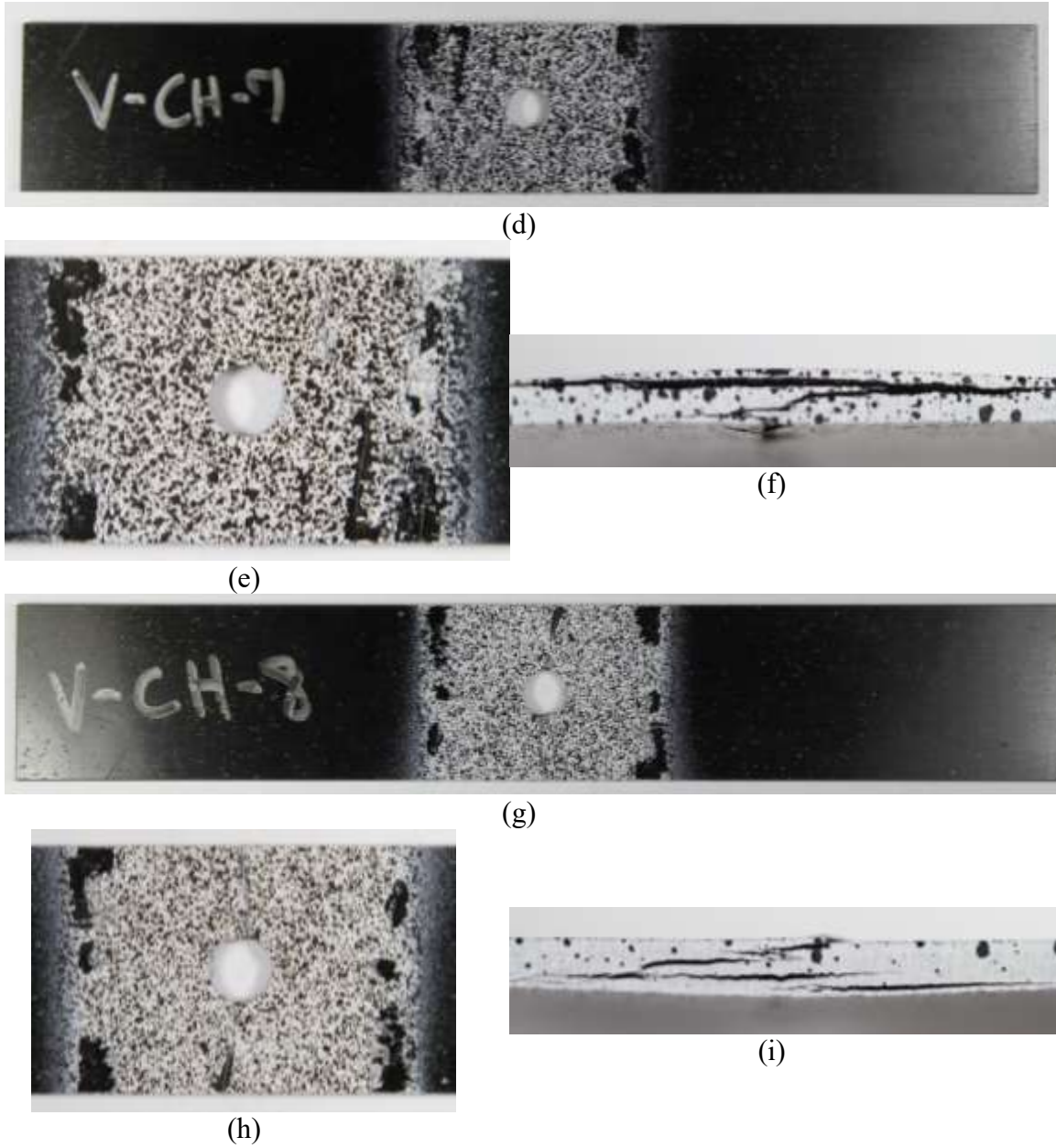


Fig. 4.17. Compression Stress Concentration specimens after testing (a)(b)(c) V-CH-5, (d)(e)(f) V-CH-7, (g)(h)(i) V-CH-8

Test Results: The summary of the test results is shown in Table 4.8.

Table 4.8. Summary of Compression Stress Concentration Test Results

Replicate ID	Loading Rate (in/min)	Strain Rate e_{yy} magnitude (RL of Hole) (1/s)	Strain Rate e_{xx} (T of Hole) (1/s)	Maximum e_{yy} (RL of Hole)	Maximum e_{xx} (T of Hole)
V-CH-5	0.01	5.27E-05	1.16E-05	-9.85E-03	2.11E-03
V-CH-7	0.01	5.14E-05	1.18E-05	-1.00E-02	2.19E-03

V-CH-8	0.01	5.26E-05	1.12E-05	-7.68E-03	1.99E-03
Average	-	5.22E-05	1.15E-05	-9.19E-03	2.10E-03
Standard Deviation	-	7.33E-07	3.06E-07	1.31E-03	1.01E-04
Coefficient of Variation (%)	-	1.40	2.65	14.30	4.83

Strain data in the x and y directions were obtained for areas to right and left of the hole as well as above and below the hole. It was found that in these areas, the x and y strains matched closely with the principal strains.

The average strain in the y direction in the areas to the left and right of the hole is presented in Fig. 4.18.

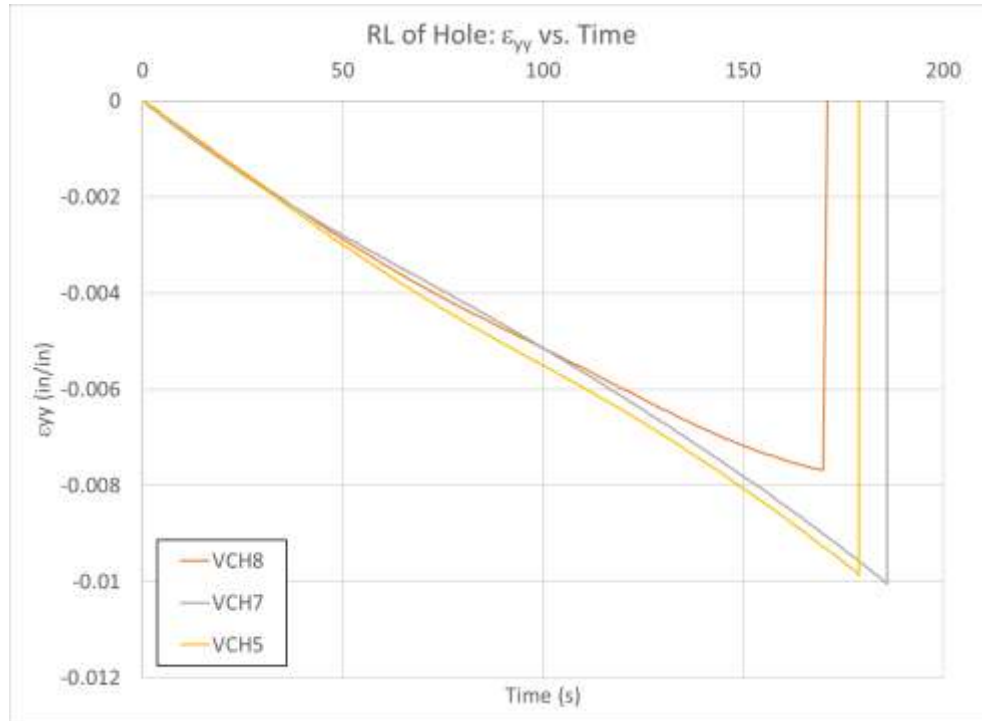


Fig. 4.18. Compression stress concentration RL of hole ϵ_{yy} vs. time

The x strain for the area above the hole is shown in Fig. 4.19 and for the area below the hole in Fig. 4.20.

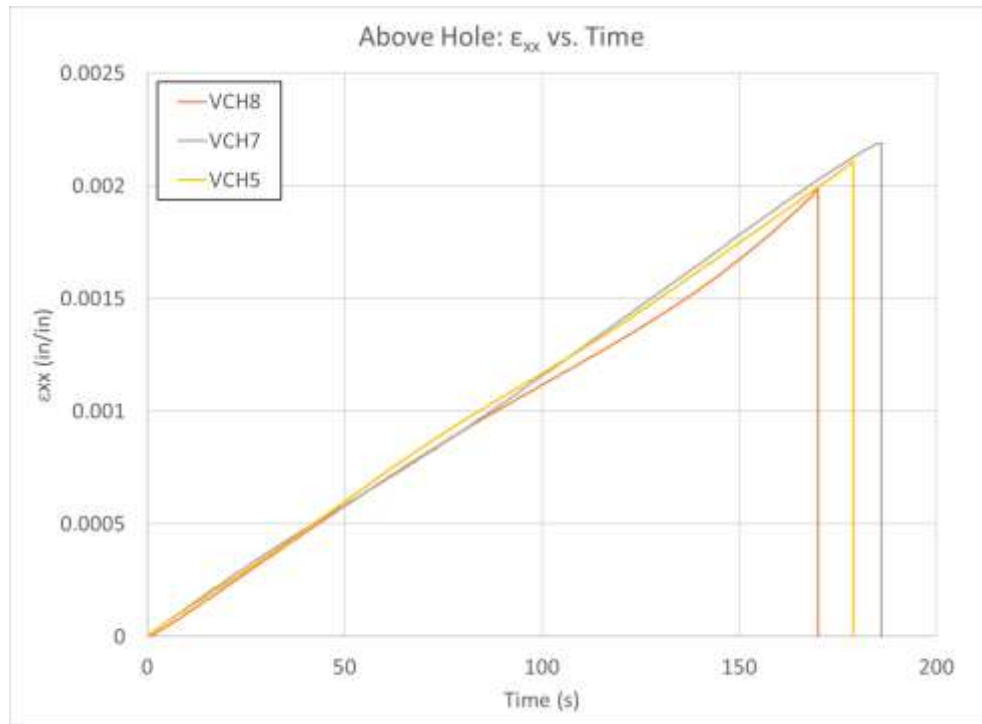


Fig. 4.19. Compression stress concentration: above hole ϵ_{xx} vs. time

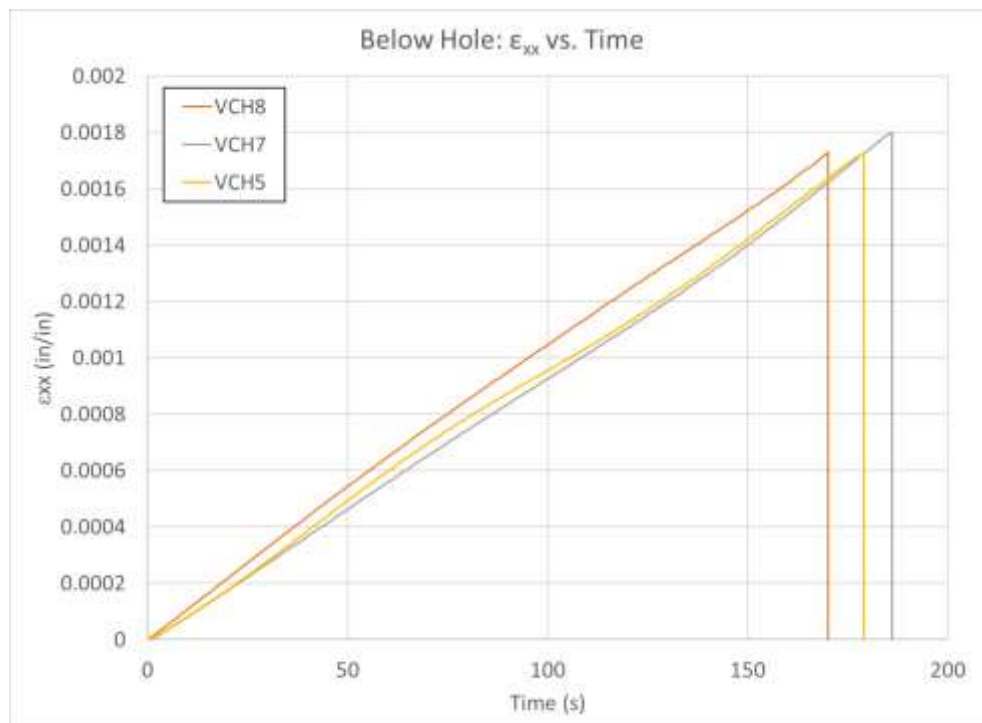


Fig. 4.20. Compression stress concentration: below hole ϵ_{xx} vs. time

4.6 Experimental Observations

The failure of all tests occurred very rapidly, much faster than the frame rate of the DIC images, thus no data was obtained through DIC showing failure onset. However comparisons were still made between the tests as to the deformation shown through DIC. In addition, comparisons between failure patterns were made by visual observations of the failed specimens after completion of the tests.

The tension tests typically failed in a manner that affected nearly one inch of the gage section. Post-test images shown in Fig. 4.3 depict delamination of the outer plies from the inner plies, while the inner plies did not show delamination. After complete failure of the outer plies, they delaminated on either side of the fracture zone by approximately one half inch, this delamination is observed in Fig. 4.3(i).

The tension with hole tests showed a more localized failure for the outer plies. Top down views of the post-test gage section, as in Fig. 4.11(e), show a clear line of fracture along which the outer plies failed. These tests showed delamination on the side of the specimen similar to that of the tension tests without the hole.

The compression tests showed a failure pattern that extended throughout the entirety of the half inch gage section length. Though the three tested specimens had similar failure strengths, the failure patterns are different. Fig. 4.7(d) shows a tested specimen in which the outer plies failed and delaminated for the length of the gage section, while delamination was not observed for the inner plies. Fig. 4.7(b) shows a tested specimen with a diagonal failure pattern, extending from the top of the thickness on one end of the gage section, to the bottom at the other end of the gage section. This

diagonal failure pattern suggests that there was some asymmetry in the loading of the specimen through the CLC fixture.

The compression with hole tests resulted in failure patterns that did not extend for the entire length of the gage section. These tests failed at the center gage section, at the hole, and did not show delamination in the outer plies to the extent that some of the compression without hole tests. The failure pattern on the edge of the specimen through the thickness as shown in Fig. 4.17(c) resembles the diagonal failure pattern of the compression test shown in Fig. 4.7(b). However, other compression with hole tests did not have a distinct diagonal failure, and instead show delamination between multiple layers of the composite, between outer and inner plies, such as those seen in Fig. 4.17(f) and Fig. 4.17(i).

5. QS-RT Fracture Mode Test Details and Results

5.1 Overview

Delamination testing was performed on the T800/F3900 composite material to help build cohesive zone models (CZM), i.e. for the use of LS-DYNA MAT 138 (MAT_COHESIVE_MIXED_MODE). Experimental tests were performed characterizing delamination of the material and these tests were then replicated in LS-DYNA simulations to calibrate the CZM.

Two types of fracture analysis tests were conducted - the end notch flexure test (ENF) and the double cantilevered beam test (DCB). The DCB and ENF tests were used to characterize mode I and mode II fracture properties respectively. The experimental tests were used to determine the critical energy release rates in mode I and mode II fracture. The other parameters required to model the CZM elements in LS-DYNA were determined by a calibration process to match experimental data.

The material model used a bilinear traction separation law for both mode 1 and mode 2 fracture. The traction separation law is shown in Fig. 5.1.

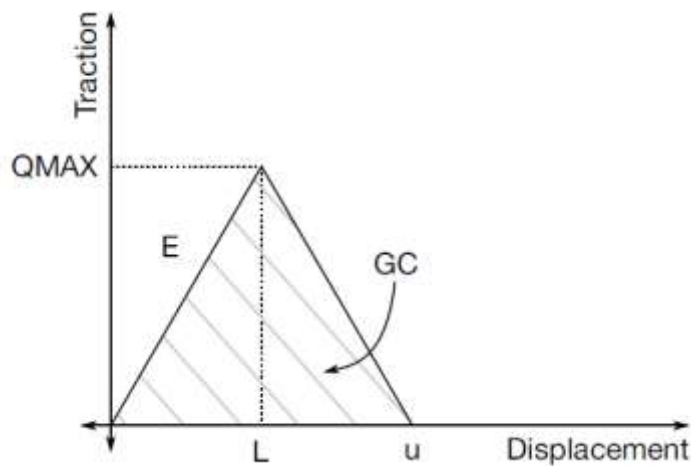


Fig. 5.1. Traction-separation law used in MAT 138 [31]

A total of six parameters are needed to completely describe the separation laws for both mode 1 and mode 2 and they are summarized in Table 5.1.

Table 5.1. MAT 138 Parameter Summary

Parameter	Opening Mode	Description	Units	Method Obtained
G_{IC}	1	critical energy release rate in mode I fracture	Energy/area	Experimentally
EN	1	initial stiffness of the cohesive zone normal to the plane of the elements	Stress/length	Calibration through LS-DYNA simulation
T	1	peak tensile traction	Stress	Calibration through LS-DYNA simulation
G_{IIC}	2	critical energy release rate in mode II fracture	Energy/area	Experimentally
ET	2	initial stiffness of the cohesive zone tangent to the plane of the elements	Stress/length	Calibration through LS-DYNA simulation
S	2	peak tangential (shear) traction	Stress	Calibration through LS-DYNA simulation

5.2 General Experimental Procedures

Unless otherwise noted, all preparation, equipment, and procedures are the same as stated in Section 3 of this report.

5.2.1 Sample Preparation

The ENF and DCB tests were performed using the T800/F3900 composite material manufactured by Toray Composites, Seattle, WA [32]. Test coupons were cut from 16 in x 16 in panels comprised of 24 layers of unidirectional fibers. The panels were manufactured with 2-inch long Teflon® film inserts on two opposite edges in the center layer through the thickness. These inserts provide an initial delamination such that the top and bottom halves of the panels were not bonded along these edges. Fig. 5.2 below shows examples of coupon cuts from the boards. The two horizontal white lines in the figure mark the end of the inserts.

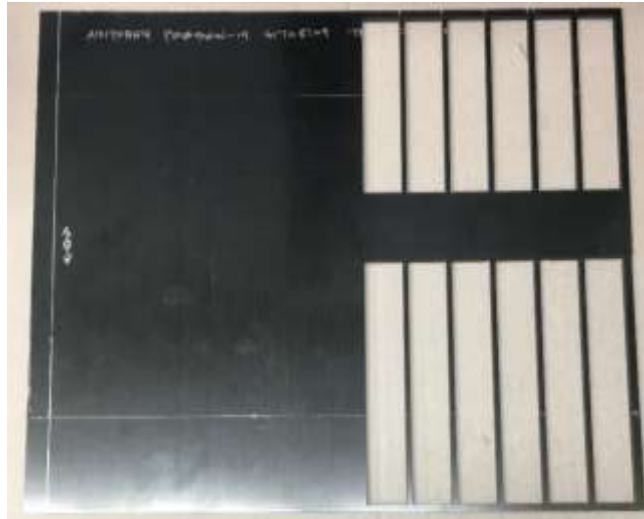


Fig. 5.2. ENF and DCB manufactured boards showing test coupons cut from the original panel

Both DCB and ENF samples were cut with waterjet with the same specifications as given in section 2.1.

DCB tests were conducted with piano hinges obtained from Material Testing Technology⁶. Fig. 5.3 shows an example of the piano hinges used for these tests.



Fig. 5.3. Piano hinges for DCB test

⁶ <http://www.mttusa.net/ISOS.15024.10.html>

The piano hinges were bonded to the DCB test coupons using 3M DP420 Scotch Weld⁷ toughened two-part epoxy. This was a different epoxy from that used for bonding the fiberglass tabs in the stacked-ply validation tests. The DP420 epoxy gave higher strength when bonding to the piano hinges as compared to the DP460 epoxy.

All specimens were prepared in the same manner unless otherwise noted. The following list outlines the steps taken to fully prepare the specimens.

1. For DCB Tests: the regions on a typical specimen where piano hinges were bonded were lightly sanded using 220 grit sandpaper. Sanding the surfaces ensured a complete bond between the specimen and hinges. The piano hinges were sanded with 100 grit sandpaper to scuff and scratch the surface of the bond area.
2. The sanded surfaces were then cleaned using cotton swabs soaked with isopropyl alcohol. The surfaces were allowed to air dry until there was no visible moisture on the bonding surfaces.
3. The 3M epoxy was mixed in accordance to the manufacturer's recommendation. A thin layer of the mixed epoxy was applied to the piano hinge using a wooden applicator.

⁷https://multimedia.3m.com/mws/media/66998O/scotch-weldtm-epoxy-adhesive-dp420-blck-ns-blck-offwhit-lh.pdf&fn=420_090216_R4.pdf

4. The tabs were then placed on the specimen and positioned until the surfaces of the specimen and the tabs were in complete contact and aligned properly in the desired region.
5. The specimens were allowed to cure at room temperature and atmospheric pressure for 24 hours.
6. For All Tests: Next, one face of the thickness of the specimen was painted and speckled. Speckling of the specimen involved first spraying the surface of the specimen with a layer of white paint with a flat finish. Paint was sprayed onto the surface until the specimen can no longer be seen. The paint was allowed to completely dry at room temperature.
7. After the white paint dried, black paint, with a flat finish, was sprayed onto the dry white paint. The black paint was sprayed in a manner which results in random array of black dots being deposited on the white area of the specimen.
8. After the specimens had been painted, they were allowed to finishing curing for another 24 hours as recommended by the manufacturer.
9. The location of the end of the insert was marked on the speckled surface so as to be clearly seen in the DIC images.
10. For ENF Tests: The calibration markings were added to the top surface of the specimen according to the ASTM standards for this test.

5.2.2 Test Machines, Fixtures, Equipment and Software

All ENF and DCB tests were performed using an MTS Exceed Model E42⁸ machine with a load cell model number BSS-XS-500KG⁹ (Fig. 5.4.a). DCB tests were performed using spring loaded grips as shown in Fig. 5.4(b) and Fig. 5.4(c). ENF tests were performed using a 3-point bend fixture as shown in Fig. 5.4(d).



(a)



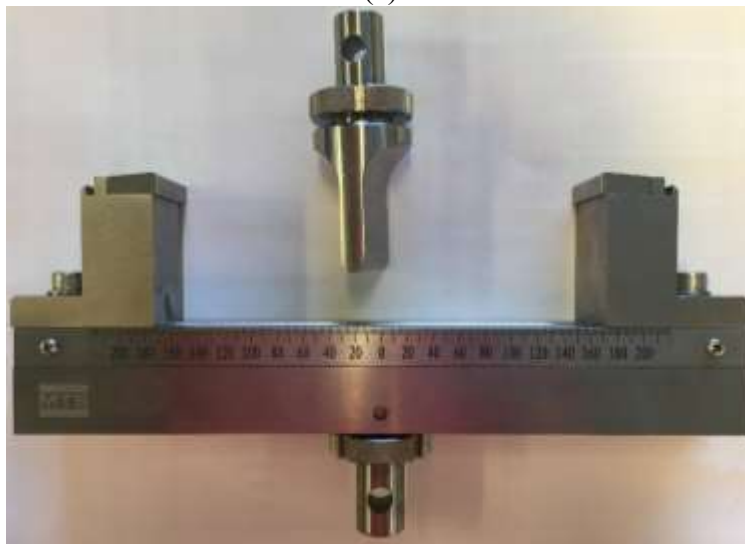
(b)

⁸ https://www.mts.com/cs/groups/public/documents/library/mts_2011071.pdf

⁹ <https://shop.transcell.com/wp-content/uploads/2016/06/BSS.pdf>



(c)



(d)

Fig. 5.4. Test machines and fixtures (a) MTS load frame (b) Spring loaded grips front view (c) Spring loaded grips side view (d) 3-point bend fixture

Digital Image Correlation (DIC) Equipment: Two Point Grey Grasshopper 3 cameras were used to capture images of the specimen throughout the duration of the

experiments. Attached to one of the cameras was a Tokina 100 mm lens¹⁰ while the other camera was used with the Schneider 35 mm lens. The Tokina lens had a higher resolution and was used to capture images for DIC processing. This camera was focused on the area of the initial crack tip. The Schneider lens provided images of the entire specimen to track and record the overall progress of the test. DIC processing was carried out with VIC 2D [25], a software program that requires images from only one camera for analysis. The two cameras were therefore independent of each other.



Fig. 5.5. Typical camera setup for ENF and DCB tests, Tokina 100 mm lens (top) and Schneider 35 mm lens (bottom)

The Tokina lens attached to the Point Grey Grasshopper 3 camera is shown in Fig. 5.6.

¹⁰ <http://tokinalens.com/download/product/5ab25b6cfl d39.pdf>



Fig. 5.6. Tokina 100 mm lens on Point Grey Grasshopper 3 camera

5.2.3 Typical Test Procedure

DCB Test

ASTM D5528-13 [12] was used as a guideline to create the experimental setup. The experimental test yielded the value of G_{IC} , the critical energy release rate in mode I fracture (units of energy/area). The test setup is shown in Fig. 5.7.

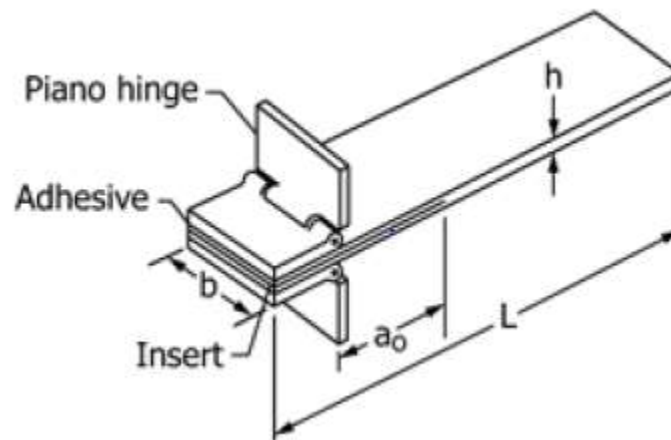


Fig. 5.7. DCB test setup [12]

The ASTM procedure was followed to calculate the G_{IC} values for both the non-precracked (NPC) and precracked (PC) conditions. The NPC condition meant the insert acted as the source of initial delamination with no further cracking induced in the

specimen. Testing in the NPC condition to a desired crack propagation as per the ASTM, yielded the PC condition, i.e. the PC condition was that in which some cracking had been induced in the specimen beyond the initial insert.

Fig. 5.8 shows an example of the DCB test being conducted after some delamination has occurred.

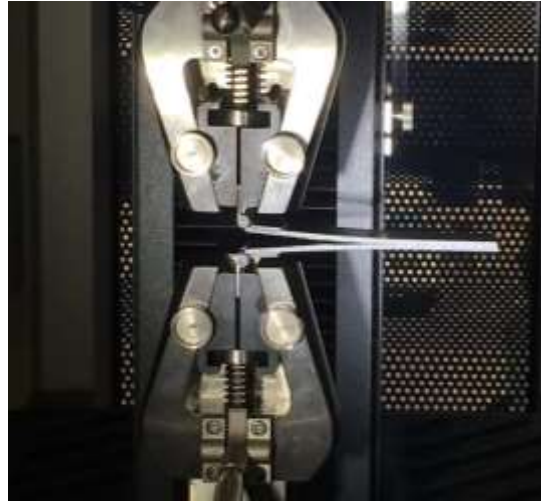


Fig. 5.8. DCB test

A loading rate of 1.2 mm/min was used for all tests. The NPC tests were loaded until a controlled crack growth of 5 mm was reached. The PC tests were loaded until complete separation of the top and bottom halves of the specimen.

As per the ASTM standard, the initiation value of G_{IC} were calculated 12 times. Three different definitions for an initiation value of G_{IC} were used including the point of deviation from linearity in the load-displacement curve (NL), the point at which delamination was visually observed on the edge (VIS), and the point at which the load had reached a maximum value (MAX) [12]. For each definition of the initiation value of G_{IC} , four different methods of calculation were used including modified beam theory

(MBT), rotation corrected modified beam theory (RCMBT), compliance calibration (CC), and modified compliance calibration (MCC).

The calculation for the strain energy release rate using MBT is given as

$$G_I = \frac{3P\delta}{2ba} \quad (5.1)$$

where P is the load, δ is the load point displacement, b is the specimen width, and a is the delamination length. The calculation for the strain energy release rate using RCMBT is given as:

$$G_I = \frac{3P\delta}{2b(a+|\Delta|)} \quad (5.2)$$

where the variables are the same as in (5.1) and Δ is determined experimentally through a relationship of the compliance and crack length. The calculation for the strain energy release rate using CC is given as:

$$G_I = \frac{nP\delta}{2ba} \quad (5.3)$$

where the variables are the same as in (5.1) and n is the slope of the compliance calibration line of best fit. The calculation for the strain energy release rate using MCC is given as:

$$G_I = \frac{3P^2C^{2/3}}{2A_1bh} \quad (5.4)$$

where the variables are the same as in (5.1) in addition to C being the compliance and A_1 being the slope of the line of best fit between the relationship of the normalized specimen thickness against the cubic root of compliance. Full procedures for all of the methods of

calculations and further details of the test procedure can be found in ASTM D5528-13 [12].

ENF Test

ASTM D7905/D7905M-14 [33] was used as a guideline to create the experimental setup. The experimental test yielded the value of G_{IIC} , the critical energy release rate in mode II fracture (units of energy/area). The test setup is shown in Fig. 5.9.

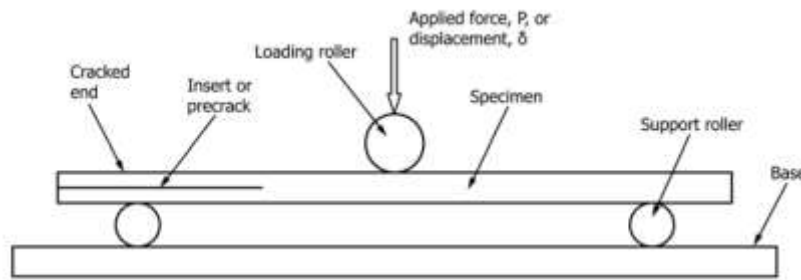


Fig. 5.9. ENF 3-point test setup [33]

The ASTM procedure was followed to calculate the G_{IIC} values for both the NPC and PC conditions. For each condition, two calibration cycles were performed and followed by a fracture cycle. The calibration and fracture cycles were all conducted on the same test specimen. The compliance of the specimen for each cycle was computed as the linear portion of the relationship between the load and displacement. The span between the support rollers was left constant across all cycles to ensure that the change in compliance was only a function of the crack length. The three cycles combined were used in the compliance calibration process to find a linear least squares regression on the relationship between the compliance of each cycle and the crack length of each cycle. Finally, the fracture test was used to calculate the G_{IIC} value as

$$G_{IIC} = \frac{3mP_{Max}^2 a_0^2}{2B} \quad (5.5)$$

where m is the CC coefficient, P_{max} is the maximum force from the fracture test, a_0 is the crack length in the fracture test, and B is the specimen width.

Fig. 5.10 shows an example of the ENF being conducted.

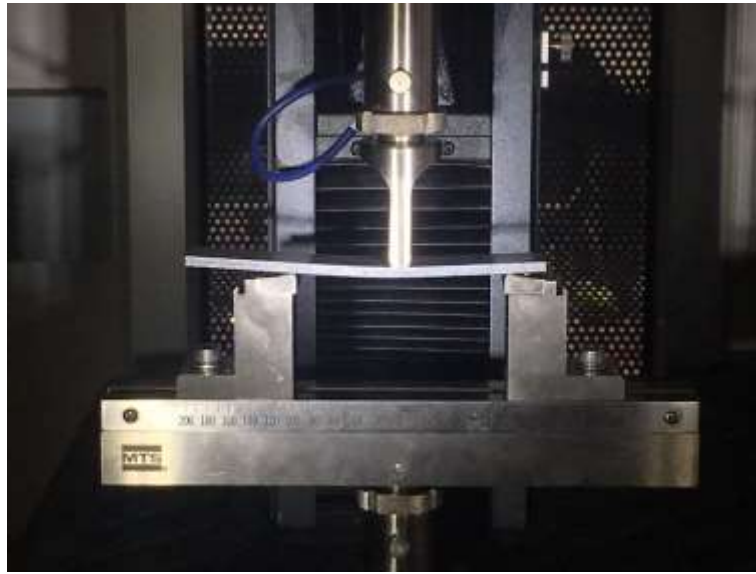


Fig. 5.10. ENF test

Further details of the test procedure can be found in ASTM D7905/D7905M-14 [33].

5.2.4 Post-processing of Test Data

ASTM standards were followed. At each data collection time, the force and displacement at the load point were extracted from the MTS machine. For the DCB tests, it was also necessary to track and record two other parameters during the test - the crack tip opening displacement and the crack propagation length. These parameters were obtained using DIC software, VIC-2D 2009 [25]. Displacement data was obtained using

DIC software and used to verify the displacement output of the MTS machine. Fig. 5.11 shows DIC y-displacement data plotted on a DCB test coupon during the test.

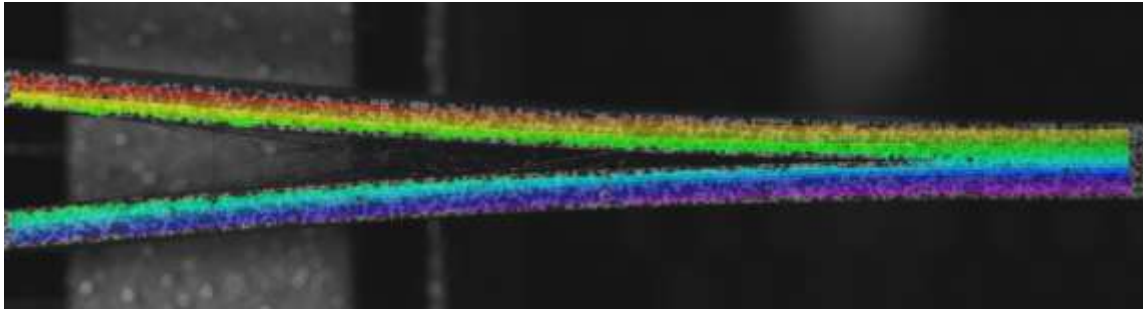


Fig. 5.11. Y-displacement DIC data for DCB test

The VIC-2D 2009 software has a crack opening data (COD) tool that was used to monitor the length of the crack in the cohesive layer between the top and bottom halves of the test coupon. The COD tool employed on the ENF test coupon is shown in Fig. 5.12.

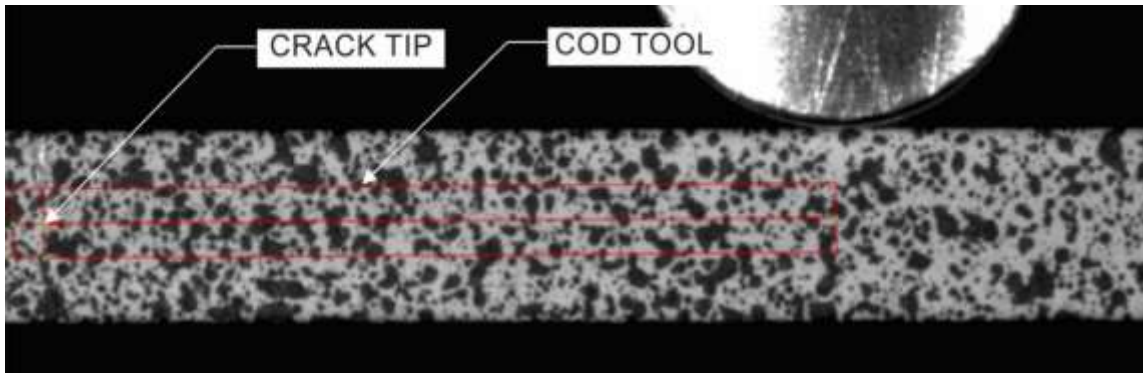


Fig. 5.12. COD tool on ENF specimen

While the COD tool had multiple capabilities, it was primarily used in the DCB tests to determine the crack tip opening displacement and the crack propagation length at any point in time of the test. The COD tool is shown in Fig. 5.13 on the DCB specimen after some delamination has occurred. Note that the tool could only be shown on the reference, or first, image of the test.

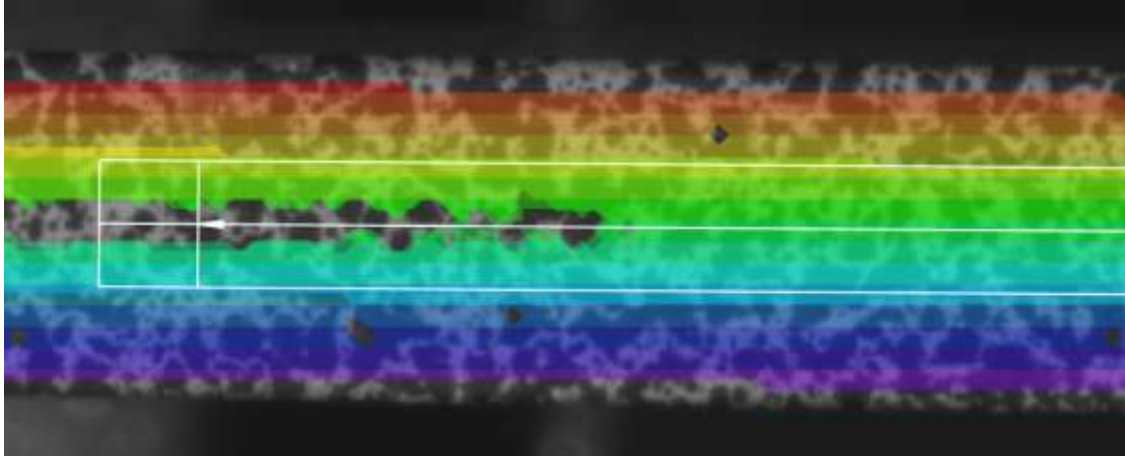


Fig. 5.13. COD tool on DCB specimen

The data collected with this tool and the data from the MTS machine allowed for the calculation of the strain energy release rates.

5.3 Experimental Results

5.3.1 ENF Test

Specimen Geometry: ASTM D7905 [33] standard is applicable for this test. The specimen geometry and layout are shown in Fig. 5.14.

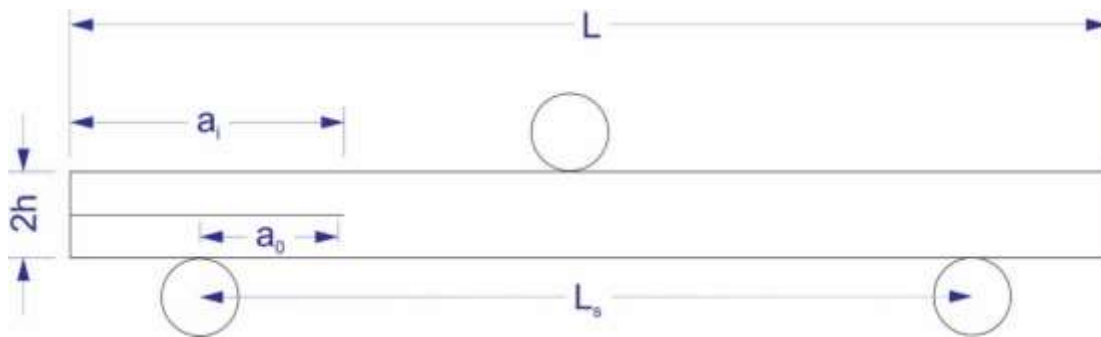


Fig. 5.14. Typical specimen geometry and layout

The average specimen dimensions of the test replicates are shown in Table 5.2.

Table 5.2. ENF Test Specimen Dimensions

Replicate ID	a_i (in)	a_0 (mm)	h (in)	b (in)	L (in)
ENF-2	2.349	20,30,40	0.097	1.008	6.560
ENF-3	2.357	20,30,40	0.093	1.004	6.575

ENF-4	2.352	20,30,40	0.093	1.003	6.555
ENF-5	2.358	20,30,40	0.094	1.005	6.555
ENF-6	2.362	20,30,40	0.093	1.003	6.530
Average	2.356	-	0.094	1.005	6.555
Standard Deviation	0.005	-	0.001	0.002	0.016
Coefficient of Variation (%)	0.215	-	1.586	0.205	0.247

Specimen Photographs: The specimen photographs before the tests are shown in Fig.

5.15. After testing images are shown in Fig. 5.16.

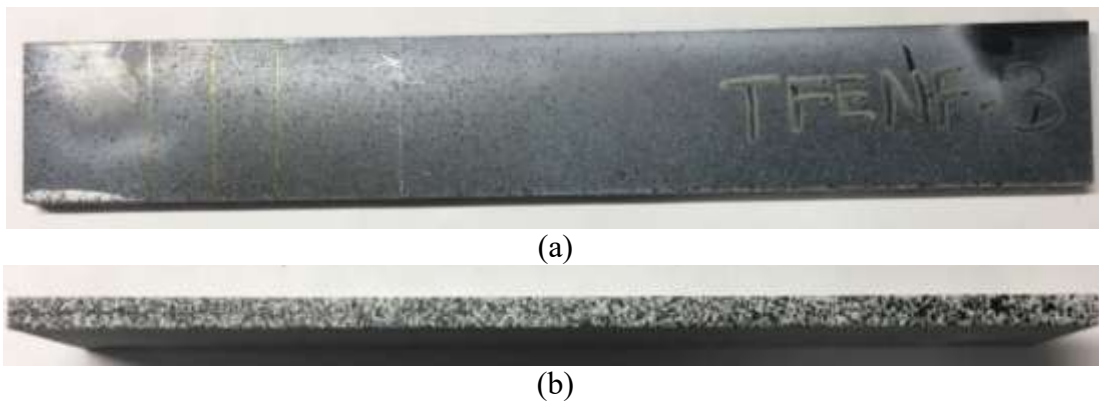


Fig. 5.15. Example image of ENF specimen prior to testing (a) Top surface showing specimen width (b) Side of specimen showing thickness

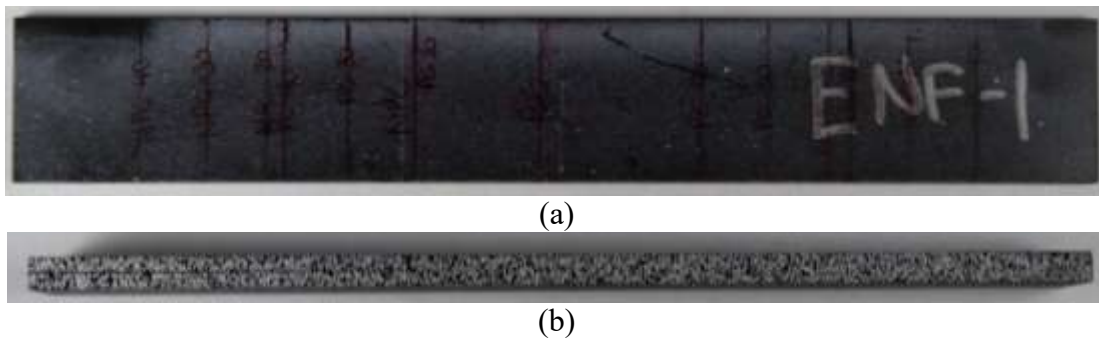


Fig. 5.16. Example image of ENF specimen after testing (a) Top surface showing specimen width (b) Side of specimen showing thickness

Test Results: The summary of the results from the Non-precracked tests is shown in Table 5.3. The variable *acalc* in this table refers to the post-test crack length as calculated using

unload data along with the compliance calibration coefficients m and A . The variable a_{meas} refers to the post-test crack length measured by visual observation and a digital caliper.

Table 5.3. Test Summary for ENF Non-precracked Tests

NPC						
Name	m (N ⁻¹ mm ⁻²)	A [mm/N]	G_{IIc} [N-mm/mm ²]	G_{IIc} [lb-in/in ²]	a_{calc} [mm]	a_{meas} [mm]
TFENF-2	9.98E-09	1.32E-03	2.28	13.02	50.98	49.23
TFENF-3	1.02E-08	1.28E-03	2.40	13.72	49.98	47.71
TFENF-4	8.95E-09	1.32E-03	2.35	13.43	52.79	53.15
TFENF-5	9.72E-09	1.28E-03	2.35	13.44	50.90	48.74
TFENF-6	9.47E-09	1.28E-03	2.26	12.87	51.32	48.59
Average	9.67E-09	1.30E-03	2.33	13.30	51.20	49.48
Standard Deviation	4.95E-10	2.21E-05	0.06	0.35	1.02	2.12
Coefficient of Variation (%)	5.12	1.71	2.60	2.60	1.99	4.29

The summary of the results from the pre-cracked tests is shown in Table 5.4.

Table 5.4. Test Summary for ENF Precracked Tests

PC					
Name	m (N ⁻¹ mm ⁻²)	A [mm/N]	G_{IIc} [N-mm/mm ²]	G_{IIc} [lb-in/in ²]	a_{calc} [mm]
TFENF-2	1.17E-08	1.12E-03	1.75	9.99	-45.77
TFENF-3	1.06E-08	1.10E-03	1.84	10.51	-46.98
TFENF-4	1.04E-08	1.07E-03	1.70	9.69	-46.86
TFENF-5	9.04E-09	1.05E-03	1.92	10.94	-48.73
TFENF-6	1.05E-08	1.05E-03	2.00	11.39	-46.41
Average	1.04E-08	1.08E-03	1.84	10.50	-46.95
Standard Deviation	9.47E-10	3.22E-05	0.12	0.69	1.10
Coefficient of Variation (%)	9.06	2.99	6.56	6.56	-2.35

The experimental results for the measured load and displacement that occurred at the load point are shown in Fig. 5.17.

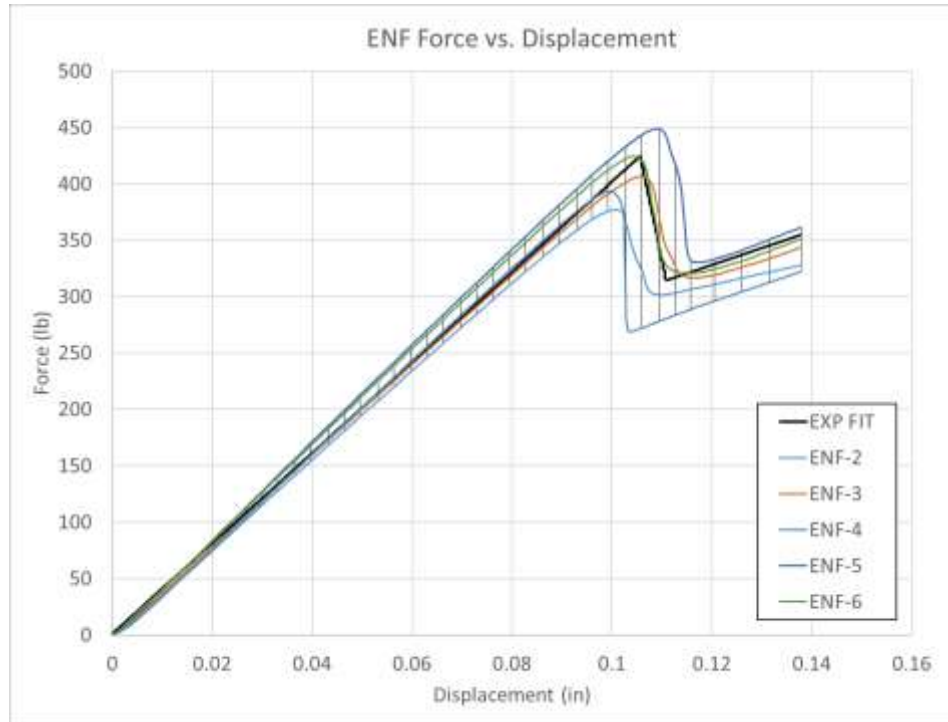


Fig. 5.17. ENF precrack experimental force vs. displacement

Five experimental curves are shown for test specimens with the precrack procedure. The experimental data across each replicate was fitted using polynomial regression to form an experimental model curve. This is labeled at “EXP FIT” in Fig. 5.17. The whisker plot depicts the range of the experimental data. The specifications of the regression are given in Table 5.5.

Table 5.5. ENF Experimental Regression Specifications

Section	Fit Type	R ²
Pre-peak	Linear	0.983
Post-peak	Linear	0.522

5.3.2 DCB Test

Specimen Geometry: ASTM D5528 [12] standard was applicable for this test. The specimen geometry and layout are shown in Fig. 5.18.



Fig. 5.18. Typical specimen geometry and layout

The average specimen dimensions of the test replicates are shown in Table 5.6.

Table 5.6. DCB Test Specimen Dimensions

Replicate ID	a_0 (in) NPC	a_0 (in) PC	h (in)	b (in)	L (in)
DCB-3	2.291	2.625	0.094	1.007	4.999
DCB-4	2.277	2.652	0.094	1.003	5.002
DCB-5	2.311	2.624	0.093	1.004	5.002
DCB-6	2.314	2.866	0.093	1.003	4.994
Average	2.298	2.692	0.093	1.004	4.999
Standard Deviation	1.76E-02	1.17E-01	4.59E-04	2.24E-03	3.93E-03
Coefficient of Variation (%)	0.77	4.35	0.49	0.22	0.08

Specimen Photographs: The specimen photographs before the tests are shown in Fig. 5.19. After testing images are shown in Fig. 5.20.



(a)

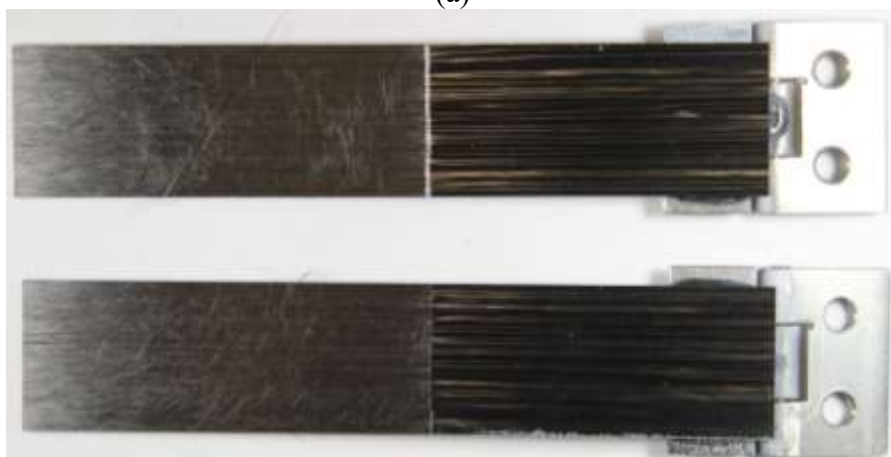


(b)

Fig. 5.19. Example image of DCB specimen prior to testing (a) Top surface showing specimen width (b) Side of specimen showing thickness



(a)



(b)

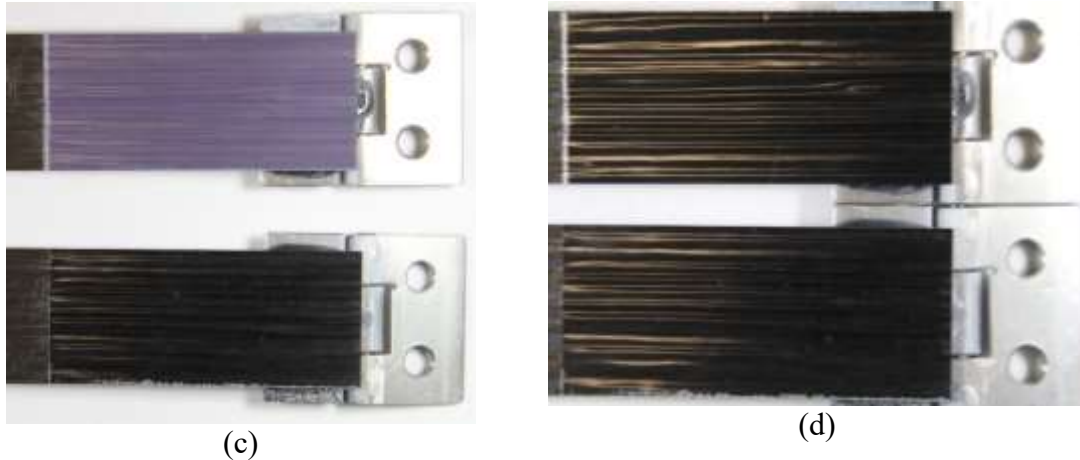


Fig. 5.20. Example image of DCB specimen after testing (a) Exterior top and bottom surfaces (b) Interior surfaces (c) Film (d) Initial crack area

Test Results: The experimental results for the measured load and displacement that occurred at the load point are shown in Fig. 5.21.

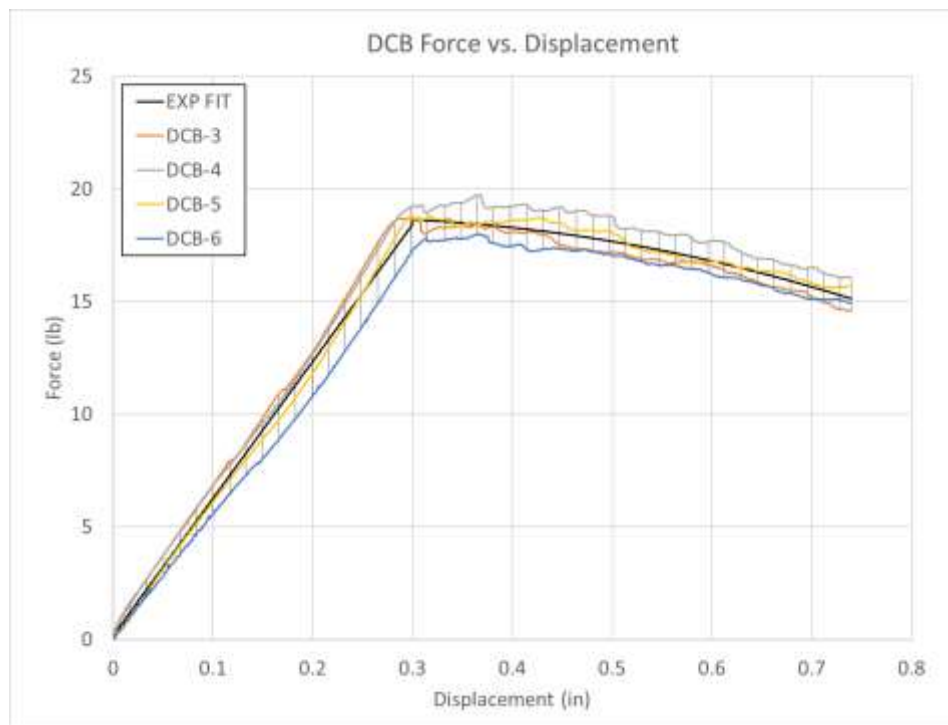


Fig. 5.21. DCB precrack experimental force vs. displacement

Four experimental curves are shown for test specimens with the precrack procedure. The experimental data across each replicate was fitted using polynomial

regression to form an experimental model curve. This is labeled at “EXP FIT” in Fig.

5.21. The whisker plot depicts the range of the experimental data. The specifications of the regression are given in Table 5.7.

Table 5.7. DCB Experimental Regression Specifications

Section	Fit Type	R ²
Pre-peak	Linear	0.981
Post-peak	Quadratic	0.756

The summary of the results from the non-precracked tests is shown in Table 5.8.

Table 5.8. Test Summary for DCB Non-precracked Tests

NPC				
Name	MAX G _{IC} [lb-in/in ²]			
	MBT	MBT w/ Rot Correction	CC	MCC
TFDCB-3	4.70	3.31	3.64	3.31
TFDCB-4	4.83	3.38	3.50	2.30
TFDCB-5	4.15	2.71	2.99	3.25
TFDCB-6	5.24	3.06	4.99	4.99
Average	4.73	3.11	3.78	3.46
Standard Deviation	0.45	0.30	0.85	1.12
Coefficient of Variation (%)	9.51	9.78	22.57	32.35

The summary of the results from the precracked tests are separated into three tables each for the different measures for the G_{IC} value. Table 5.9 shows the results for the non-linear G_{IC} measure for the precracked tests. This was the measure of G_{IC} when the force vs. displacement relationship of the test becomes non-linear.

Table 5.9. Test Summary for DCB Precracked Tests – Non-linear

PC				
Name	NL G _{IC} [lb-in/in ²]			
	MBT	MBT w/ Rot Correction	CC	MCC
TFDCB-3	2.66	2.07	2.24	2.07
TFDCB-4	2.96	2.24	2.35	2.25
TFDCB-5	3.10	2.25	2.40	2.27
TFDCB-6	2.73	2.17	2.26	2.17
Average	2.86	2.18	2.31	2.19

Standard Deviation	0.20	0.08	0.08	0.09
Coefficient of Variation (%)	7.11	3.88	3.34	4.17

Table 5.10 shows the results for the visible G_{IC} measure for the precracked tests. This is the measure of G_{IC} when the crack propagation from the initial crack becomes visible.

Table 5.10. Test Summary for DCB Precracked Tests – Visible

PC				
Name	VIS G_{Ic} [lb-in/in ²]			
	MBT	MBT w/ Rot Correction	CC	MCC
TFDCB-3	2.83	2.20	2.38	2.20
TFDCB-4	3.09	2.34	2.46	2.35
TFDCB-5	3.11	2.26	2.41	2.29
TFDCB-6	2.77	2.20	2.29	2.21
Average	2.95	2.25	2.39	2.26
Standard Deviation	0.18	0.07	0.07	0.07
Coefficient of Variation (%)	6.00	2.96	2.93	2.95

Table 5.11 shows the results for the maximum G_{IC} measure for the precracked tests. This is the measure of G_{IC} when the peak force is reached.

Table 5.11. Test Summary for DCB Precracked Tests – Maximum

PC				
Name	MAX G_{Ic} [lb-in/in ²]			
	MBT	MBT w/ Rot Correction	CC	MCC
TFDCB-3	3.04	2.38	2.56	2.42
TFDCB-4	3.63	2.81	2.88	2.86
TFDCB-5	3.22	2.37	2.50	2.40
TFDCB-6	3.16	2.55	2.61	2.57
Average	3.26	2.53	2.65	2.56
Standard Deviation	0.25	0.21	0.17	0.21
Coefficient of Variation (%)	7.81	8.13	6.40	8.22

The crack resistance curves for the duration of the tests are shown in Fig. 5.22.

This plots the strain energy release rate against the crack length for the PC tests.

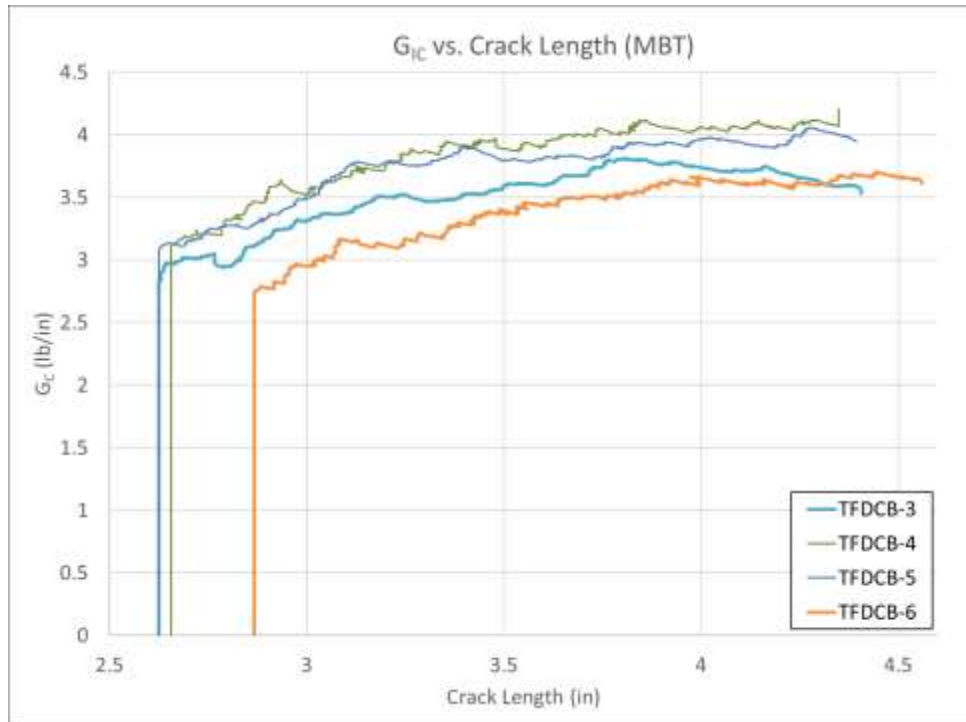


Fig. 5.22. DCB tests crack resistance curve

The opening displacement at the location of the original crack tip is also calculated using DIC. Fig. 5.23 shows the strain energy release rate plotted against the crack tip opening displacement for the PC tests.

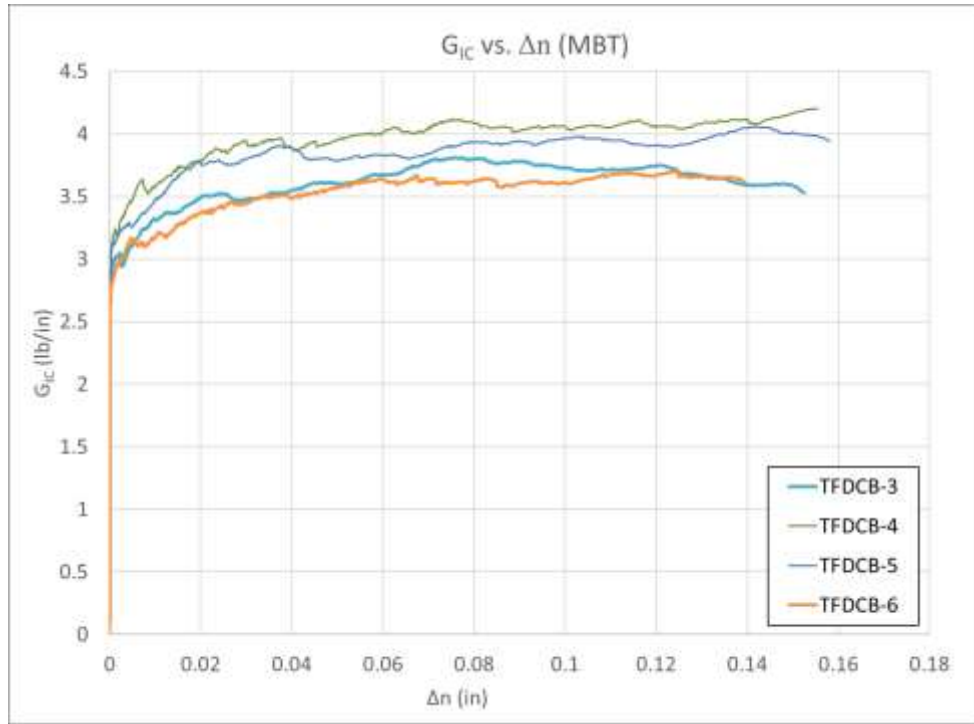


Fig. 5.23. GIC versus crack tip opening displacement

5.4 Simulation Details

Models were created in LS-DYNA for both the ENF and DCB tests. The purpose of modeling these tests was to use simulations alongside experimental data to calibrate the remaining parameters of MAT138, used for modeling cohesive zone elements. Values of G_{IC} and G_{IIC} were determined experimentally, while values for EN, ET, T, and S were not directly determined experimentally, thus calibration by simulation was required.

In both the ENF and DCB tests, a stroke displacement and a measured force were reported by the MTS machine. Simulations of each test were created to yield the same output, force and displacement, as the experimental test. For each test, the values of EN, ET, T, and S were varied in a series of simulations to determine the parameter values that produced the best match of the experimental force vs. displacement relationships.

The geometry and boundary conditions of the models were chosen so as to best represent the conditions present in the experimental tests. The geometry and boundary conditions of the experimental ENF test are shown in Fig. 5.24 when viewing the front face of the test coupon.

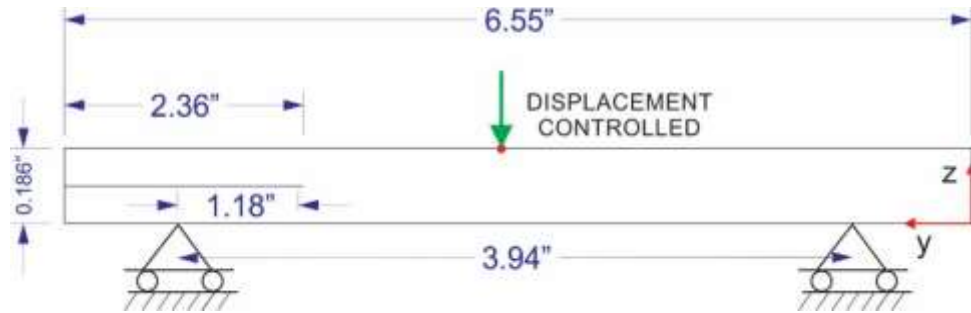


Fig. 5.24. ENF experimental geometry and BC's

For the simulation, only the portion of the test coupon between the left and right rollers was simulated. The overhangs are not included in the simulation because they are outside of the boundary conditions and have much shorter lengths than the main span, thus they have little effect on the results of the study. The geometry and boundary conditions of the simulated ENF test are shown in Fig. 5.25.

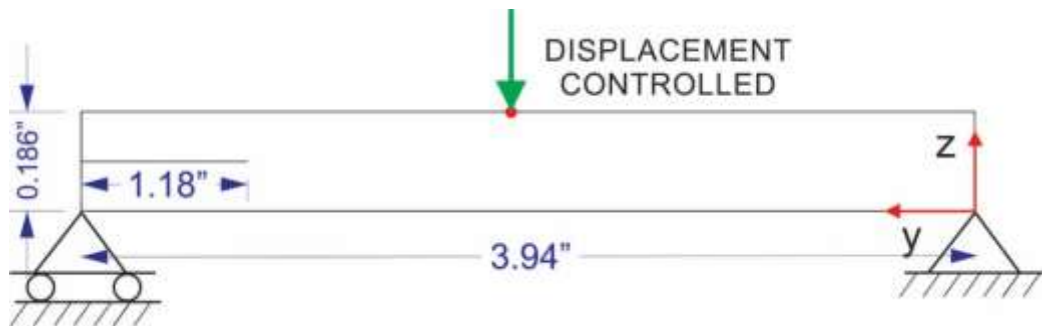


Fig. 5.25. ENF simulation geometry and BC's

The geometry and boundary conditions of the experimental DCB test are shown in Fig. 5.26.

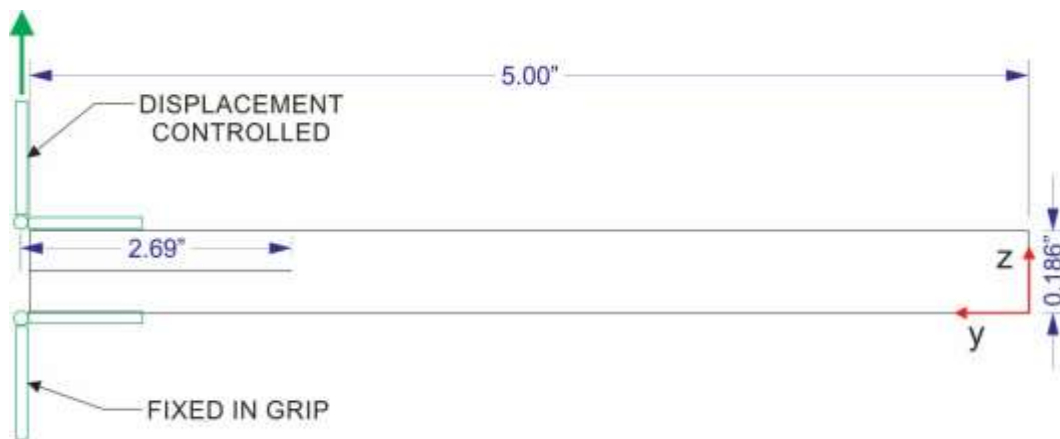


Fig. 5.26. DCB experimental geometry and BC's

The full geometry of the DCB test was modeled in the LS-DYNA simulation. The geometry and boundary conditions are shown in Fig. 5.27.

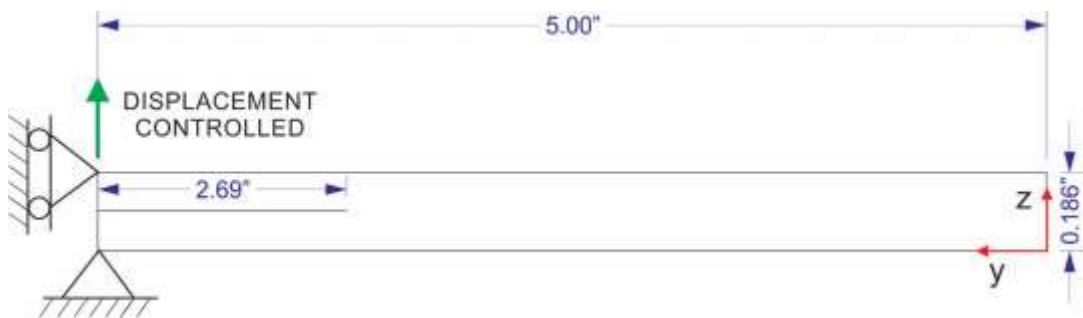


Fig. 5.27. DCB simulation geometry and BC's

Multiple models were made with varying degrees of complexity and mesh sizes. These are listed in Table 5.12.

Table 5.12. ENF and DCB Meshes

Mesh Number	# of Cohesive zone Layers	# of Elements between cohesive layers	Size of Elements in XY plane	Solid element size ratio (X:Y:Z)
1	1	2	0.06	(3:3:2)
2	1	4	0.03	(3:3:2)
3	7	1	0.03	(3:3:2)
4	23	1	0.06	(8:8:1)

As expected, modeling with fewer cohesive zone layers improved the computational throughput and allowed for rough calibration of the DCB and ENF parameters. However, it was found that the number of cohesive zone layers did have a significant effect on the results of the simulation. Thus, the final model included all 23 cohesive zone layers that existed in the experimental coupons. The model with 23 cohesive zone layers was superior because it best represented the experimental conditions. The experimental test coupon had 24 layers of unidirectional fibers and thus had 23 interlaminar layers. Since the number of cohesive zone layers in the model was observed to significantly affect the compliance of the specimen, it was necessary to include all the layers.

Mesh 3 was used to perform a sensitivity study on the effect of altering each of the six ENF and DCB parameters needed for the traction separation laws. Though this model didn't match the experimental data as well because only 7 cohesive layers were modeled, it allowed the observation of the effects of tuning each parameter.

An example of DCB Mesh 1 is shown in Fig. 5.28.

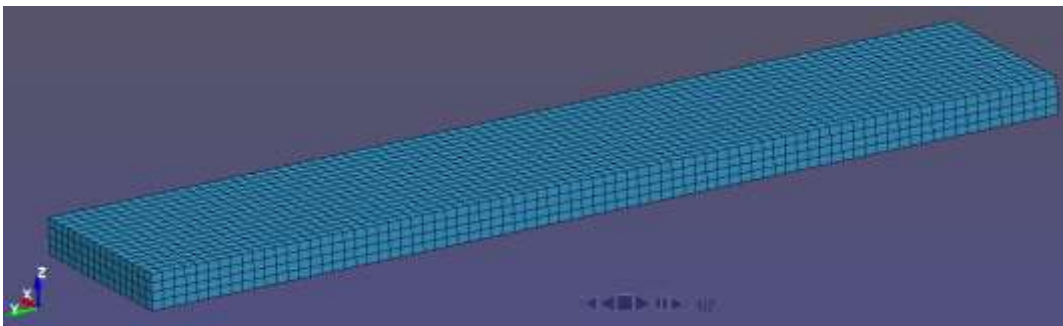


Fig. 5.28. DCB Mesh 1 - 1 cohesive zone layer

An example of DCB Mesh 4 is shown in Fig. 5.29.

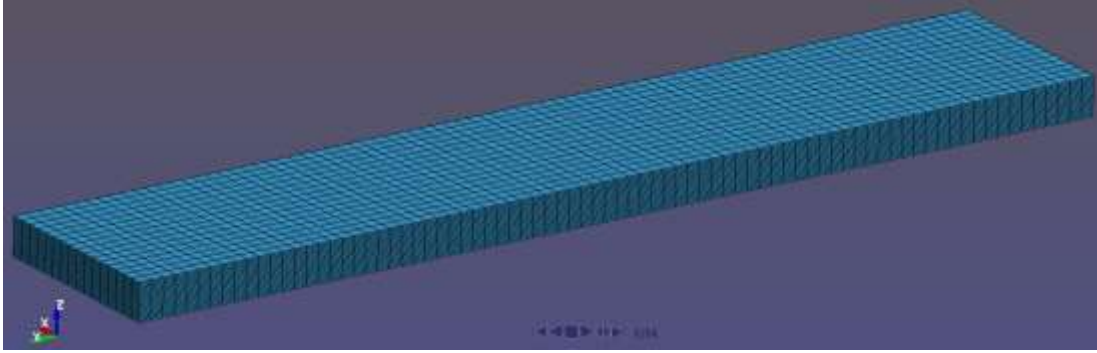


Fig. 5.29. DCB Mesh 4 - 23 cohesive zone layers

Other parameter specifications related to the simulations are shown in Table 5.13.

Table 5.13. ENF and DCB Simulation Specifications

Parameter	ENF	DCB
Integration scheme	Elform = 2, fully integrated	Elform = 2, fully integrated
Hourglassing control	Incorporated, IHQ=6, QH=0.1	Incorporated, IHQ=2, QH=0.1
Mass scaling	Incorporated, TSSFAC = 0.9, DT2MS = $-2.444(10)^{-8}$	Incorporated, TSSFAC = 0.9, DT2MS = $-2.444(10)^{-8}$
Displacement-controlled input	3 in/s	5 in/s
Termination time	0.05 s	0.12 s
Platform	Linux, ASU Agave Cluster	Linux, ASU Agave Cluster
Material model of composite	MAT22	MAT22 and MAT213
MAT213 version	N/A	V1.3 α -1

MAT213 was only used to model the composite material for the DCB test, and not the ENF test, because of limitations in the current version of MAT213. An error in finding the value of the plastic multiplier occurs early in the ENF simulation with 23 cohesive zone layers using MAT213. Thus, only MAT22 was used to obtain simulation results for the ENF test. In simulations with only one cohesive zone layer, the plastic multiplier error did not occur. In these models MAT213 showed that there was very little plasticity in the test coupon during the simulation, thus MAT22 was a valid choice of material model as it is a linear elastic model. Since MAT213 was unable to be used for the ENF simulation, the DCB simulation was completed using both MAT22 and

MAT213 in different trials, to see how the change of material model affected the results. The MAT213 plastic multiplier error will be amended in the near future.

Sensitivity studies were conducted to determine the effect of changing each calibration parameter. A range of values were used across multiple simulations for each parameter while holding all other parameters constant. Using the force vs. displacement responses of the sensitivity study, values of the parameters were chosen that would produce the desired slope and peak force to match the experimental test values. The parameter values producing the best fit of the experimental slope and peak force were determine only by visual observation. However, the results of the sensitivity study will allow for a regression analysis to be completed to find the optimal values, this procedure is part of the future work of this research.

5.5 Simulation Results

5.5.1 ENF Test

Sensitivity studies were carried out for the stiffness and peak traction mode II parameters. The results of the sensitivity study are shown in Fig. 5.30.

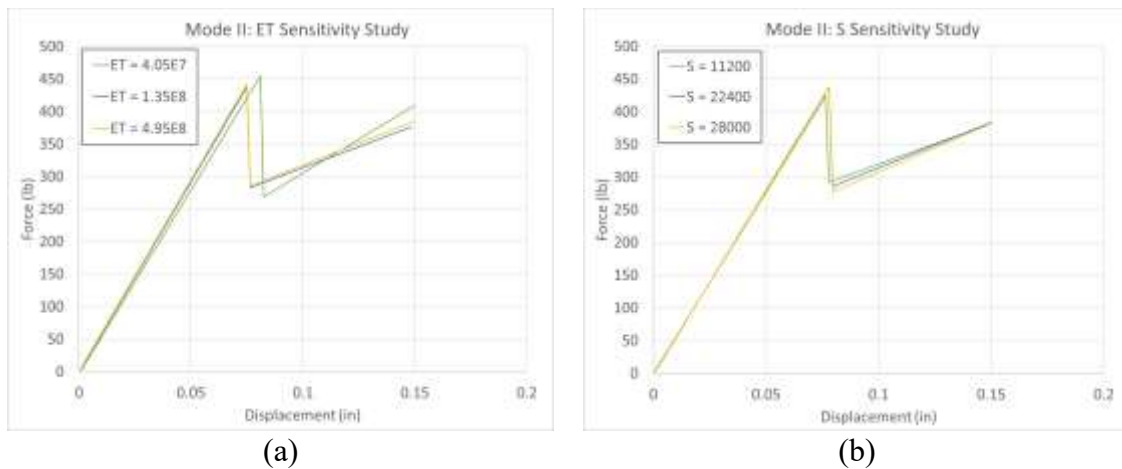


Fig. 5.30. Mode II sensitivity study (a) ET (b) S

Fig. 5.30(a) shows that a higher ET value led to a higher slope on the force displacement plot. Fig. 5.30(b) shows that the peak force was increased with a larger S value. In addition the larger values decreased the drop in force after the initial delamination.

The plot of force vs. displacement using the final parameter values is shown in Fig. 5.31. Due to limitations with the current implementation of MAT213, analysis errors were encountered and inhibited modeling with MAT213. MAT 22 was used for the solid elements in this model to complement the MAT 138 cohesive zone models.

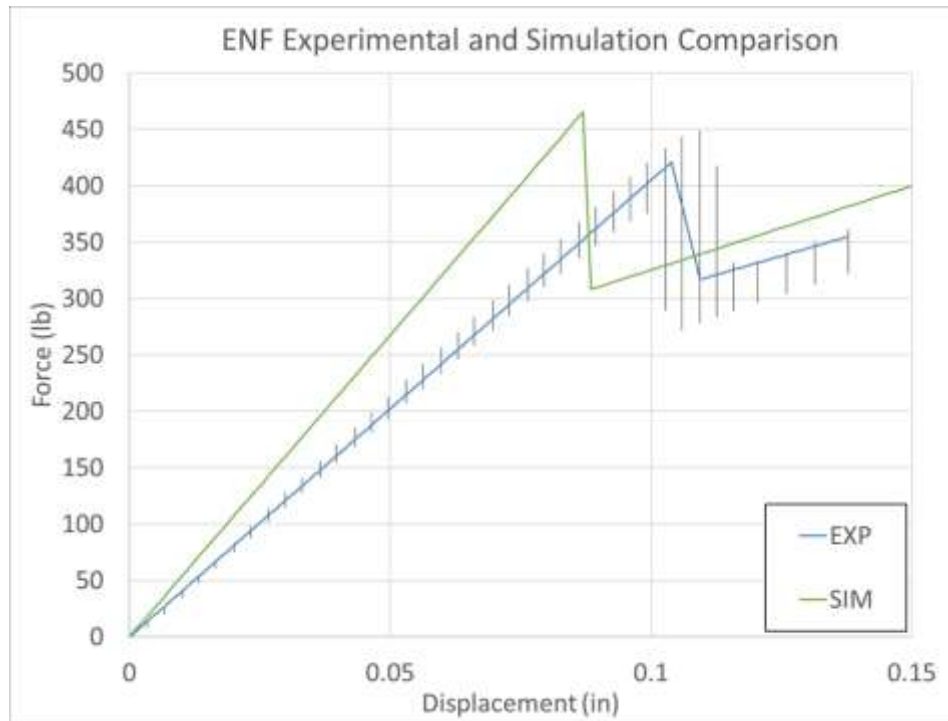


Fig. 5.31. Force vs. displacement simulation and experimental comparison

This figure shows that the slope of the force displacement is higher for the simulation than the experiment. This is partly due to the use of MAT22, in general models run with MAT213 yielded a lower slope. The simulation data was noisy and jagged, thus

it was fit using polynomial regression. The specifications of the regression are shown in Table 5.14.

Table 5.14. Simulation Regression Specifications

Section	Fit Type	R ²
Pre-peak	Linear	0.997
Post-peak	Linear	0.226

The final MAT 138 values for mode II are shown in Table 5.15.

Table 5.15. Final Mode II MAT 138 Parameters

Parameter	Value
ET	$4.50(10)^7$ psi/in
S	28000 psi
GIIC	10.50 lb-in/in ²

The traction separation curve produced by these final parameters values is shown in Fig. 5.32.

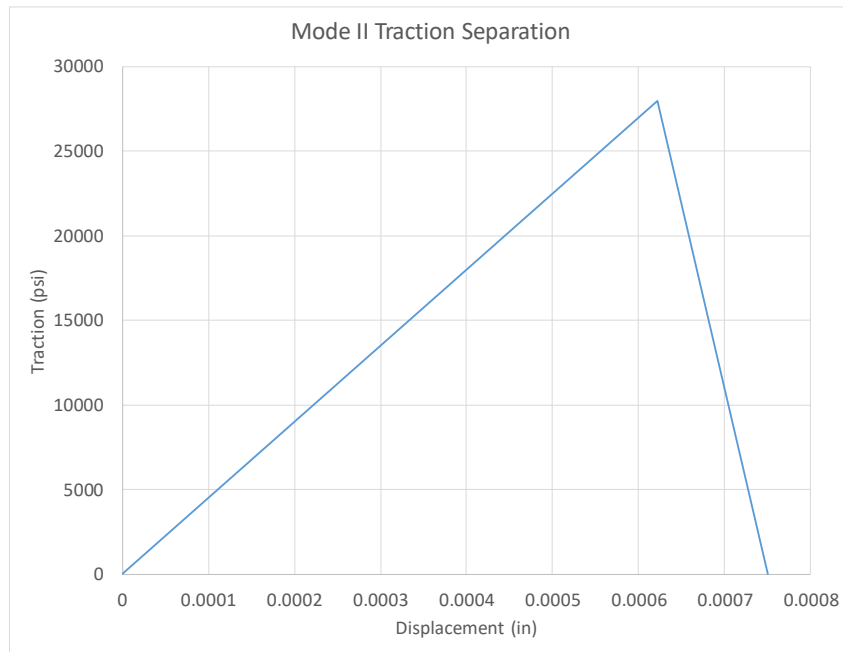


Fig. 5.32 Mode II Final Traction Separation Curve

5.5.2 DCB Test

Sensitivity studies were also carried out for the stiffness and peak traction mode I parameters. The results of the sensitivity study are shown in Fig. 5.30.

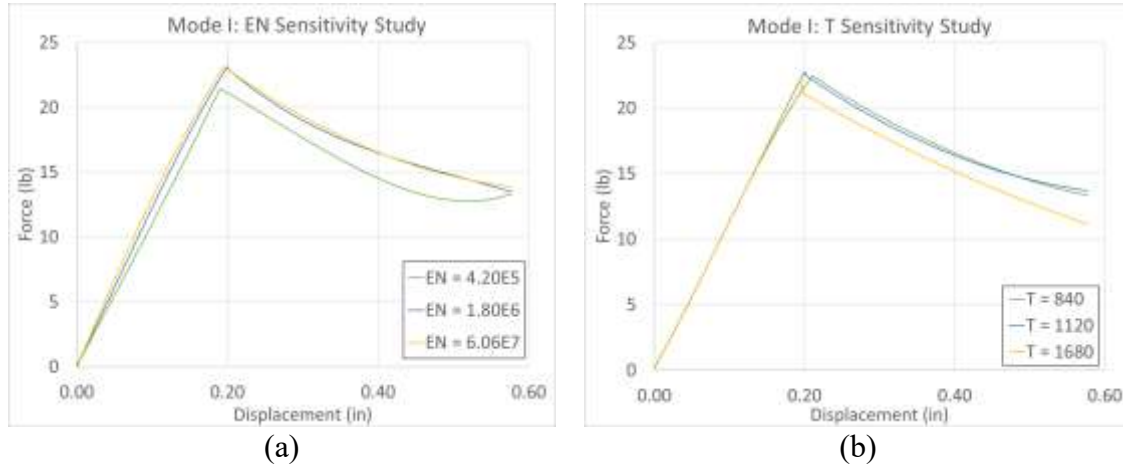


Fig. 5.33. Mode I sensitivity study (a) EN (b) T

Fig. 5.33(a) shows that a higher EN value led to a higher slope on the force displacement plot. Fig. 5.33(b) shows that the peak force was slightly increased with a larger T value.

Optimal values for each cohesive zone parameter were determined from the sensitivity study using a trial and error process. The plot of force vs. displacement using the final MAT138 values and using MAT213 to model the solid elements is shown in Fig. 5.34.

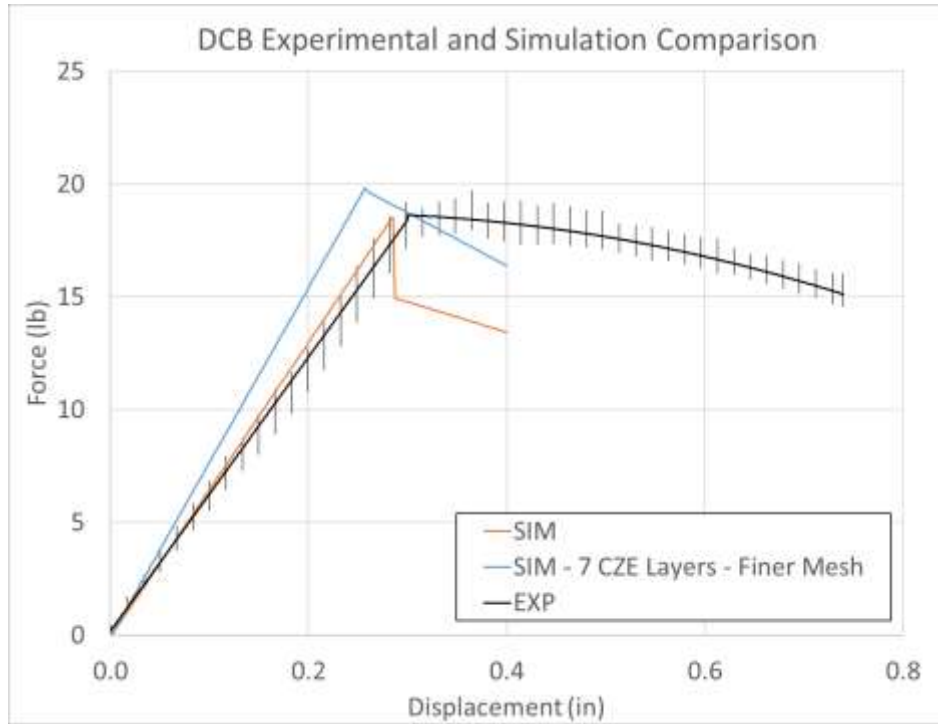


Fig. 5.34. Force vs. displacement simulation and experimental comparison

In Fig. 5.34 the curve labeled “SIM” was the result of the final model with 23 cohesive zone layers. The pre-peak response is within the experimental data range. However, there is a drop in the force after the linear peak force value that is not present in the experimental data. This drop in force was discovered to be a function of element size. The model with 23 cohesive zone layers was used with a coarse mesh to decrease simulation run time. A preliminary model with 7 cohesive zone layers but a finer mesh was found to produce results that did not feature this drop. The results of this model are shown in Fig. 5.34 and labeled “SIM – 7 CZE Layers – Finer Mesh”. Thus the element size was the cause of the discrepancy in the change in force at the beginning of crack propagation. Future work on the DCB model includes finding a balance between computational time and model performance. The simulation curve was noisy and jagged

and thus was fit using polynomial regression, the specifications of the regression are shown in Table 5.16.

Table 5.16. Simulation Regression Specifications

Section	Fit Type	R ²
Pre-peak	Linear	0.997
Post-peak	Linear	0.033

The final MAT 138 values for mode I are shown in Table 5.17.

Table 5.17. Final Mode I MAT 138 Parameters

Parameter	Value
EN	$6.00(10)^5$ psi/in
T	1400 psi
GIC	2.65 psi-in

The traction separation curve produced by these final parameters values is shown in Fig. 5.35.

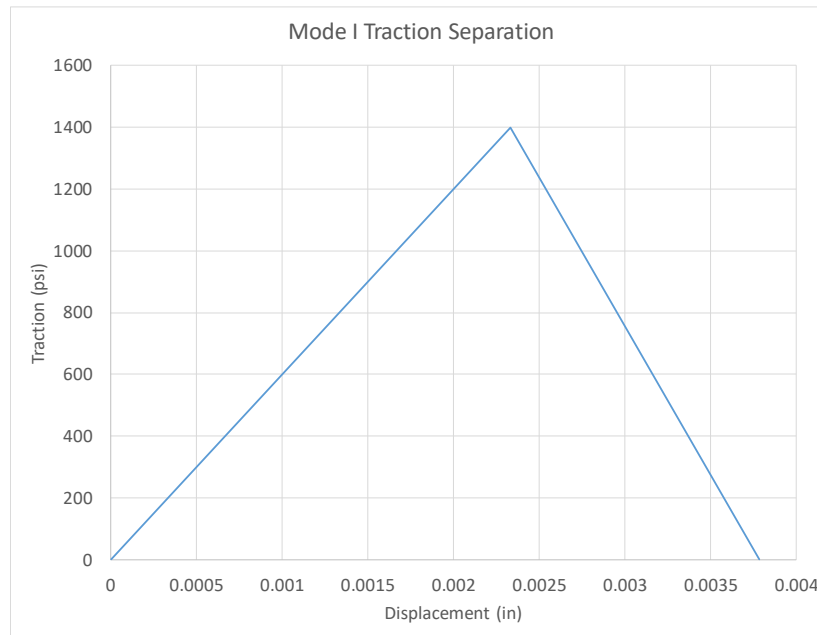


Fig. 5.35 Mode I Final Traction Separation Curve

Using the parameter values found through experimentation and simulation calibration, the final MAT138 input deck, used for the cohesive zone layers in the stacked-ply simulations, is shown in Table 5.18. The values are given in base units of pounds and inches.

Table 5.18 MAT138 Input Deck

Card 1	1	2	3	4	5	6	7	8
Variable	MID	RO	ROFLG	INTFAIL	EN	ET	GIC	GIIC
Value		$8.5(10)^{-8}$		1	$6.00(10)^5$	$4.50(10)^7$	2.65	10.50
Card 2	1	2	3	4	5	6	7	8
Variable	XMU	T	S	UND	UTD	GAMMA		
Value	1.0	1400	28000					

6. LS-DYNA Simulation of QS-RT Stacked-ply Validation Tests Using MAT213

6.1 LS-DYNA Simulation Overview

This section summarizes the stacked-ply simulations conducted as a portion of the validation testing for the MAT213 material model [MAT213 V1.3-alpha Rev # 123494].

Four types of stacked-ply simulations were performed to mirror the experimental tests - tension, compression, tension with stress concentration, and compression with stress concentration. These simulations serve to validate MAT213's deformation and damage sub-models.

Simulations of the stacked-ply validation tests were conducted using MAT213 to compare with the experimental tests. Modeling techniques and validation metrics used varied according to the test and are explained in the following sections.

In this section, the experimental results are presented as model experimental curves. The model curves were obtained by averaging the results of the test replicates for the respective stacked-ply tests. The stresses, strains, and displacements were averaged over the time duration of the experiments. The experimental data is also presented as a whisker curve, where the extents of the whisker depict the experimental data range.

6.2 General Modeling Techniques

The goal while modeling the stacked-ply tests was to recreate the conditions of the experimental tests as accurately as possible while maintaining computational efficiency. Because of a lack of symmetry in the test coupons due to the ply layup, a full model of each test was created. All 8 layers of the test coupons were modeled for the entire gage section of each test. An example of the XZ plane view of the model, showing all 8 plies, is shown for a coarse mesh in Fig. 6.1.

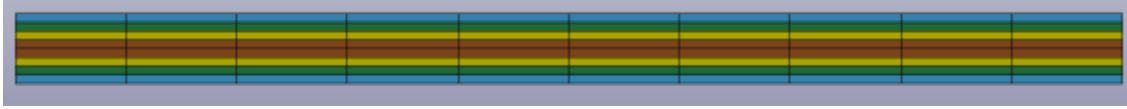


Fig. 6.1. Elevation XZ plane view of the FE model

Convergence analysis was conducted for each simulation using three meshes with decreasing element size and aspect ratio. Other parameters shared by all the models are listed in Table 6.1.

Table 6.1. Model Parameter Specifications

Parameter	Specification
Integration scheme	Elform = 2, fully integrated
Hourglassing control	Incorporated, IHQ=2, QH=0.1
Mass scaling	Incorporated, TSSFAC = 0.7, DT2MS = $-7.1429(10)^{-8}$
Displacement-controlled input	Varying, made equal to the displacement obtained from DIC extensometer
Termination time	Varying
Platform	Linux, ASU Agave Cluster
Material model for composite material	MAT213
Material model for cohesive zone	MAT138
MAT213 version	V1.3a-1
Damage model of MAT213	Only uncoupled 2-direction compression and uncoupled 12-plane shear are included.
Failure model of MAT213	Not incorporated

The extension of the specimen in the y direction was measured in the experimental test using a digital extensometer within Vic 3D software. This displacement vs. time plot was averaged over all of the experimental tests and then smoothed. The time values were scaled by a factor of 1/100,000 to create the final displacement vs. time plot for the displacement-controlled nodes in the simulation. The time-scaling was necessary to allow a reasonable computational time within LS-DYNA. During post-processing, the time values were re-scaled by a factor of 100,000 to allow for comparison with the experimental results. For example, the average experimental test duration for the tension

tests was 320 seconds, thus the simulation time was 0.00320 seconds. This time-scaling procedure was used for each of the test types. To validate the use of time-scaling, it was necessary to examine the energy effects of each simulation. An example of the energy induced in the simulation of the tension test is shown in Fig. 6.2.

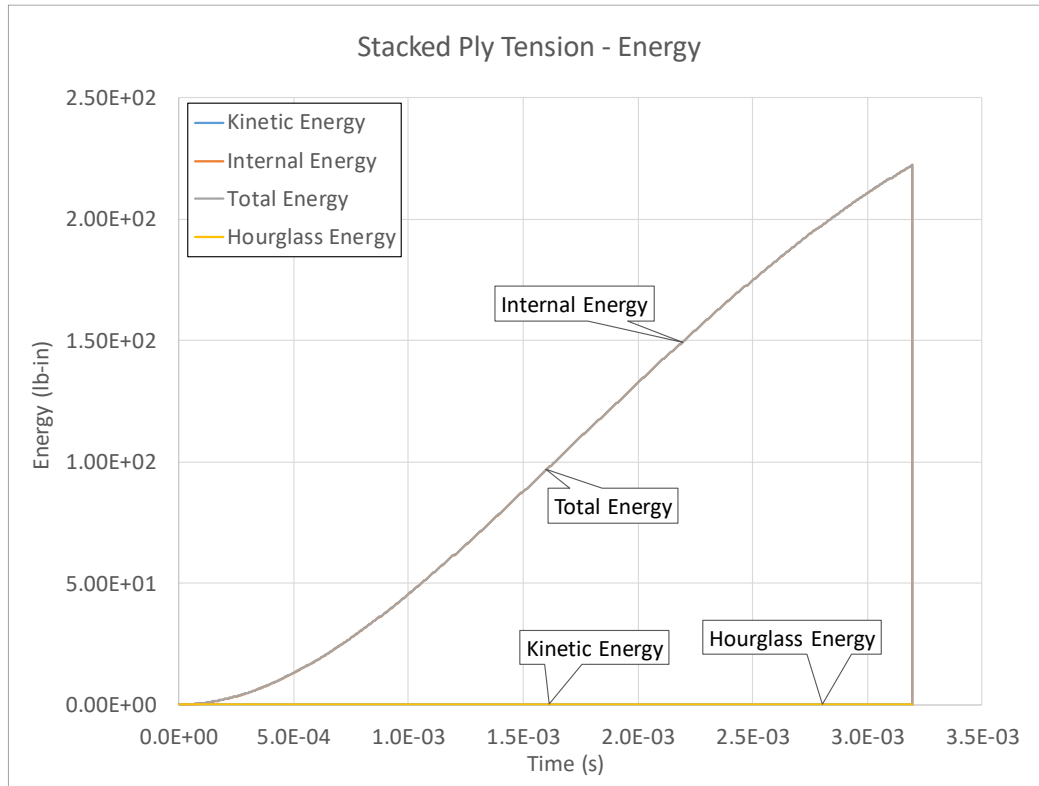


Fig. 6.2. Energy plot for tension simulation

For each simulation, energy plots were observed to verify that the kinetic energy remained a small portion of the total energy, as is the case in Fig. 6.2. The same energy checks were used in this study as employed by Deivanayagam et al. [34] in a study on dry fabric modeling.

For each validation test, 3 meshes were created with decreasing element size. Simulations were run with the coarse, medium, and fine meshes to show convergence of the results with decreasing element size. Only results from the fine meshes are shown.

Data extracted from the simulations was often jagged and choppy. In order to make meaningful comparisons between the experimental and simulated data, the simulated data was smoothened via polynomial regression fitting. The details of each polynomial fit are given in the following sections.

The interlaminar layers of the test coupons were modeled using material model MAT138. The parameters of the model were the final parameters obtained from the ENF and DCB test delamination studies as shown in Table 5.18.

Specific modeling techniques of each test are detailed in subsequent sections.

6.3 LS-DYNA Simulation of Stacked-ply Tension

6.3.1 Simulation Modeling

The overall geometry as well as boundary and loading conditions of the experimental test are shown in Fig. 6.3 and Fig. 6.4. Only the gage section of the specimen is shown.



Fig. 6.3. Experimental test conditions, XY plane

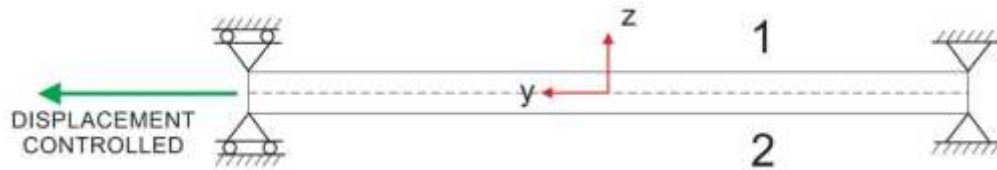


Fig. 6.4. Experimental test conditions, YZ plane

The geometry as well as boundary and loading conditions for the MAT213 simulations are shown in Fig. 6.5 and Fig. 6.6.

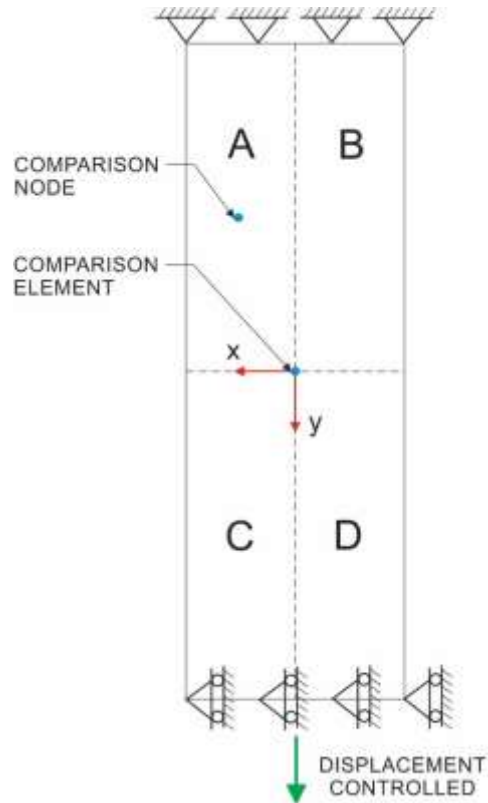


Fig. 6.5. Simulation test conditions, XY plane

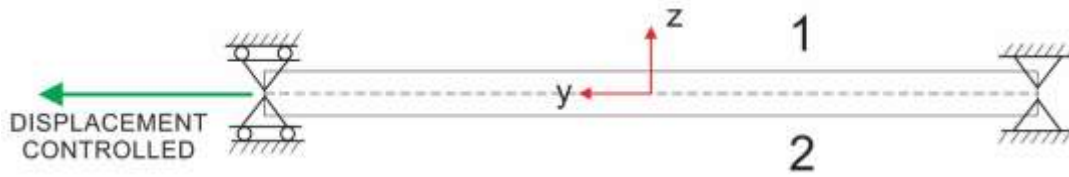
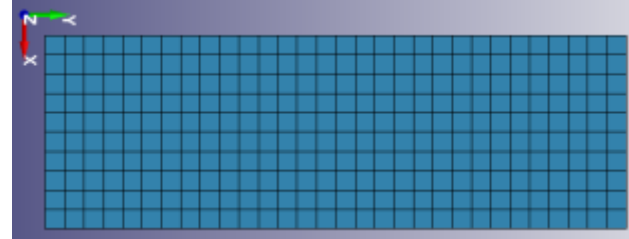
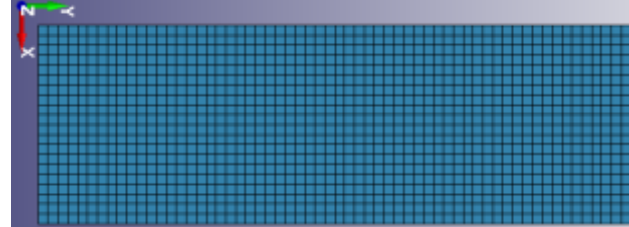
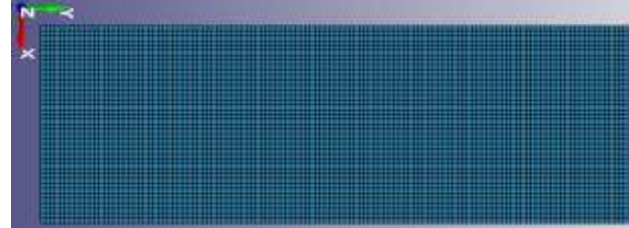


Fig. 6.6. Simulation test conditions, YZ plane

Three finite element (FE) models were created with varying element sizes, these are depicted in Table 6.2. The plies were modeled using MAT213. The interface between each ply was modeled using cohesive zone elements. The cohesive elements were modeled using MAT138.

Table 6.2. FE Model Meshes

Mesh	# of MAT213 elements	# of cohesive elements	XY Plane view of FE model

Coarse	2400	2100	
Medium	9600	8400	
Fine	38400	33600	

6.3.2 Validation Metrics

The simulation tests were validated with three distinct metrics comparing the simulation and experimental values. These metrics are outlined in Table 6.3.

Table 6.3. Validation Metrics Description

Metric	Description
1	Comparison of strains for the 0 ⁰ -ply of an element which was centrally located in the simulation model (Fig. 6.5). The strains ϵ_{xx} and ϵ_{yy} were plotted against time.
2	Comparison of displacement for the 0 ⁰ -ply of a node which was centrally located in Quadrant A of the simulation model (Fig. 6.5). The x and y displacements were plotted against time.
3	Comparison of the average (longitudinal) stress in the Y direction, σ_{yy} , plotted against the (longitudinal) strain in the Y direction, ϵ_{yy} .

A comparison of how the data was captured in the experimental and simulation tests for Metric 1 is shown in Table 6.4.

Table 6.4. Tension Test Metric 1

Data Type	Method of Data Collection
Experimental	Strains were computed using a DIC strain gage section as shown in Fig. 3.5.
Simulation	Strains were taken from an element that was located centrally in the gage section of the 0 ⁰ -ply as shown in Fig. 6.5.

A comparison of how the data was captured in the experimental and simulation tests for Metric 2 is shown in Table 6.5.

Table 6.5. Tension Test Metric 2

Data Type	Method of Data Collection
Experimental	Displacements were calculated using virtual extensometers with DIC. The y displacement was calculated using an extensometer that extends in the Y direction from the fixed end to the point of interest. The x displacement was calculated using an extensometer that extends in the X direction from the specimen centerline to the point of interest. These digital extensometers are shown in Fig. 6.7.
Simulation	Displacements were taken from a node that was located centrally in quadrant A of the 0 ⁰ -ply, as shown in Fig. 6.5



Fig. 6.7 VIC 3D digital extensometers used for metric 2

Metric 3

A comparison of how the data was captured in the experimental and simulation tests for Metric 3 is shown in Table 6.6.

Table 6.6. Tension Test Metric 3

Data Type	Method of Data Collection
Experimental	The experimental data for σ_{yy} was obtained using equation (1). The strain value was the same ϵ_{yy} used for metric 1. The force used to obtain the stress was the force recorded from the MTS test machine
Simulation	The simulation data for σ_{yy} was obtained by recording and taking the summation of the Y force for every node that was restrained in the Y direction. The forces were summed and divided by the original area of model in the XZ plane. The simulation data for ϵ_{yy} was the same which was used for metric 1. The nodes used to compute the force are shown in Fig. 6.8

The nodes used to obtain the reactions the Y direction for the simulation are shown in Fig. 6.8.

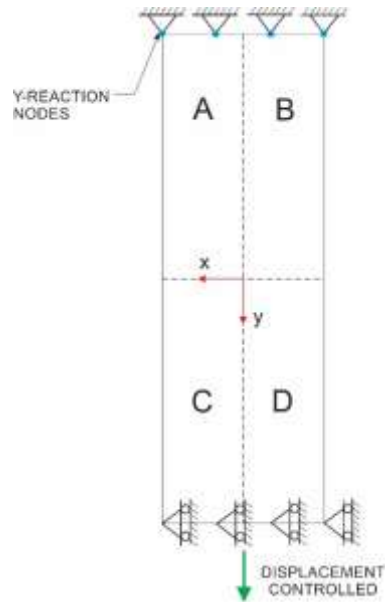


Fig. 6.8. Metric 3 y-reaction nodes

6.3.3 Results

Fig. 6.9 and Fig. 6.10 show the results for Metric 1.

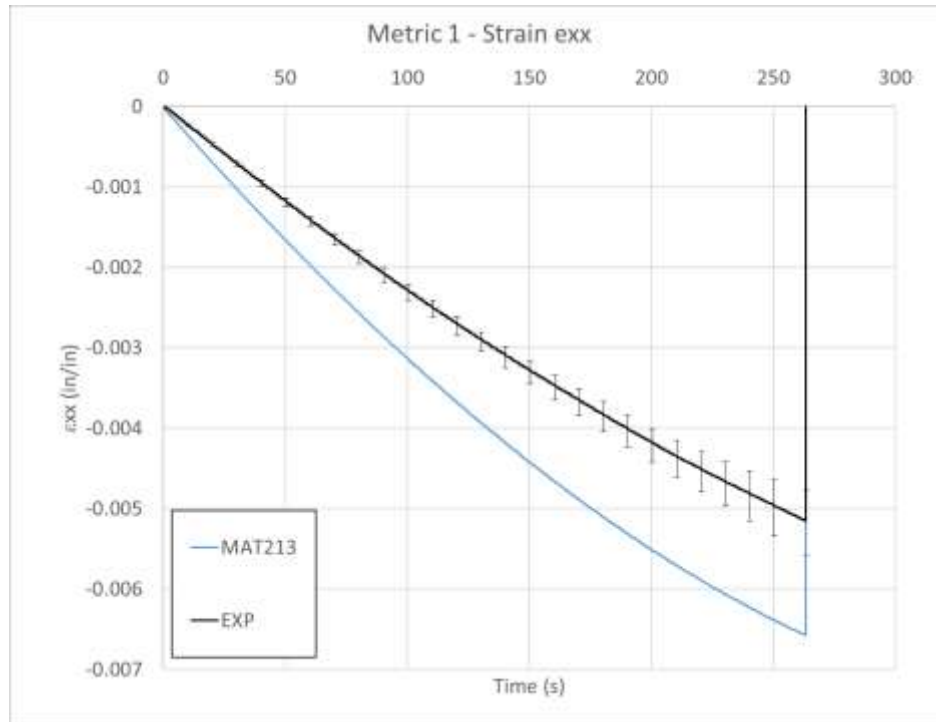


Fig. 6.9. Metric 1 - ϵ_{xx} comparison

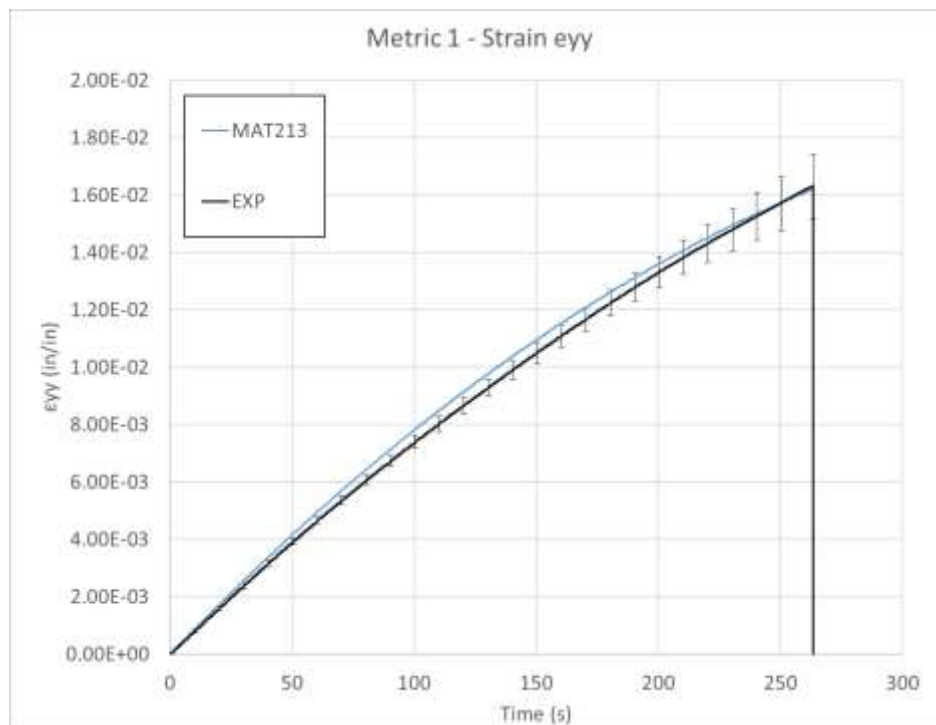


Fig. 6.10. Metric 1 - ϵ_{yy} comparison

Fig. 6.11 and Fig. 6.12 show the results for Metric 2.

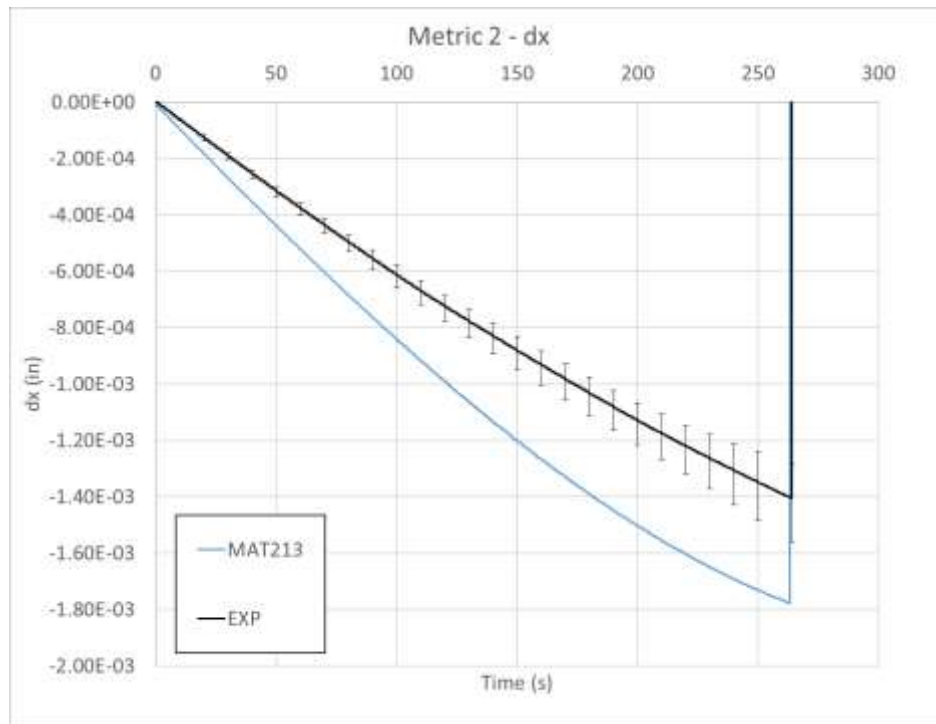


Fig. 6.11. Metric 2 - x-displacement comparison

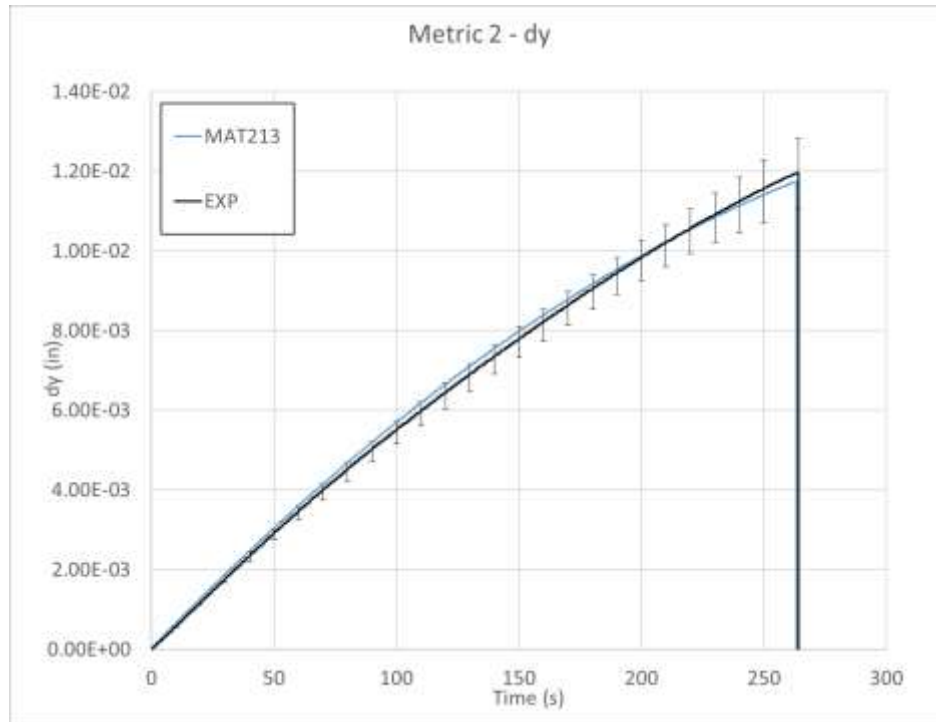


Fig. 6.12. Metric 2 - y-displacement comparison

Fig. 6.13 shows the results for Metric 3.

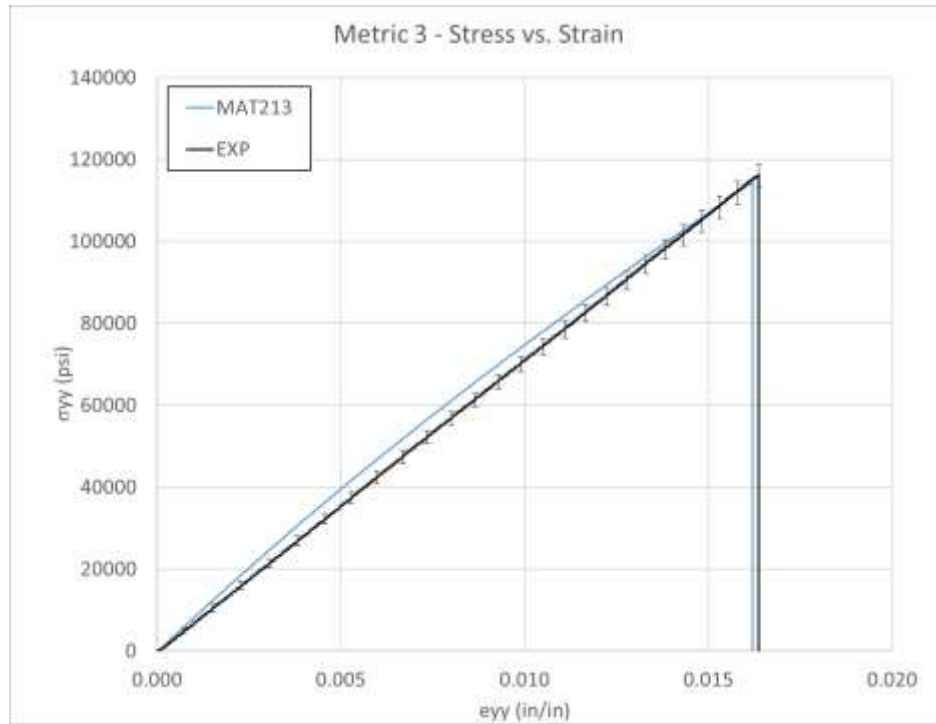


Fig. 6.13. Metric 3 - stress-strain comparison

A fringe plot of the y-strain is pictured in Fig. 6.14. The range and color scheme depicting the strain field is identical for the simulation (a) and the experiment (b). The experimental plot shows a higher strain along the right edge of the test coupon. However, the range of strain magnitude and the average strain value in the gage section match well.

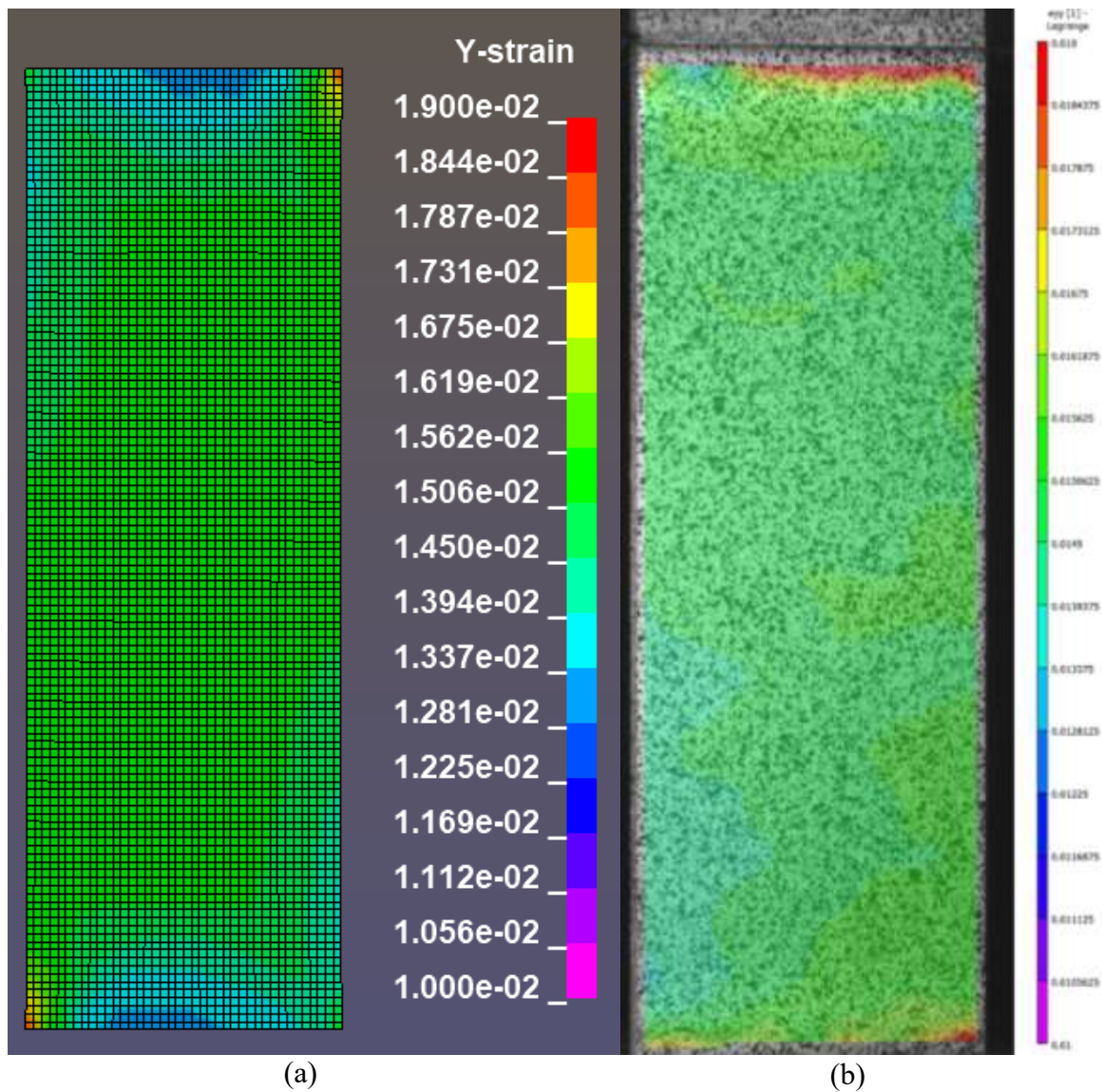


Fig. 6.14. Y-Strain fringe plot of tension test, at $t = 250$ s (a) Simulation (b) Experiment

6.3.4 Discussion

Several of the simulation curves used for comparison had data that was fitted using polynomial regression. The details of the polynomial regressions are shown in Table 6.7.

Table 6.7 Polynomial Regression Fitting of Tension Simulation Metrics

Metric	Order of polynomial regression	R-squared of regression	Fig. #
Metric 1 – Strain ϵ_{xx}	Cubic	0.9998	Fig. 6.9
Metric 1- Strain ϵ_{yy}	Cubic	0.9998	Fig. 6.10
Metric 2 - Δx	Cubic	0.9995	Fig. 6.11
Metric 2 – Δy	Cubic	0.9998	Fig. 6.12
Metric 3 – Stress-Strain	Quadratic	0.9991	Fig. 6.13

Metric 1 indicated that the MAT213 simulation over-predicted the transverse strain, while giving an excellent prediction of the longitudinal strain. The longitudinal strain was in this case, nearly a magnitude of order larger than the transverse strain, thus MAT213 better predicted the larger strain value.

Metric 2 indicated that the MAT213 simulation over predicted the transverse displacement measure in the experiment, while it has a good prediction of the longitudinal displacement. The MAT213 simulation showed nonlinearity in the transverse displacement response towards the end of the simulation, which was present in some but not all of the experimental tests.

Metric 3 indicated that the MAT213 simulation displayed some nonlinearity in the stress-strain response, while the experimental tests showed only linear relationships. The MAT213 response is slightly stiffer than the experimental results initially, the stiffness is reduced during the test and the final stress value is very similar to that of the experimental tests.

The transverse direction strains and displacements are approximately one magnitude of order lower than those in the longitudinal direction. The error seen in the transverse direction metrics may be due to this low magnitude and the limitations of the DIC software in capturing these small displacements and strains.

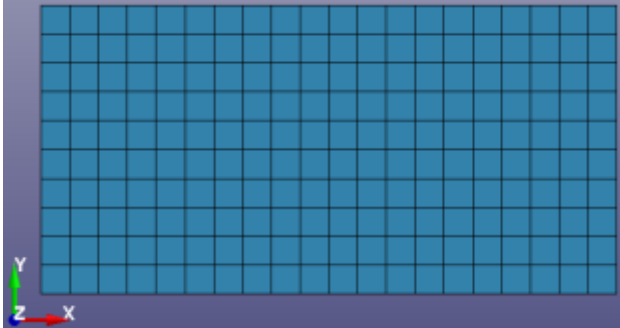
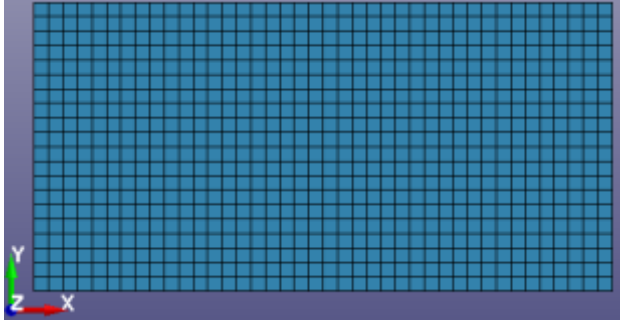
6.4 LS-DYNA Simulation of Stacked-ply Compression

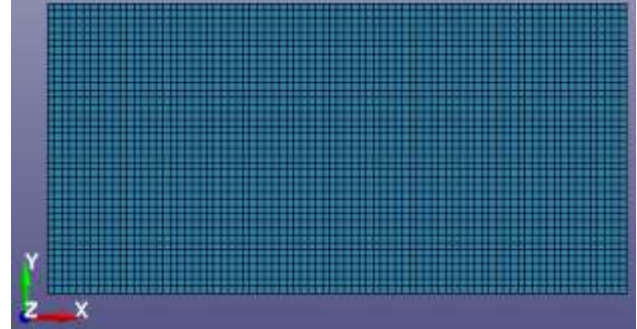
6.4.1 Simulation Modeling

Only the gage area of the experimental test was considered for the simulations. Thus, the experimental and simulation modeling and fixity conditions was the same as for the stacked-ply tension tests. The dimensions of gage area were different, but the overall geometry was the same.

Three finite element (FE) models were created with varying element sizes, these are depicted in Table 6.8.

Table 6.8. FE Model Meshes

Mesh	# of MAT213 elements	# of cohesive elements	XY Plane view of FE model
Coarse	1600	1400	
Medium	6400	5600	

Fine	25600	22400	
------	-------	-------	--

6.4.2 Validation Metrics

The validation metrics and data collection methods were the same as for the stacked-ply tension tests except for a minor change in the evaluation of metric 2. Since the compression specimen has a shorter gage section and failed earlier than the tension specimen, the displacements to induce failure were small. Thus, the node chosen to compare displacement was in the center of the gage section in the y-direction. This gives a higher displacement than the position of the node in the tension comparison. The higher displacement resulted in lower error from experimental data collection. The location of the comparison node for metric 2 and the comparison element for metric 1 are shown in Fig. 6.15.

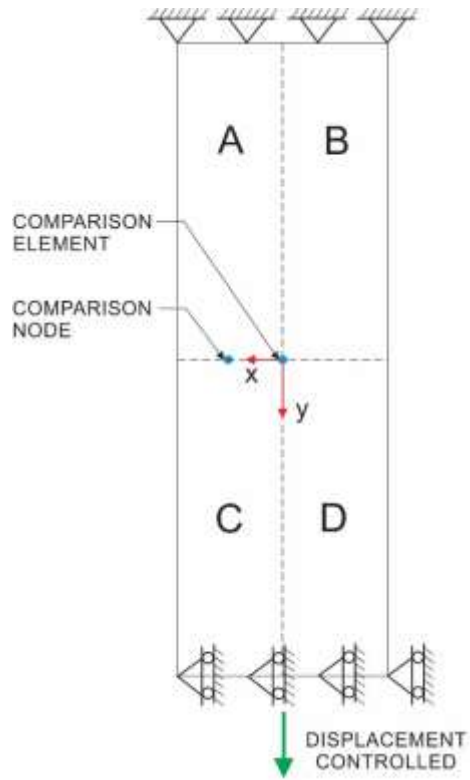


Fig. 6.15. Compression comparison node and element

6.4.3 Results

Fig. 6.16 and Fig. 6.17 show the results for Metric 1.

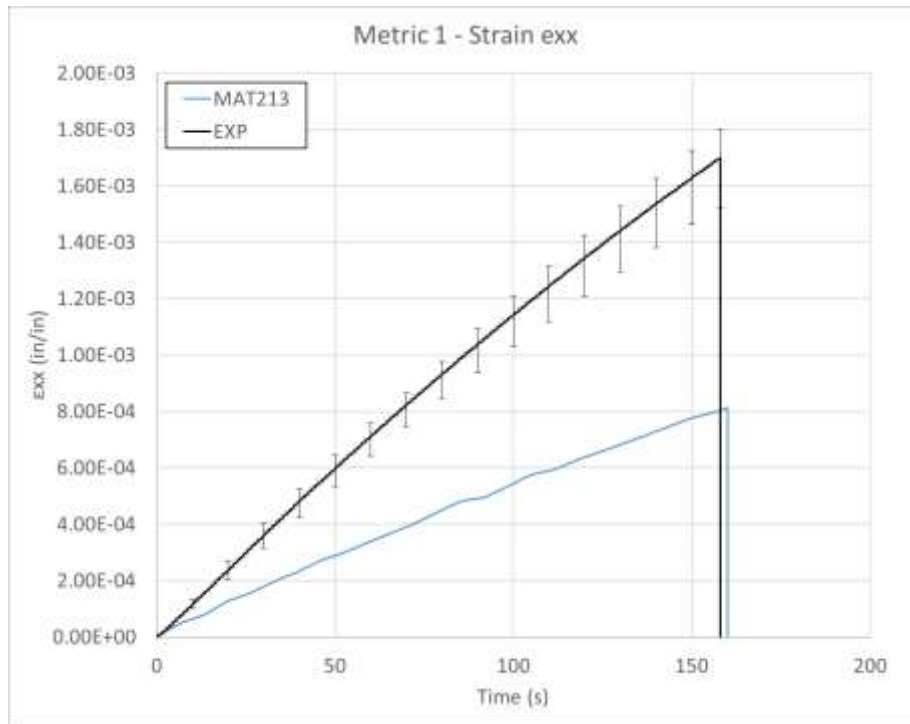


Fig. 6.16. Metric 1 - ϵ_{xx} comparison

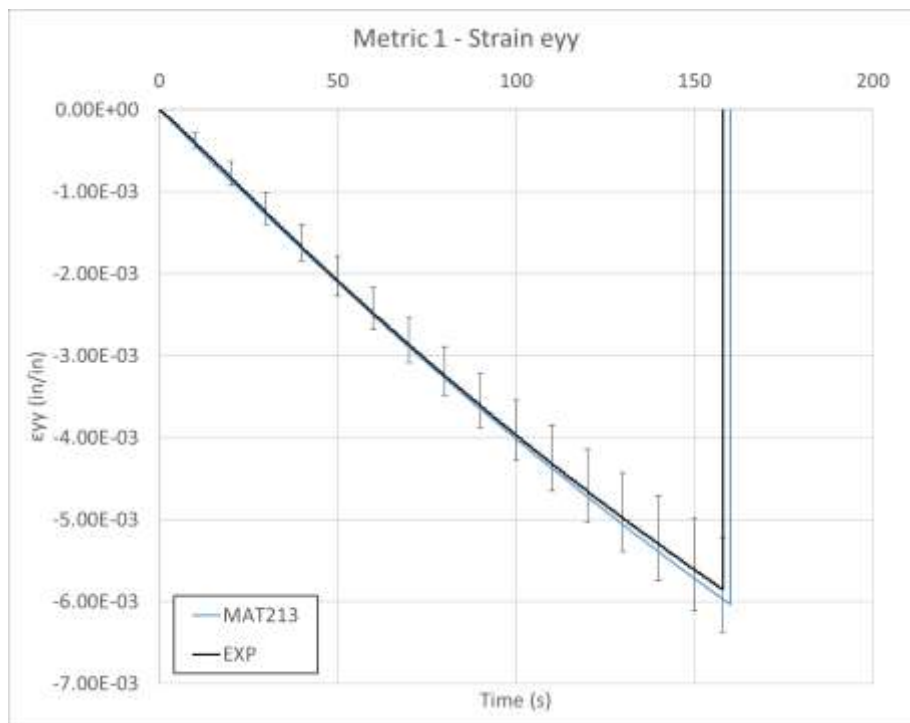


Fig. 6.17. Metric 1 - ϵ_{yy} comparison

Fig. 6.18 and Fig. 6.19 show the results for Metric 2.

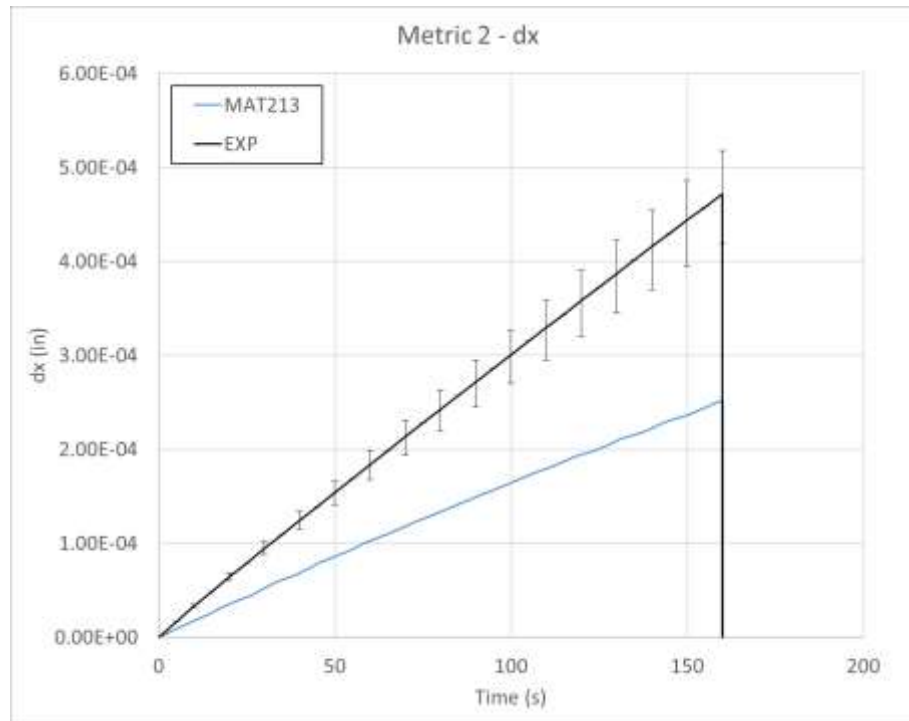


Fig. 6.18. Metric 2 - x-displacement comparison

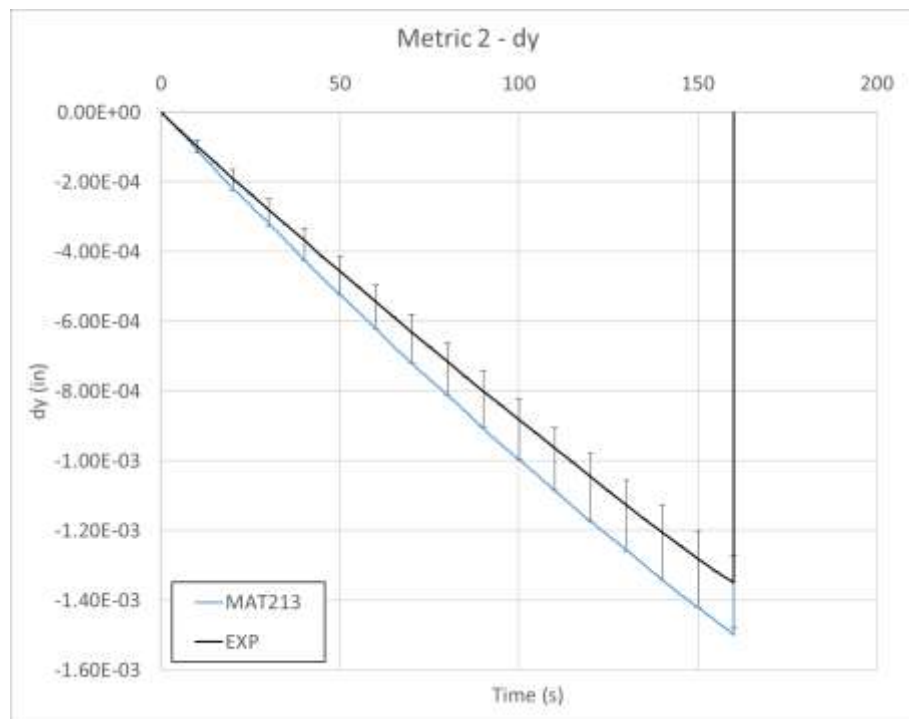


Fig. 6.19. Metric 2 - y-displacement comparison

Fig. 6.20 shows the results for Metric 3.

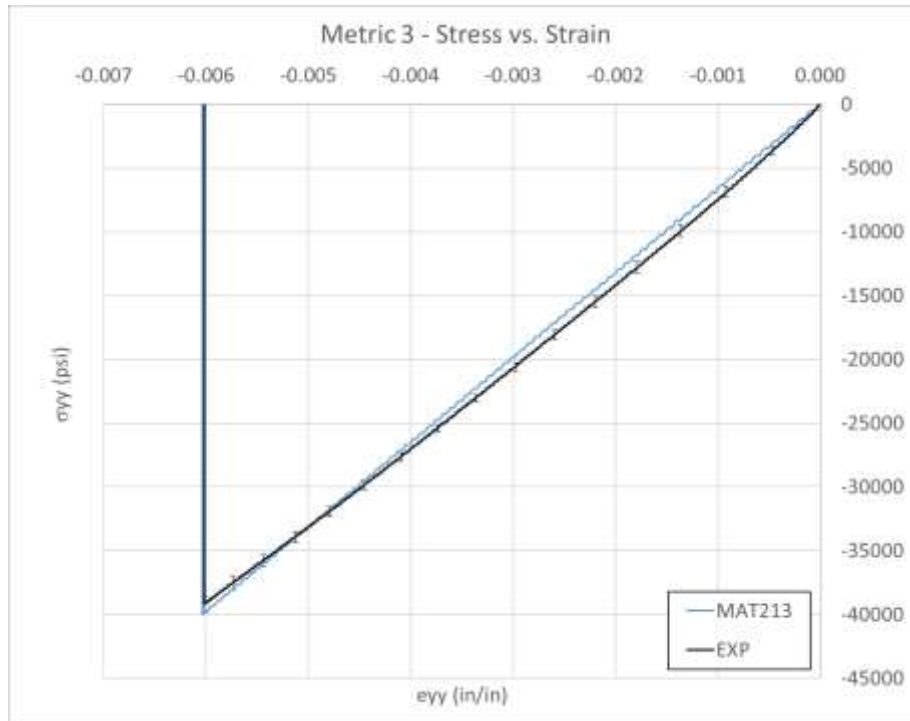
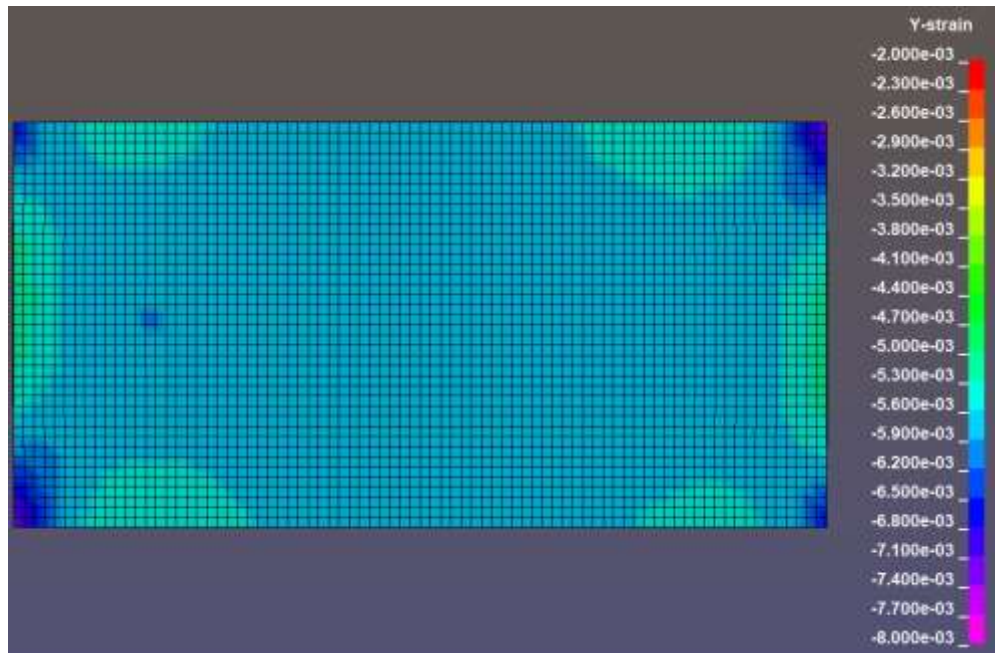
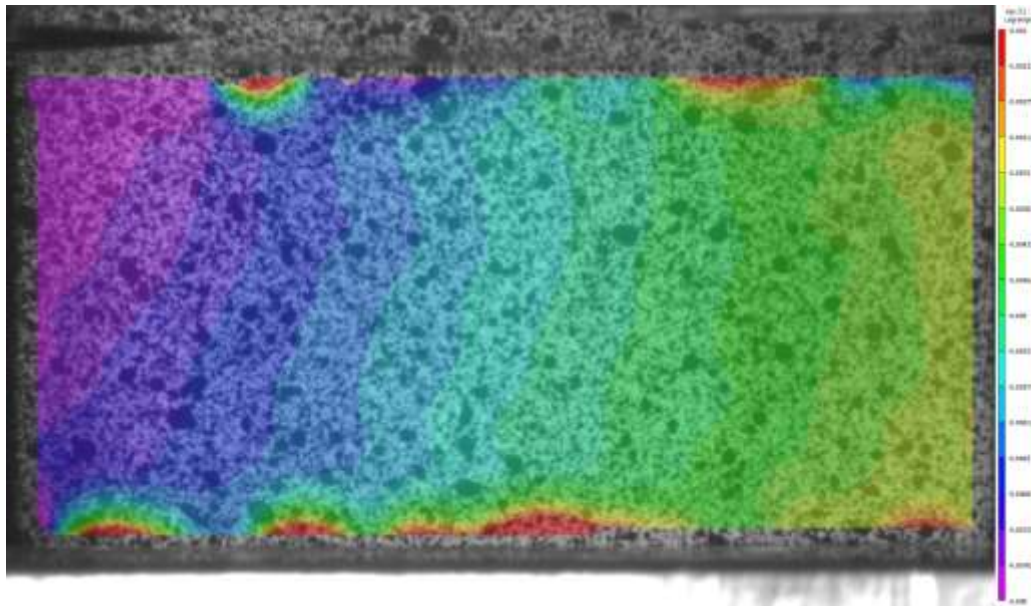


Fig. 6.20. Metric 3 - stress-strain comparison

A fringe plot of the y-strain is pictured in Fig. 6.21. The range and color scheme depicting the strain field is identical for the simulation (a) and the experiment (b). The experimental plot shows a gradation from high magnitude to low strain from the right to left edge. However, the experimental value at the center of the coupon is the same as that in the majority of the section of the simulation.



(a)



(b)

Fig. 6.21. Y-Strain fringe plot of compression test, at $t = 150$ s (a) Simulation (b) Experiment

Observation of the gradation shown in the strain field shows that some factor of the experiments caused an asymmetry in the loading condition. Given the desired loading

condition and experimental geometry, the strain field should be symmetric about the vertical axis. A possible cause of asymmetry in the loading is eccentricity caused by the load frame or by the CLC fixture.

6.4.4 Discussion

Metric 1 indicated that the MAT213 simulation under-predicted the transverse strain by approximately one half of the experimental results, while the longitudinal strain was well predicted, in the range of the experimental results.

Metric 2 indicated that the MAT213 simulation had a similar performance in predicting the transverse and longitudinal displacement as measured in the experimental tests. The transverse displacement is under-predicted by the simulation, nearly by one half, while the longitudinal displacement is within the experimental results.

Metric 3 indicated that the MAT213 simulation well predicted the stiffness shown in the experimental results very well. The stress-strain curve extends beyond that of the experimental curves, but the stiffness is within the range of the experimental results for the duration of the experimental tests.

The error seen in the transverse direction metrics for the compression tests could be related to the asymmetry seen in the strain fields.

6.5 LS-DYNA Simulation of Stacked-ply Tension – Stress Concentration Test

6.5.1 Simulation Modeling

The overall geometry as well as boundary and loading conditions for the experimental setup are shown in Fig. 6.22 and Fig. 6.23.

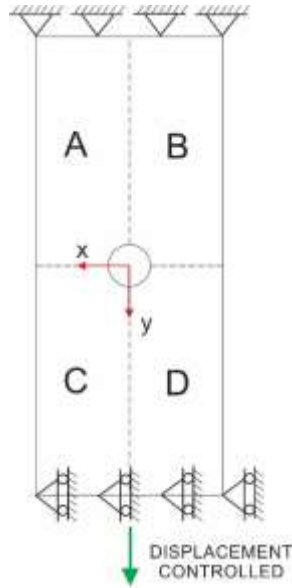


Fig. 6.22. Experimental test conditions, XY plane

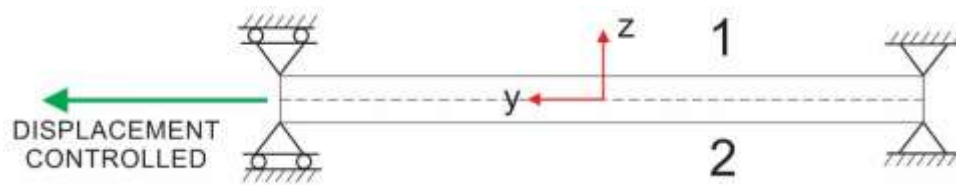


Fig. 6.23. Experimental test conditions, YZ plane

The geometry as well as boundary and loading conditions for the MAT213 simulations are shown in Fig. 6.24 and Fig. 6.25.

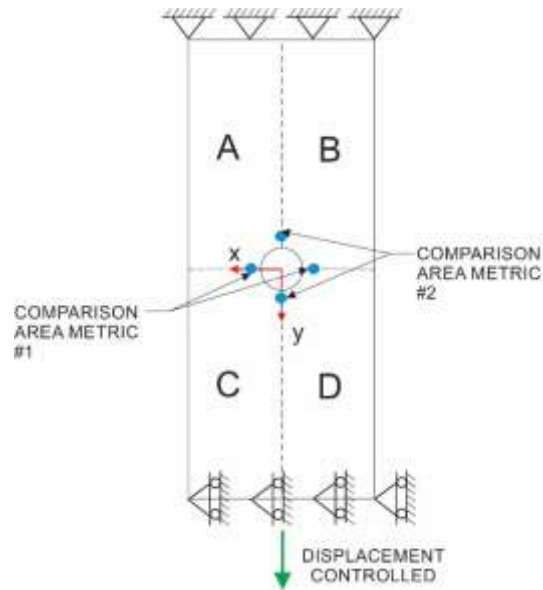


Fig. 6.24. Simulation test conditions, XY plane

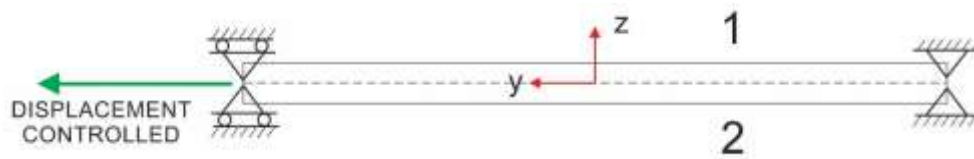
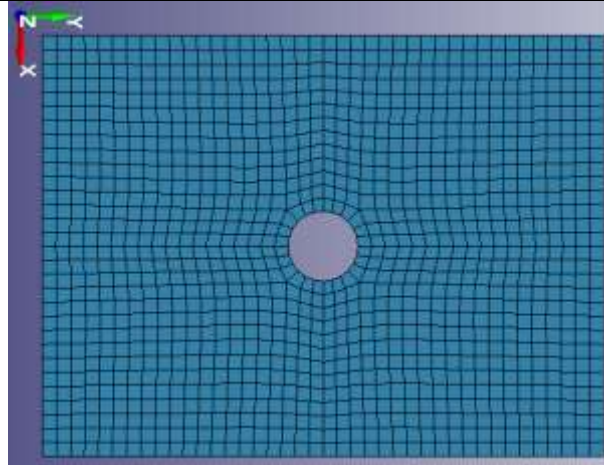
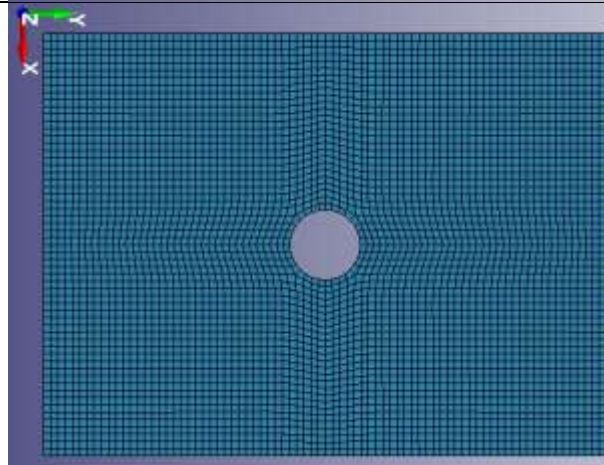


Fig. 6.25. Simulation test conditions, YZ plane

Three Finite Element (FE) models were created with varying element sizes, these are depicted in Table 6.9.

Table 6.9. FE Model Meshes

Mesh	# of MAT213 elements	# of cohesive elements	XY Plane view of FE model
Coarse	2560	2240	

Medium	9504	8316	
Fine	35936	31444	

6.5.2 Validation Metrics

The simulation tests were validated with three distinct metrics comparing the simulation and experimental values. Fig. 6.26-Fig. 6.28 show the coarse, medium, and fine meshes and the nodes and elements used to compare strain and displacement values with the experiments. Only the left half of the simulation models are shown for simplicity, but information was taken from both sides of the model.

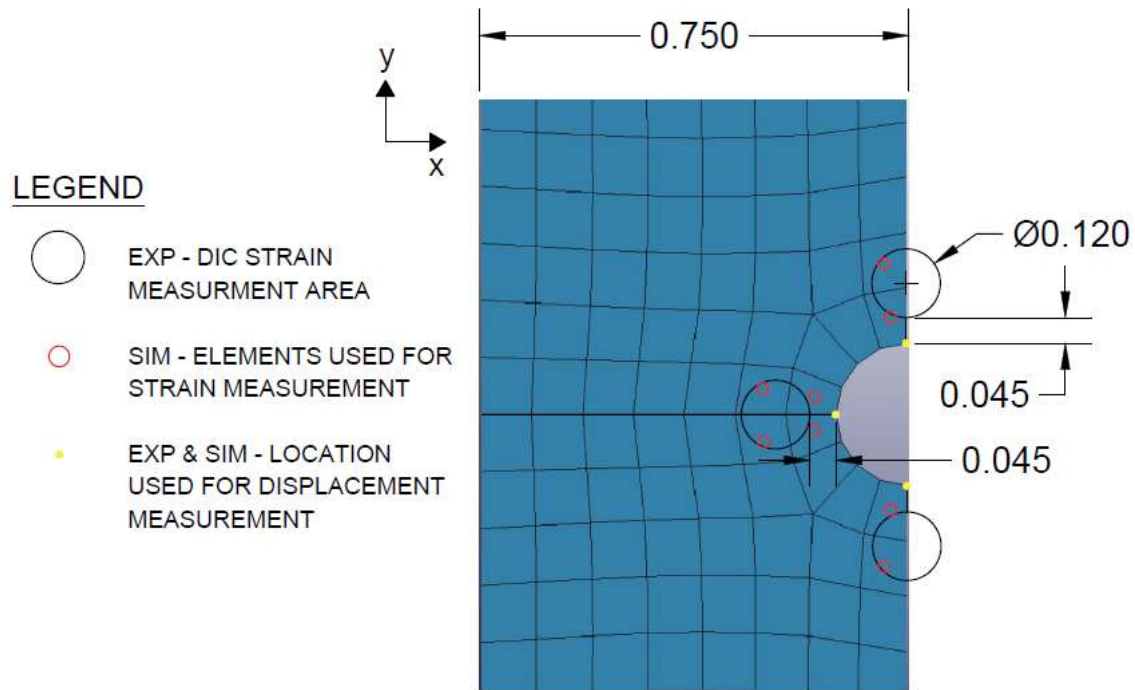


Fig. 6.26. Coarse mesh validation measurement locations

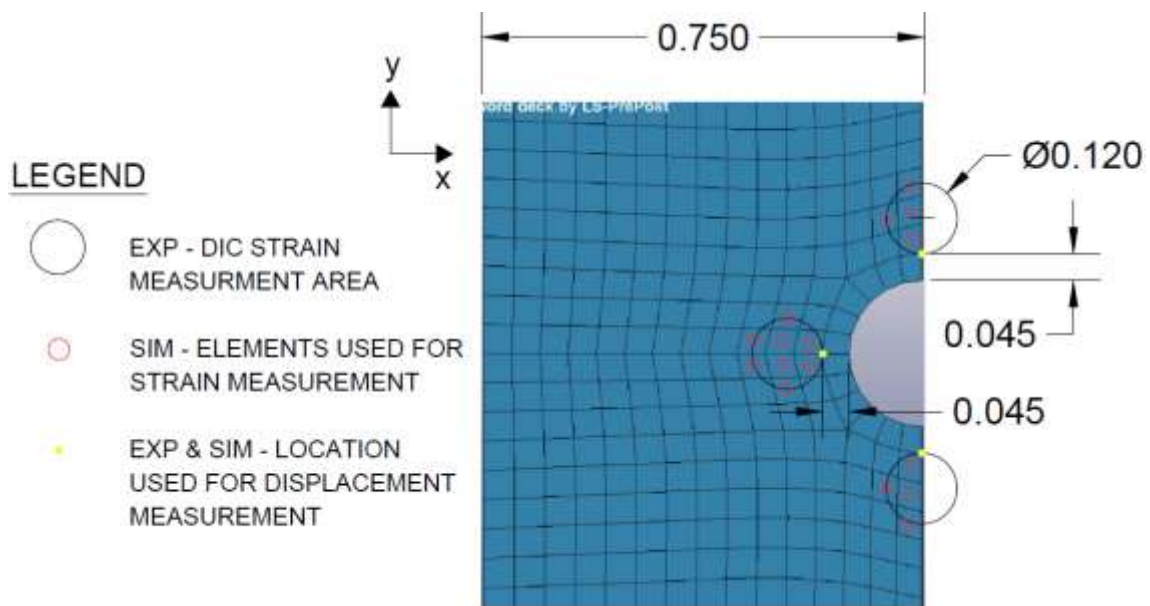


Fig. 6.27. Medium mesh validation measurement locations

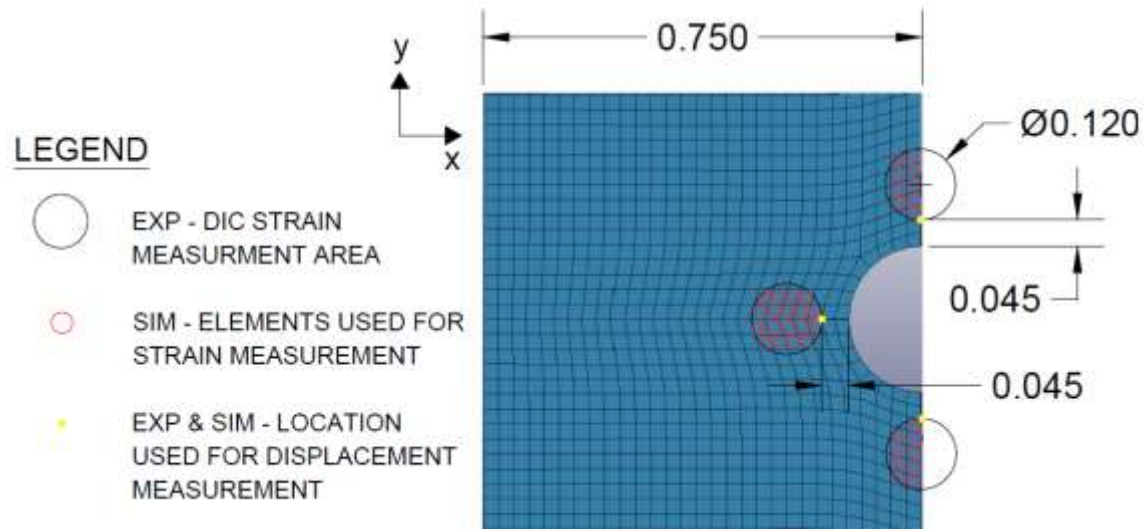


Fig. 6.28. Fine mesh validation measurement locations

Fig. 6.29 shows an example of the measurement areas taken from DIC for the experimental tests.

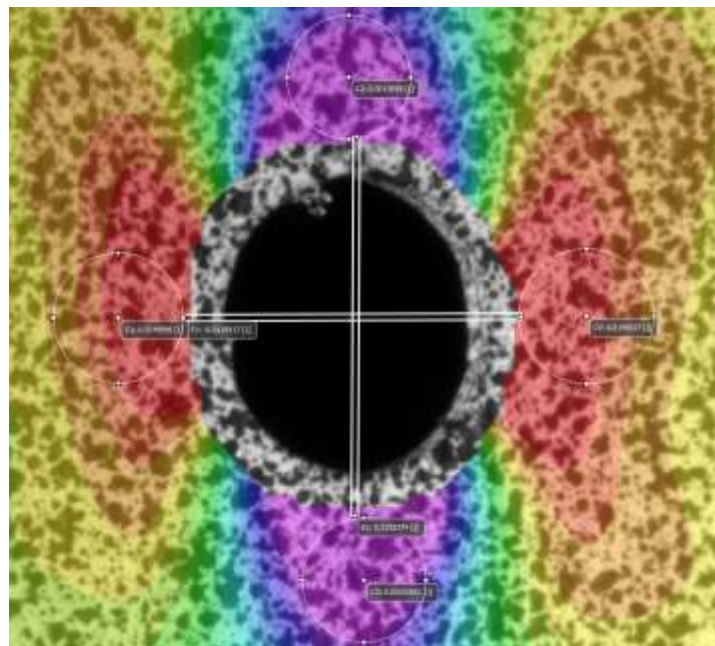


Fig. 6.29. DIC measurement areas

Fig. 6.29 shows four areas in which strain was measured, the four circles adjacent to the hole. The figure also shows two digital extensometers which measured the displacement around the hole, vertically and horizontally.

The three metrics used for comparison are outlined in Table 6.10.

Table 6.10. Validation Metrics Description

Metric	Description
1	Comparison of strains for the 0 ⁰ -ply for the area adjacent to the hole in the x direction, right and left of the hole (shown in Fig. 6.26-Fig. 6.28). The strains ϵ_{xx} , ϵ_{yy} , ϵ_{xy} were plotted against time
2	Comparison of strains for the 0 ⁰ -ply for the area adjacent to the hole in the y direction, both top and bottom (shown in Fig. 6.26-Fig. 6.28). The strains ϵ_{xx} , ϵ_{yy} , ϵ_{xy} were plotted against time
3	Comparison of displacements around the hole in both the x and y directions

Metric 1

A comparison of how the data was captured in the experimental and simulation tests for Metric 1 is shown in Table 6.11.

Table 6.11. Tension Hole Test Metric 1

Data Type	Method of Data Collection
Experimental	Strains were computed using DIC as an area average of a small circular area directly adjacent to the hole in the x direction on both sides. The data from each side was averaged together. These sections are shown in Fig. 6.29.
Simulation	Strains were taken from the elements with red circles next to the hole in the x direction as shown in shown in Fig. 6.26-Fig. 6.28. Strains for each element were averaged together.

Metric 2

A comparison of how the data was captured in the experimental and simulation tests for Metric 2 is shown in Table 6.12.

Table 6.12. Tension Hole Test Metric 2

Data Type	Method of Data Collection
Experimental	Strains were computed using DIC as an area average of a small circular area directly adjacent to the hole in the y direction on both sides. The data from the top and bottom of the hole were compared separately. These sections are shown in Fig. 6.29.

Simulation	Strains were taken from the elements with red circles next to the hole in the y direction on both sides as shown in shown in Fig. 6.26-Fig. 6.28. Strains for each element were averaged together. The elements at the top and bottom of the hole were compared separately
------------	--

Metric 3

A comparison of how the data was captured in the experimental and simulation tests for Metric 3 is shown in Table 6.13.

Table 6.13. Tension Hole Test Metric 3

Data Type	Method of Data Collection
Experimental	Digital extensometers were used to track the relative displacement between the top and bottom of the hole and the left and right of the hole as shown in Fig. 6.29.
Simulation	The x and y displacement was recorded for the nodes corresponding to those shown with yellow dots in shown in Fig. 6.26-Fig. 6.28. For the vertical extension, the relative displacement is recorded as the difference between the two nodes aligned in the y direction. For the horizontal extension, the relative displacement is recorded as the difference between the two nodes aligned in the x direction.

6.5.3 Results

Fig. 6.30-Fig. 6.32 show the results for Metric 1.

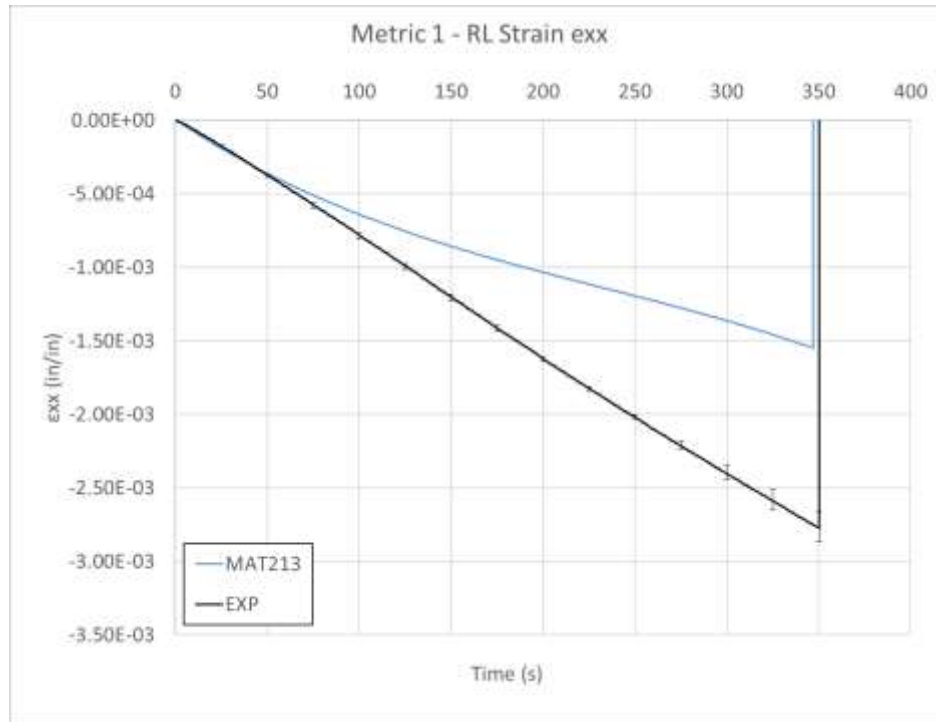


Fig. 6.30. Metric 1 - ϵ_{xx} comparison

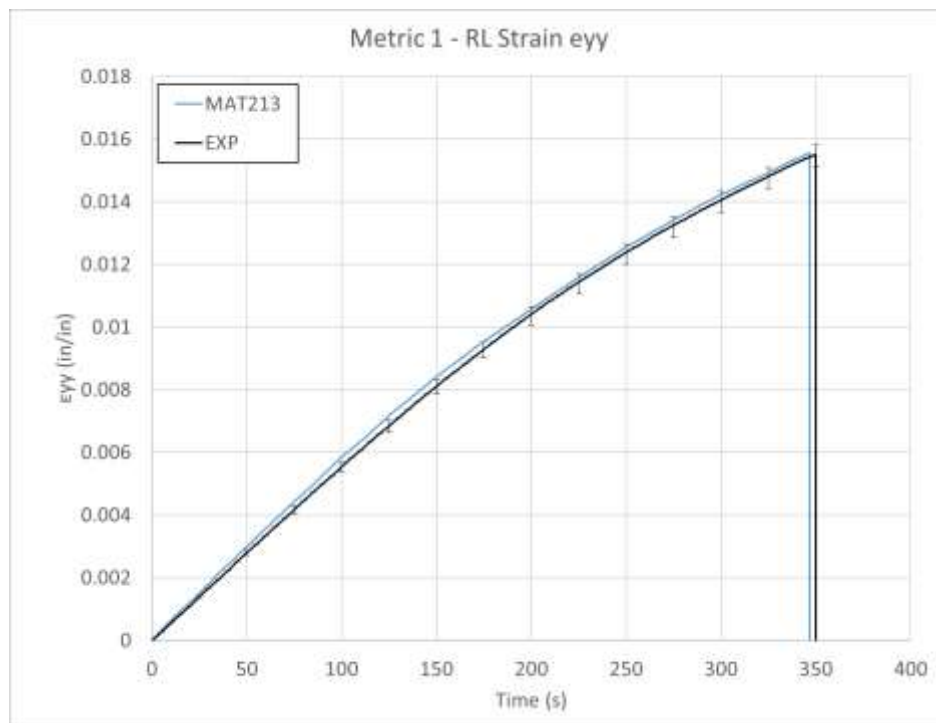


Fig. 6.31. Metric 1 - ϵ_{yy} comparison

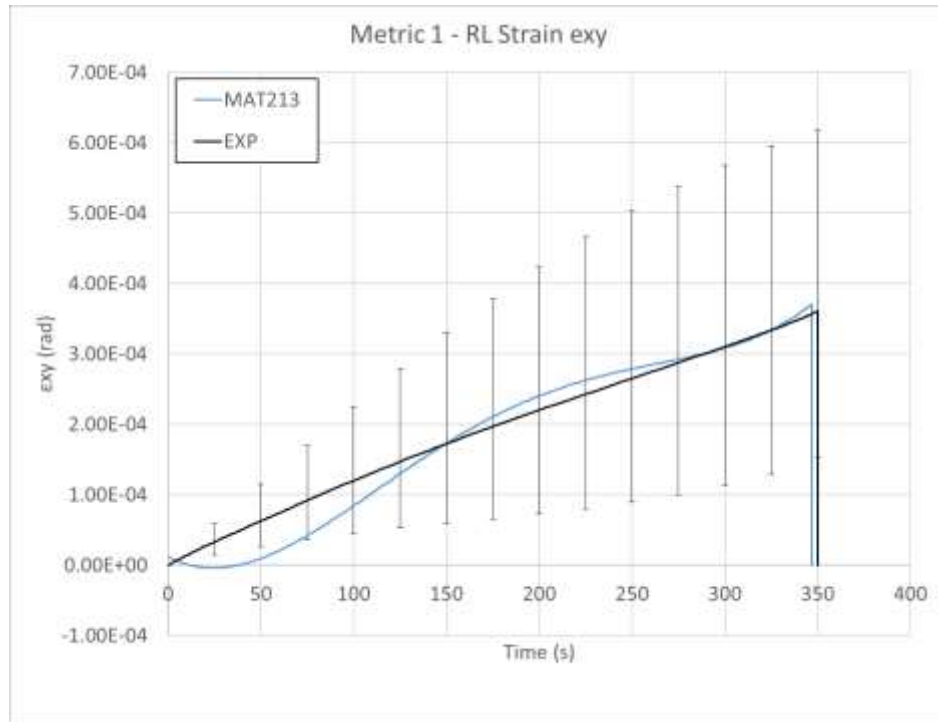


Fig. 6.32. Metric 1 - ϵ_{xy} comparison

Fig. 6.33-Fig. 6.35 show the results for Metric 2 for the area above the hole.

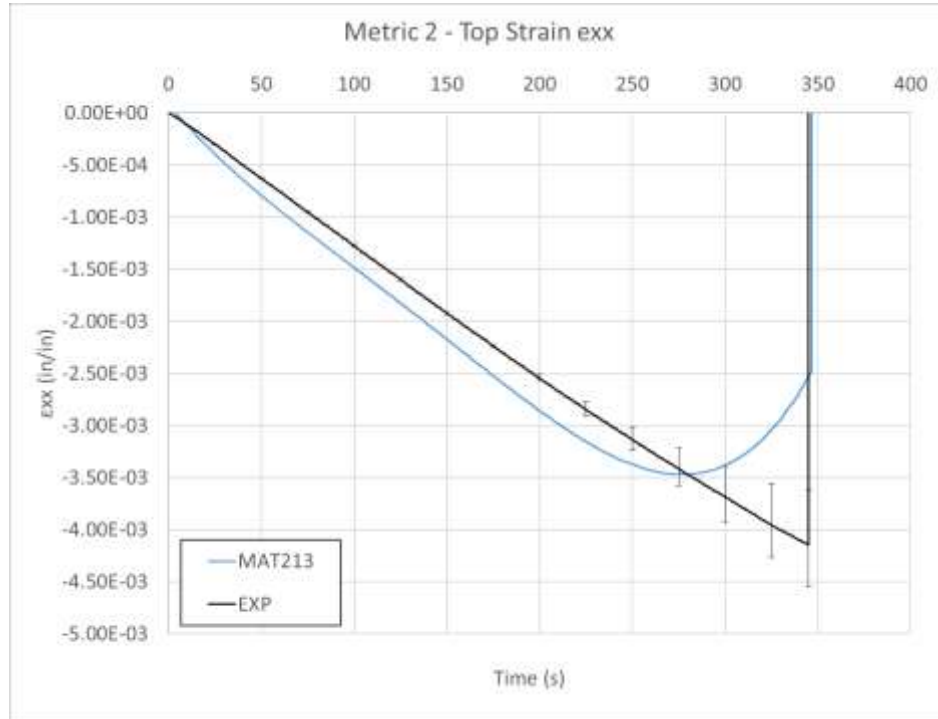


Fig. 6.33. Metric 2 - above hole ϵ_{xx} comparison

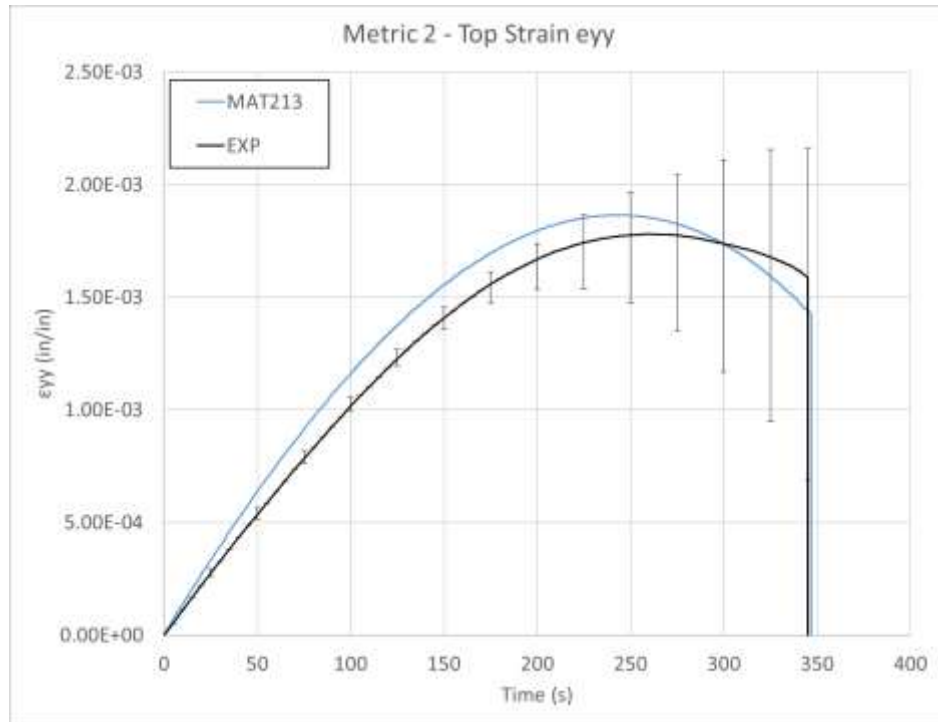


Fig. 6.34. Metric 2 - above hole ϵ_{yy} comparison

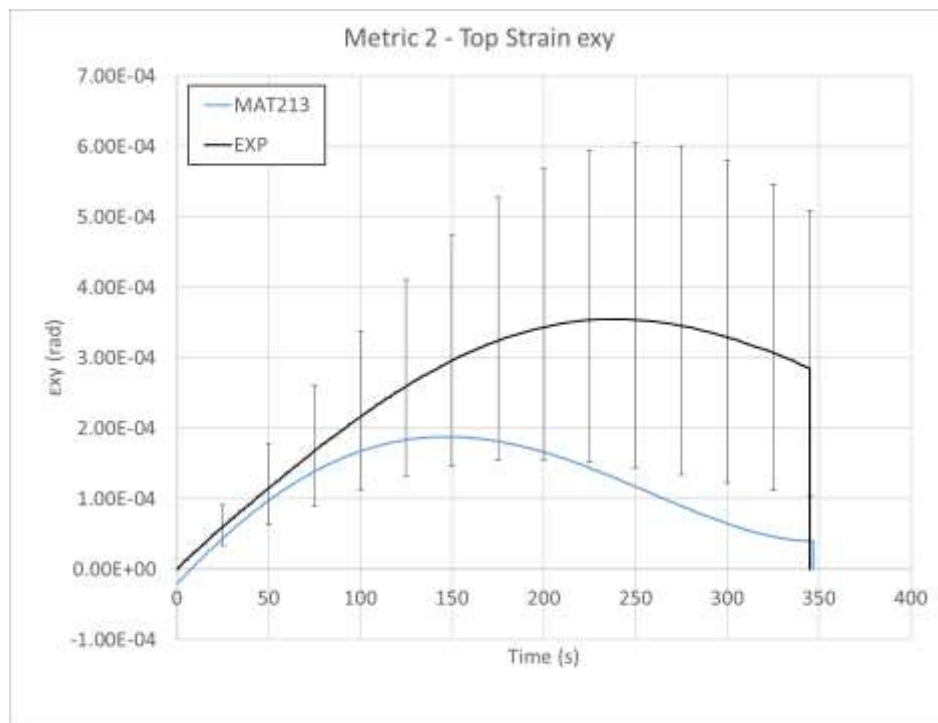


Fig. 6.35. Metric 2 - above hole ϵ_{xy} comparison

Fig. 6.36-Fig. 6.38 show the results for Metric 2 for the area below the hole.

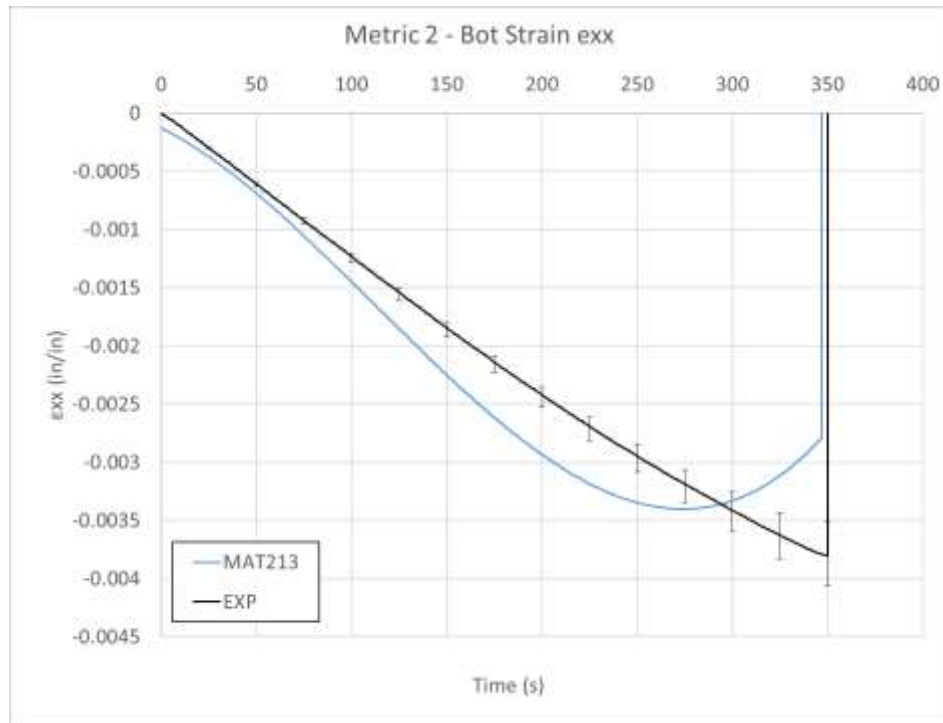


Fig. 6.36. Metric 2 - below hole ϵ_{xx} comparison

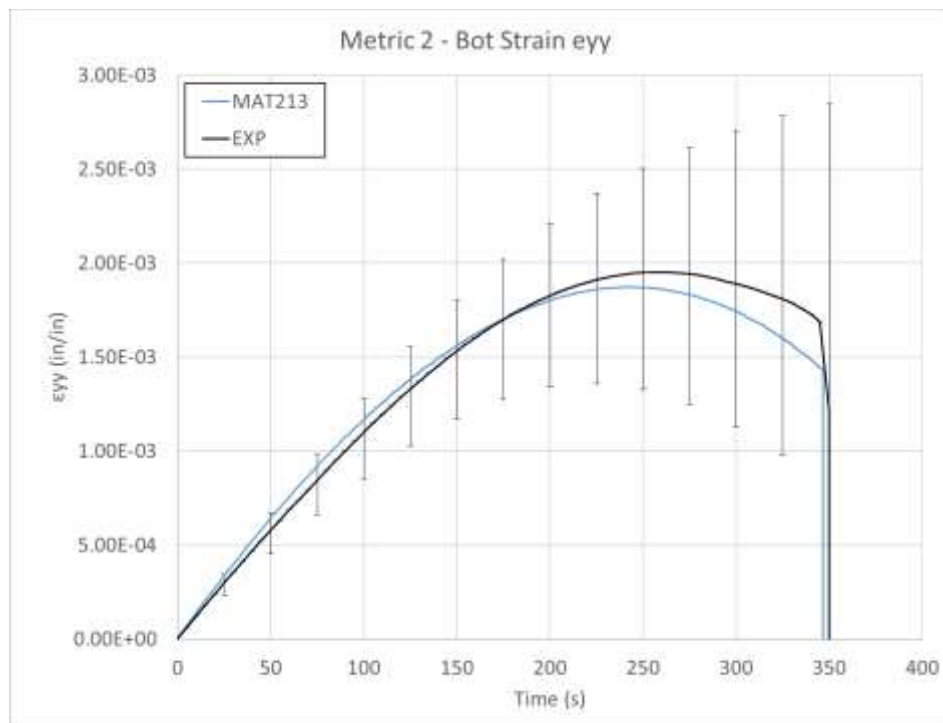


Fig. 6.37. Metric 2 - below hole ϵ_{yy} comparison

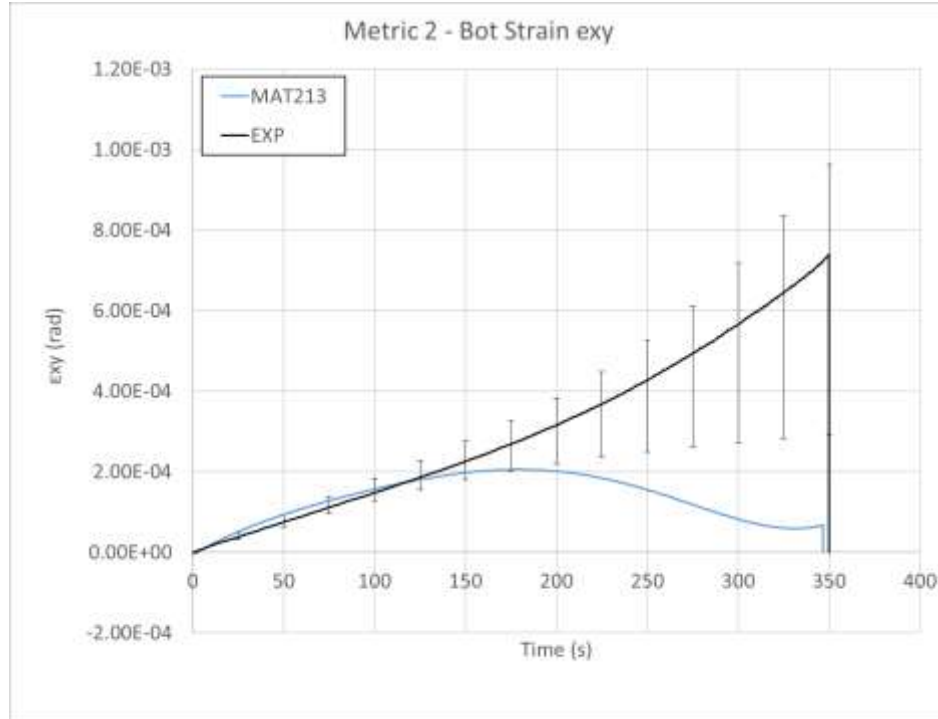


Fig. 6.38. Metric 2 - below hole ϵ_{xy} comparison

Fig. 6.39-Fig. 6.40 show the results for Metric 3.

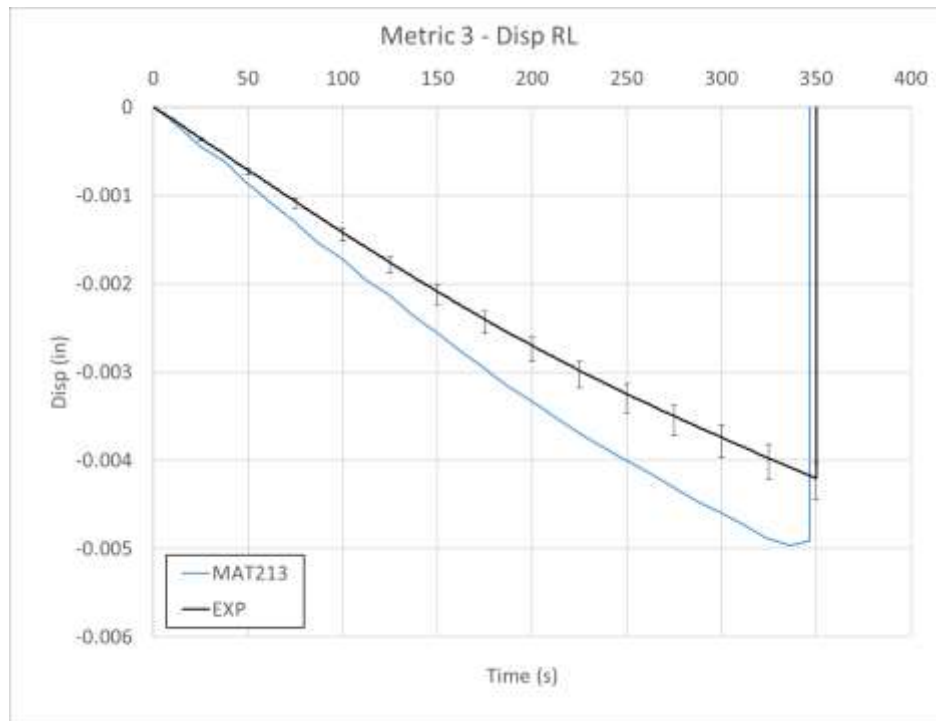


Fig. 6.39. Metric 3 - x-direction displacement

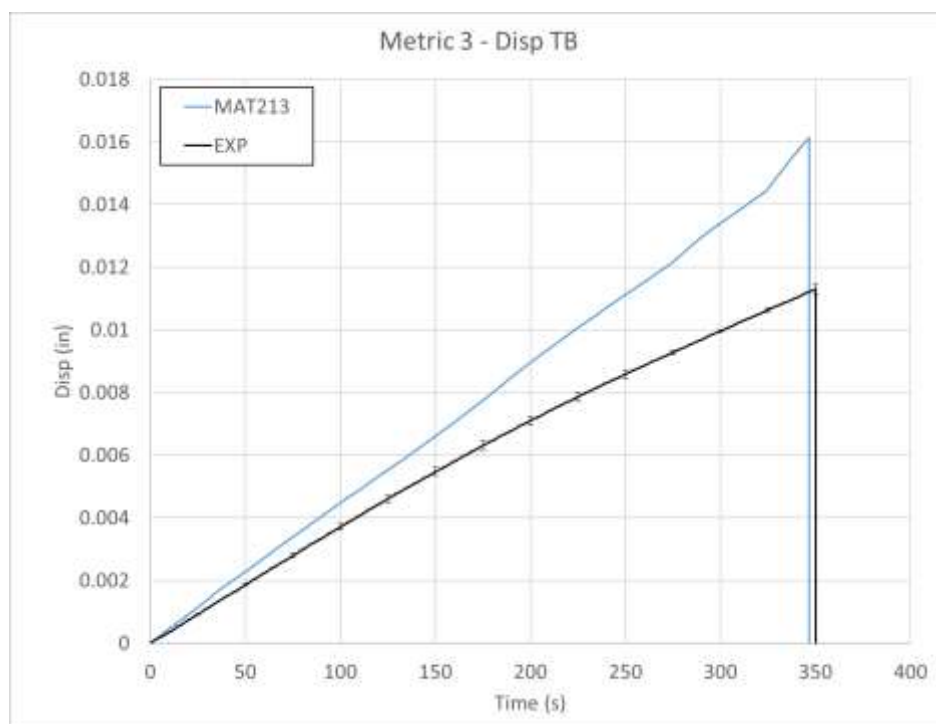
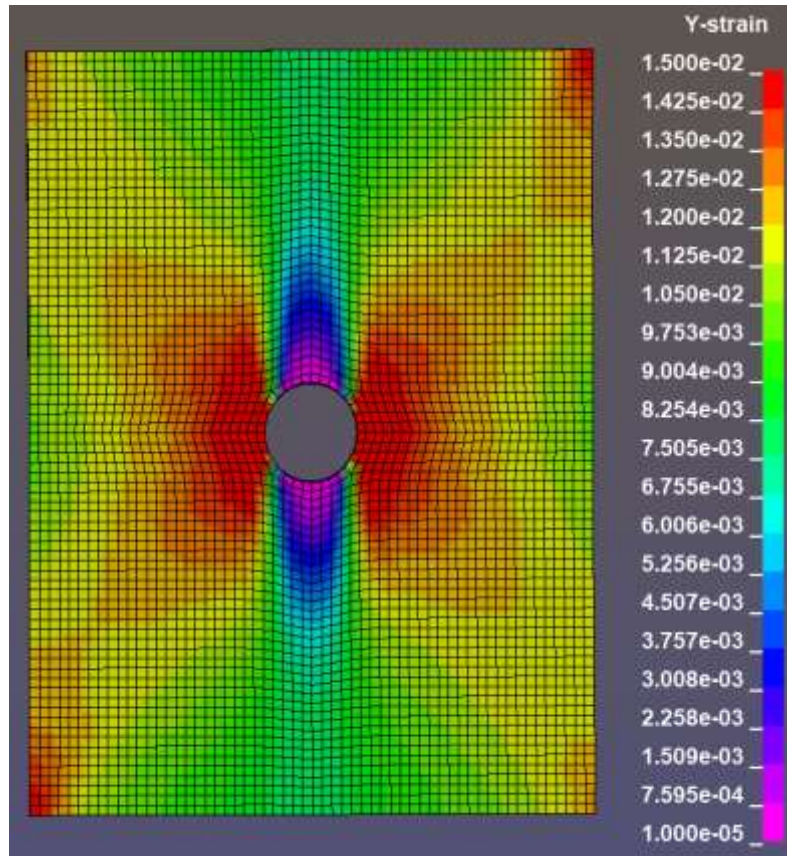
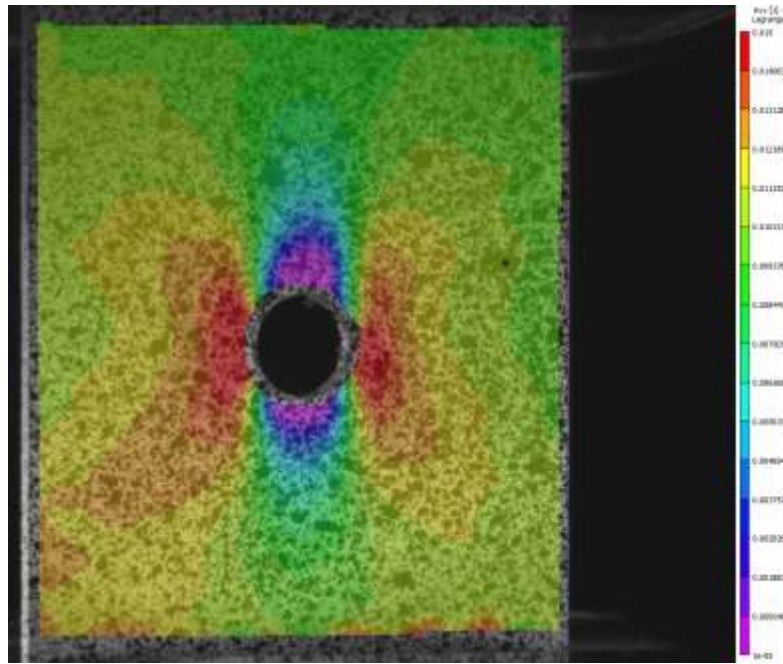


Fig. 6.40. Metric 3 - y-direction displacement

A fringe plot of the y-strain is pictured in Fig. 6.41. The range and color scheme depicting the strain field is identical for the simulation (a) and the experiment (b). The experimental plot shows some asymmetry on the right and left halves of the coupon. However, the magnitudes and shape of the strain concentrations all around the hole match closely between the experimental and simulation plots.



(a)



(b)

Fig. 6.41. Y-Strain fringe plot of tension-hole test, at $t = 325$ s (a) Simulation (b) Experiment

6.5.4 Discussion

Several of the simulation curves used for comparison had data that was fitted using polynomial regression. The details of the polynomial regressions are shown in Table 6.14.

Table 6.14 Polynomial Regression Fitting of Tension with Hole Simulation Metrics

Metric	Order of polynomial regression	R-squared of regression	Fig. #
Metric 1 – RL Strain exx	Cubic	0.9974	Fig. 6.30
Metric 1 – RL Strain eyy	None	n/a	Fig. 6.31
Metric 1 – RL Strain exy	Quartic	0.9959	Fig. 6.32
Metric 2 – Top Strain exx	Quartic	0.9943	Fig. 6.33
Metric 2 – Top Strain eyy	Cubic	0.9928	Fig. 6.34
Metric 2 – Top Strain exy	Quartic	0.7979	Fig. 6.35
Metric 2 – Bot Strain exx	Cubic	0.9940	Fig. 6.36
Metric 2 – Bot Strain eyy	Cubic	0.9947	Fig. 6.37
Metric 2 – Bot Strain exy	Quintic	0.7521	Fig. 6.38
Metric 3 – Disp RL	None	n/a	Fig. 6.39
Metric 3 – Disp TB	None	n/a	Fig. 6.40

Metric 1 indicated that the MAT213 simulation under-predicted the transverse strain to the right and left of the hole by nearly one half. The longitudinal strain at this location was well predicted within the experimental values. The experimental values of the shear strain at this location had a very large range within which was the simulation curve.

Metric 2 showed a close comparison for transverse, longitudinal and shear strain both above and below the hole. The shear strain below the hole visually featured the most deviation between the experimental and simulation curves. The initial shear strain at this location was well predicted by the simulation until a time of approximately 150 seconds, at which time the experimental values increased exponentially, but the simulation values decreased.

Metric 3 indicated that the MAT213 simulation over-predicted the displacement around the hole in both the x and y direction. By the end of the simulation, the x-direction displacement was over-predicted by approximately 25% and the y-displacement was over-predicted by approximately 30%.

The overestimation of the displacements around the hole could be due to errors in the simulated delamination around the hole. In both the experimental and simulation test coupons, delamination was observed around the hole at the end of the test, however the amount of delamination was difficult to compare. The simulation could have delaminated more than the experiment and led to the overestimation of displacement around the hole. This difference could be amended as the cohesive zone parameters continue to be tuned.

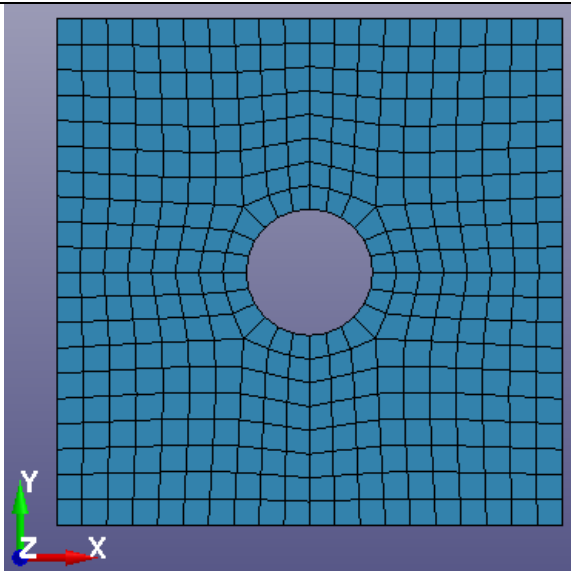
6.6 LS-DYNA Simulation of Stacked-ply Compression – Stress Concentration Test

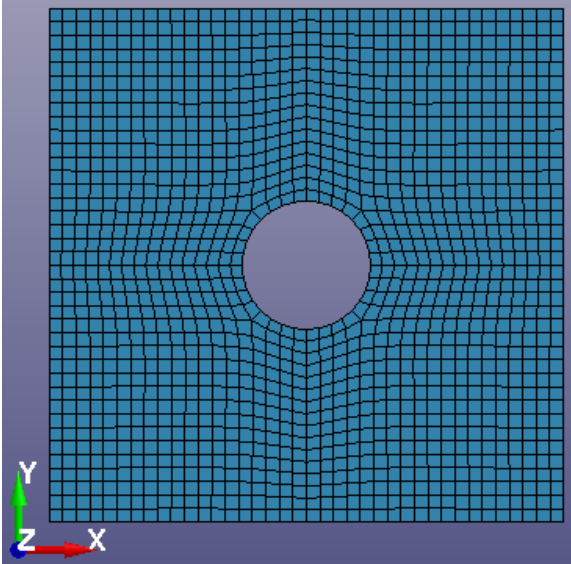
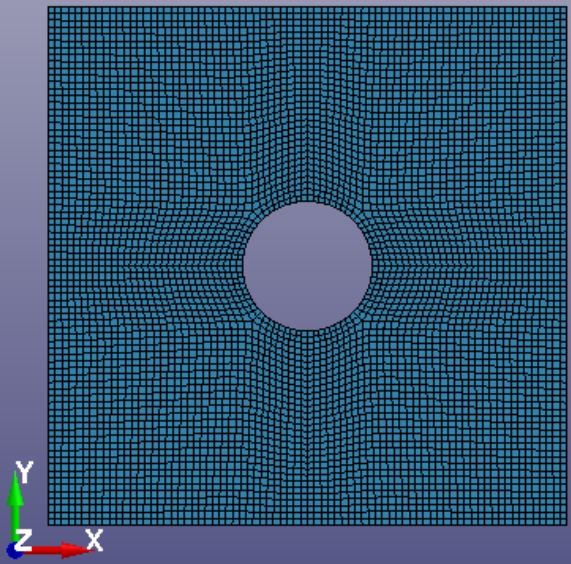
6.6.1 Simulation Modeling

Only the gage area of the experimental test was considered for the simulations. Thus, the experimental and simulation modeling and fixity conditions was the same as for the stacked-ply tension hole tests. The dimensions of gage area were different, but the overall geometry was the same.

Three Finite Element (FE) models were created with varying element sizes, these are depicted in Table 6.15.

Table 6.15. FE Model Meshes

Mesh	# of MAT213 elements	# of cohesive elements	XY Plane view of FE model
Coarse	3104	2716	

Medium	11296	9884	
Fine	44768	39172	

6.6.2 Validation Metrics

The simulation tests were validated with three distinct metrics comparing the simulation and experimental values. Fig. 6.42-Fig. 6.44 show the coarse, medium, and fine meshes and the nodes and elements used to compare strain and displacement values with the experiments. Only the left half of the simulation models are shown for simplicity, but information was taken from both sides of the model. These figures are

similar to those for the tension with hole tests, except the dimensions of the strain gage sections are slightly smaller. This was due to the smaller overall gage section of the compression with hole tests.

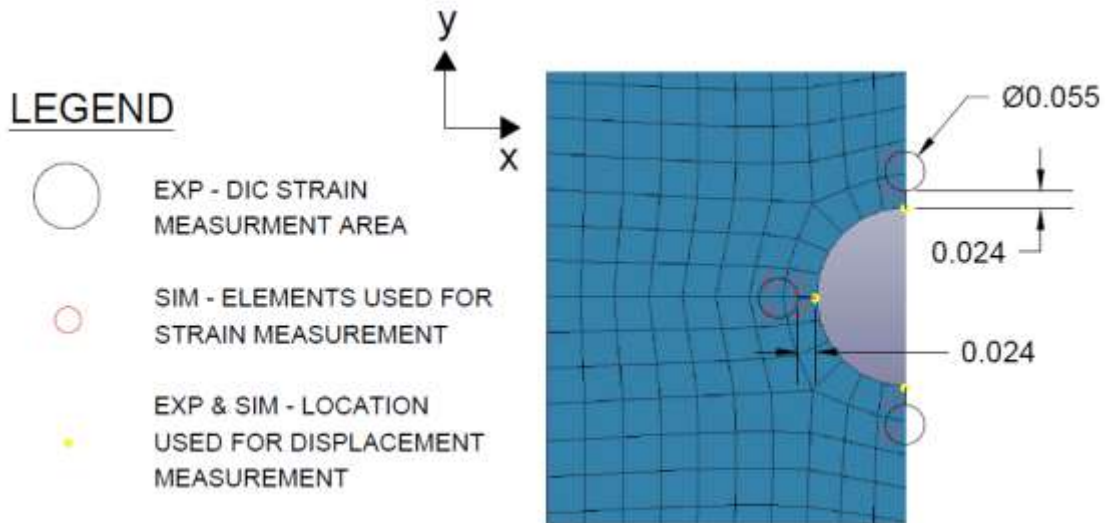


Fig. 6.42. Coarse mesh validation measurement locations

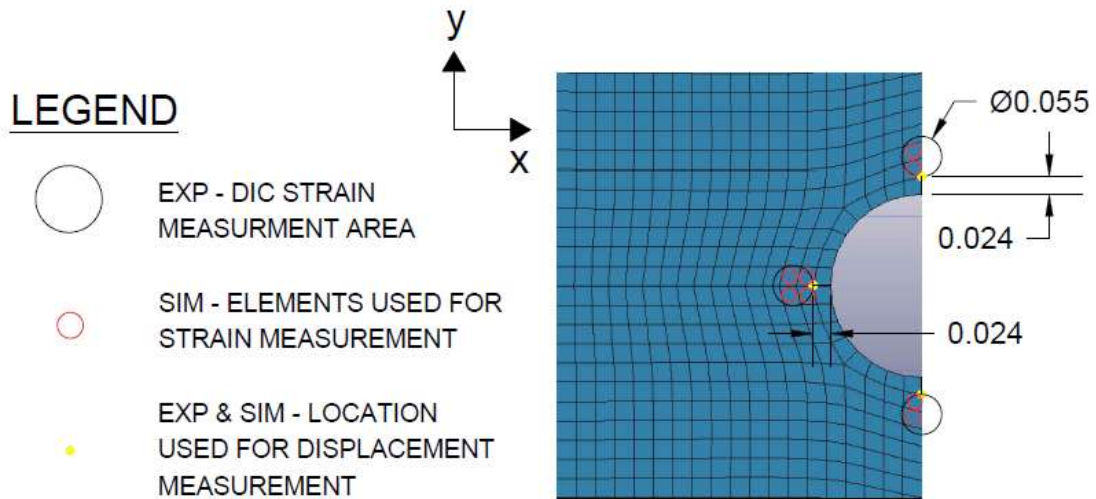


Fig. 6.43. Medium mesh validation measurement locations

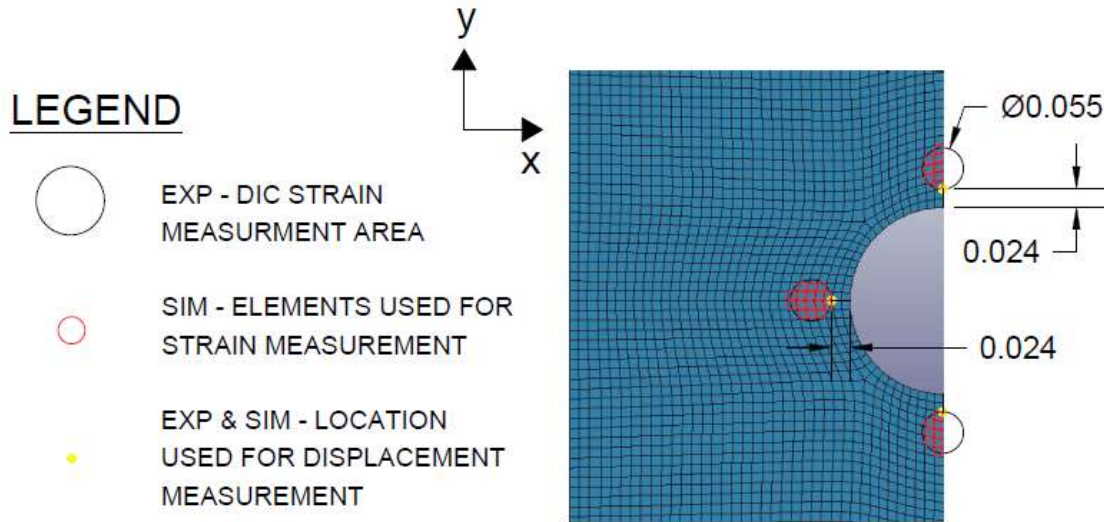


Fig. 6.44. Fine mesh validation measurement locations

The validation metrics and data collection methods were the same as for the stacked-ply tension with hole tests.

6.6.3 Results

MAT213 specifications that were used for the results shown in Fig. 6.45-Fig. 6.55 are detailed in Table 6.16.

Table 6.16. MAT213 Specifications

Parameter	Specification
Damage Model	Incorporated, only uncoupled 2-direction compression and uncoupled 12-plane shear are included
Failure Model	Not incorporated

Fig. 6.45-Fig. 6.47 show the results for Metric 1.

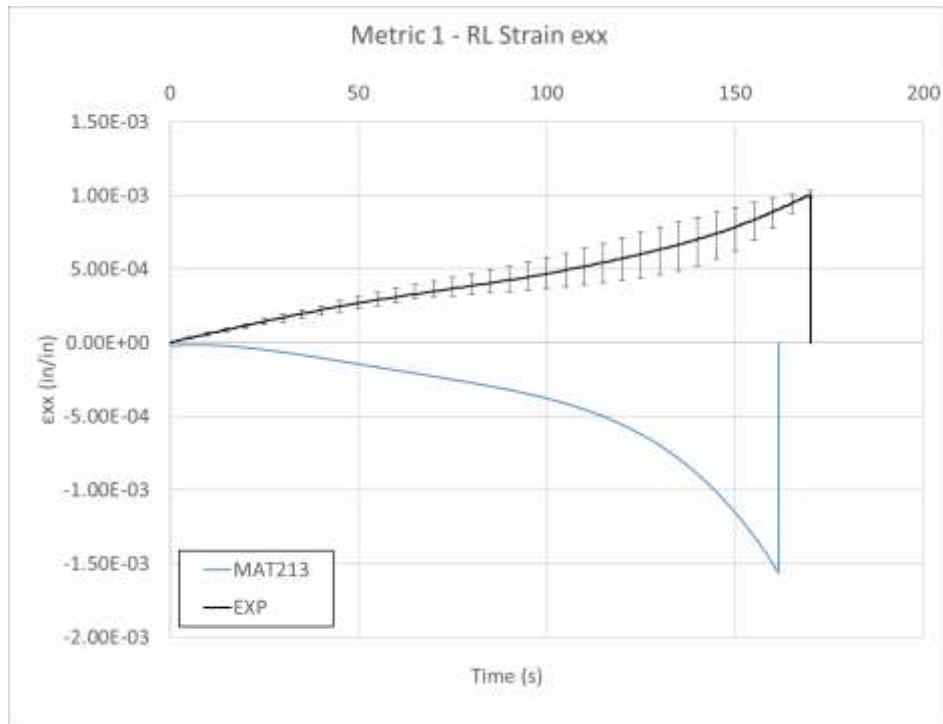


Fig. 6.45. Metric 1 - ϵ_{xx} comparison

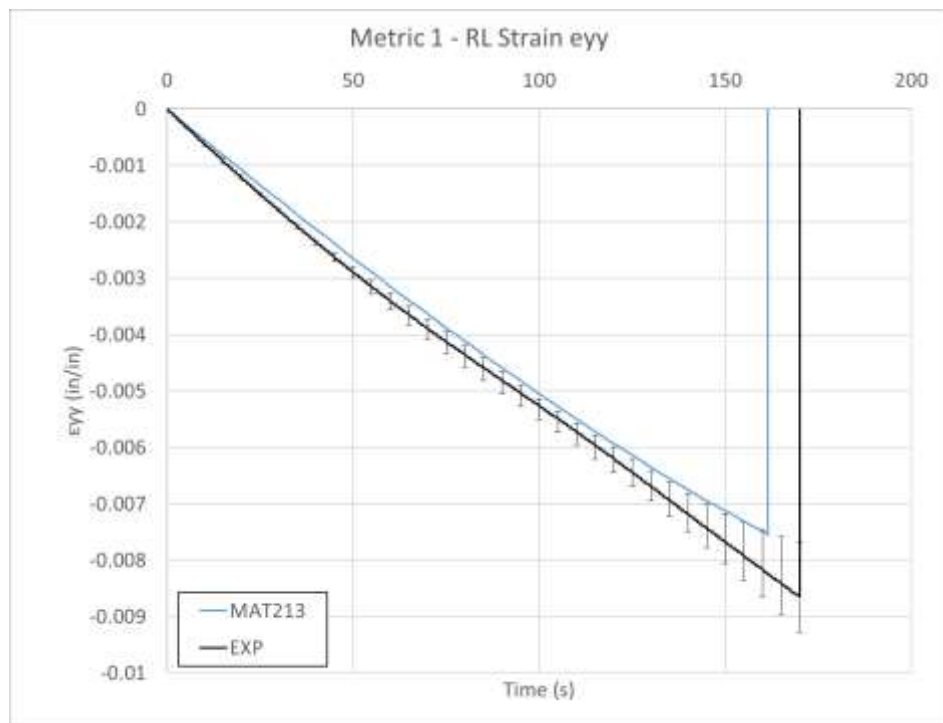


Fig. 6.46. Metric 1 - ϵ_{yy} comparison

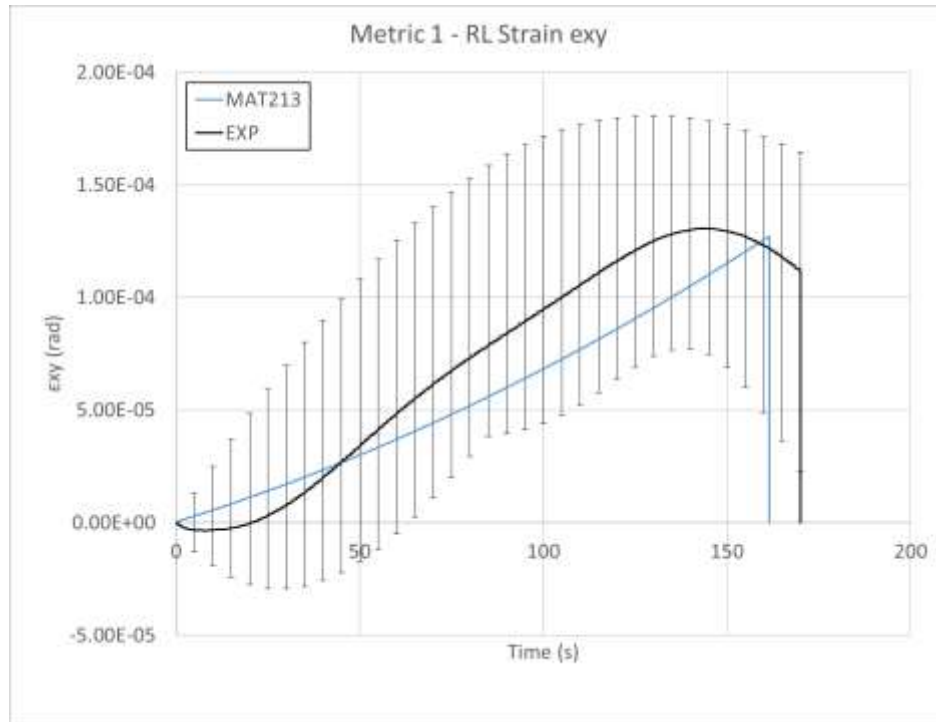


Fig. 6.47. Metric 1 - ϵ_{xy} comparison

Fig. 6.48-Fig. 6.50 show the results for Metric 2 for the area above the hole.

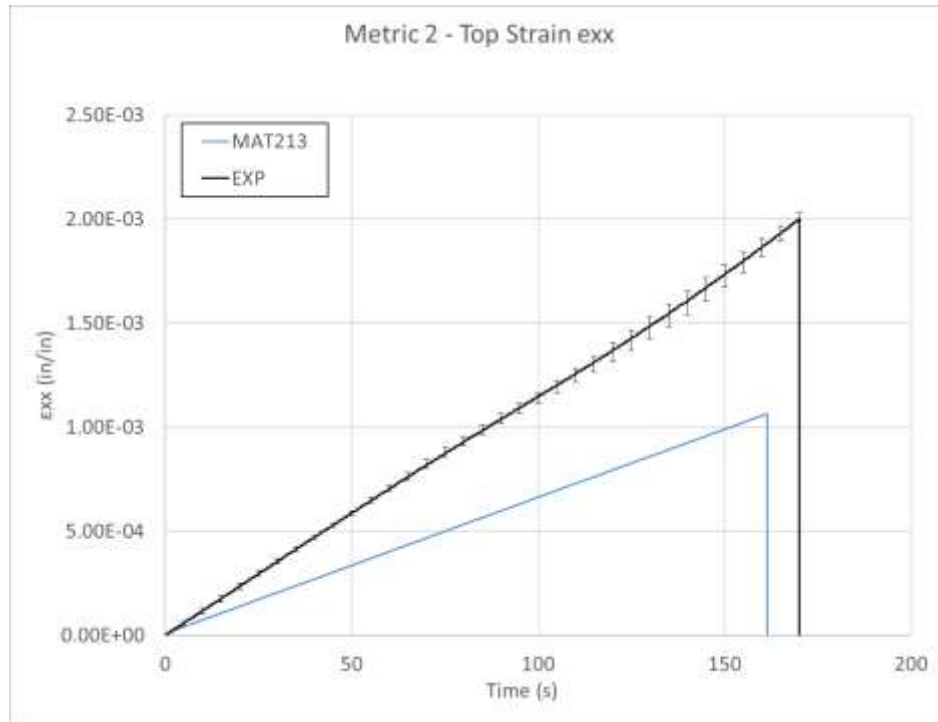


Fig. 6.48. Metric 2 - above hole ϵ_{xx} comparison

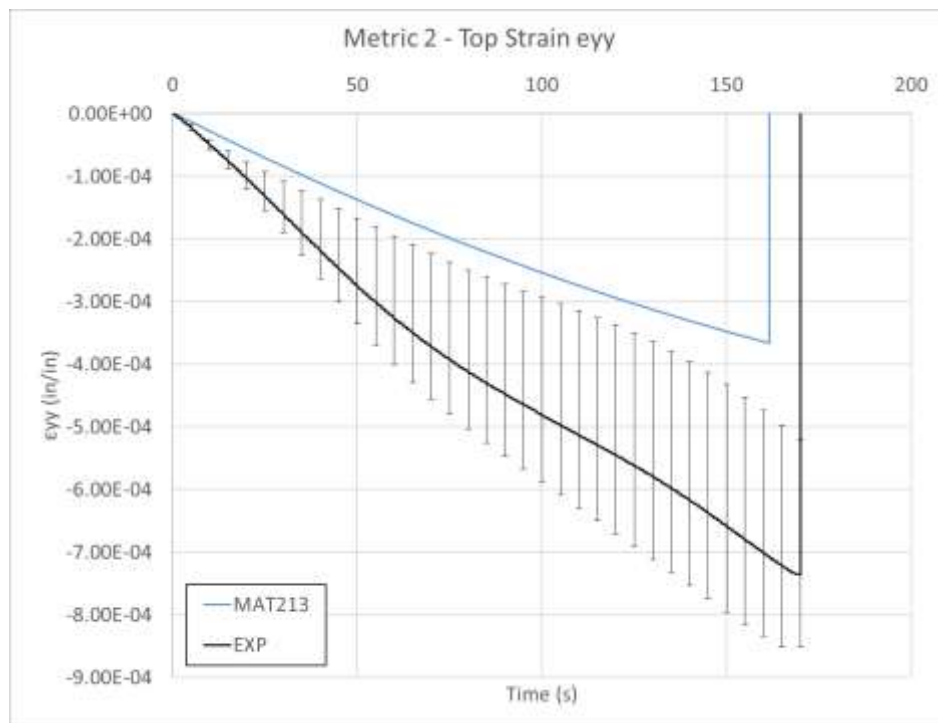


Fig. 6.49. Metric 2 - above hole ϵ_{yy} comparison

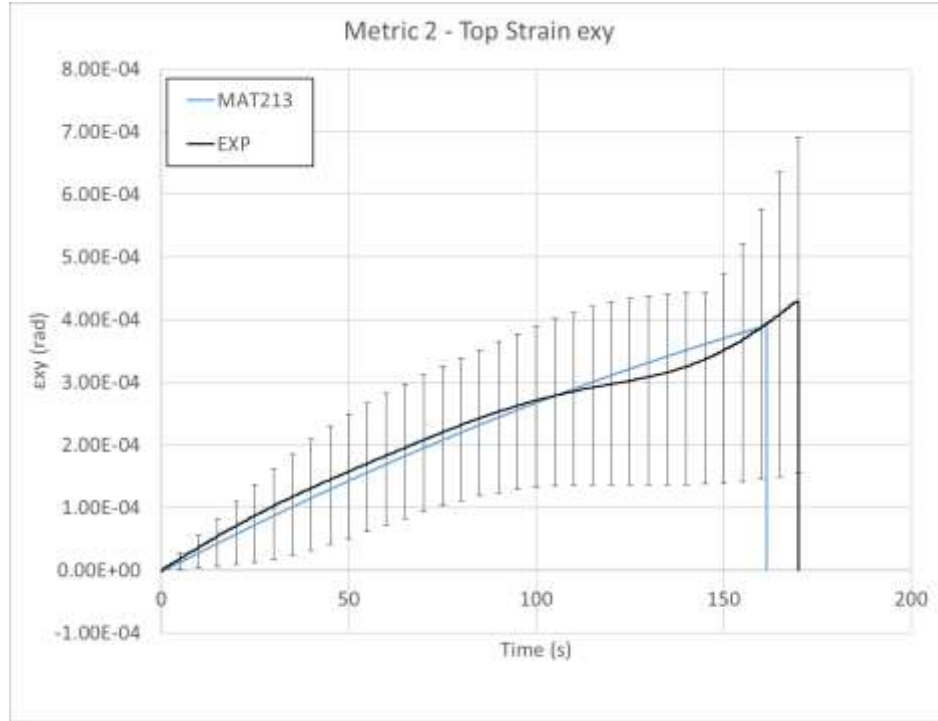


Fig. 6.50. Metric 2 - above hole ϵ_{xy} comparison

Fig. 6.51-Fig. 6.53 show the results for Metric 2 for the area below the hole.

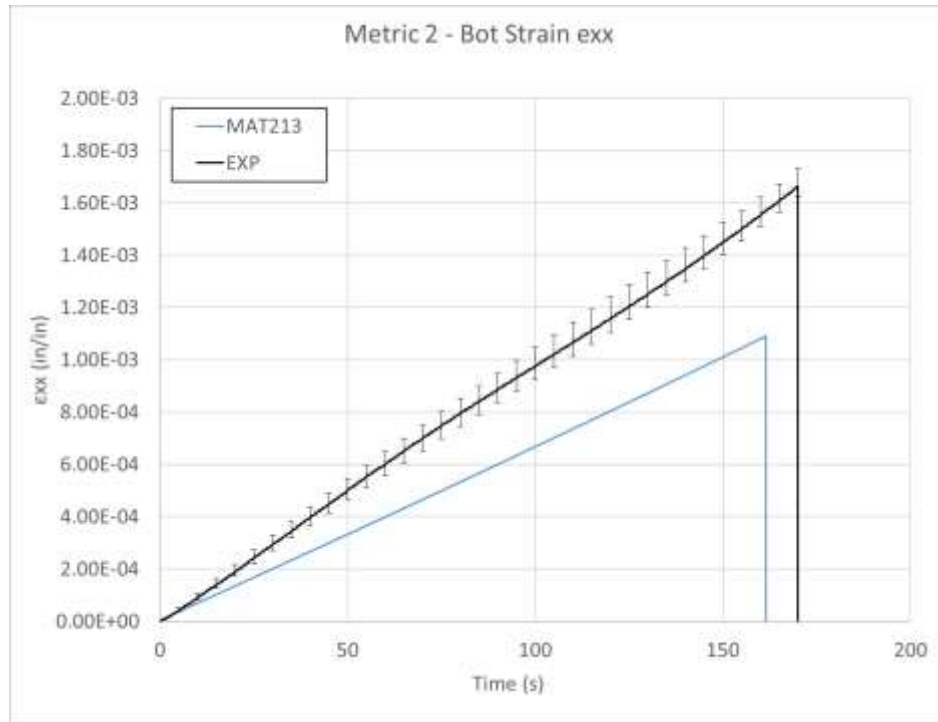


Fig. 6.51. Metric 2 - below hole ϵ_{xx} comparison

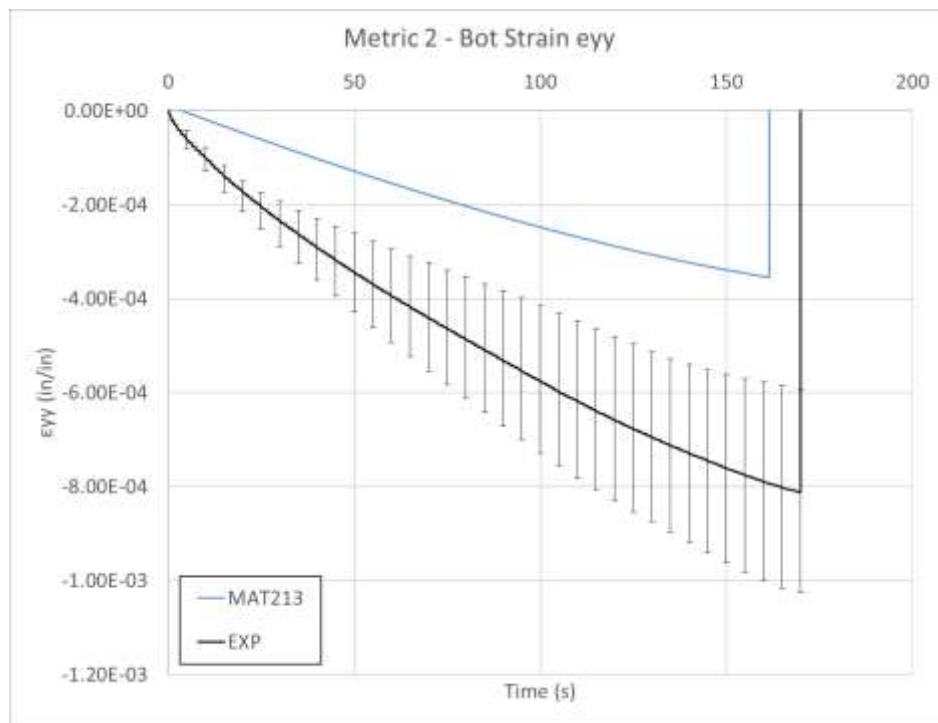


Fig. 6.52. Metric 2 - below hole ϵ_{yy} comparison

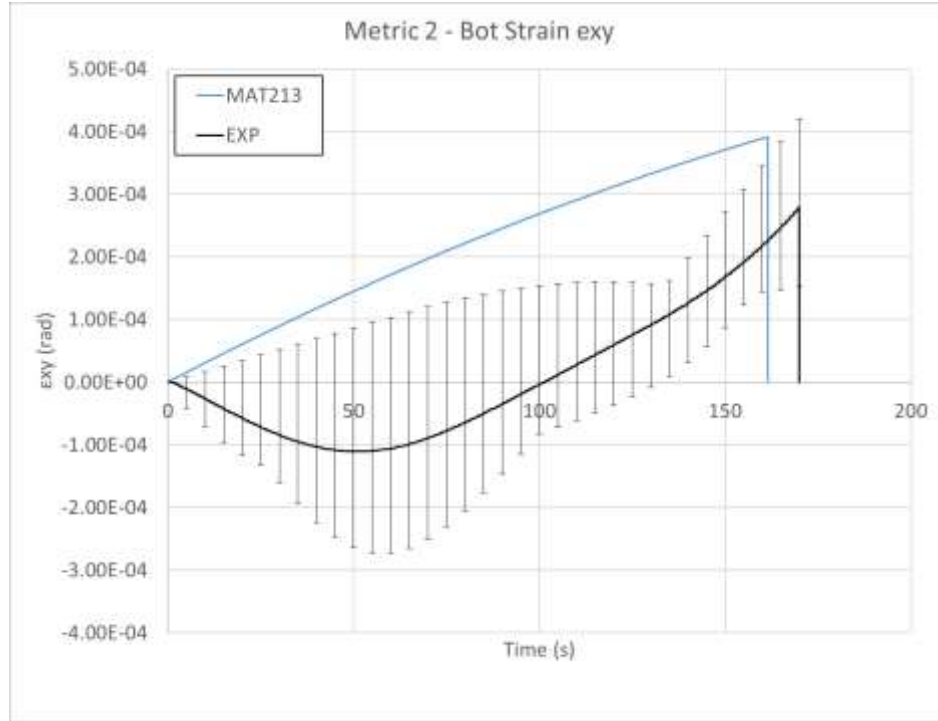


Fig. 6.53. Metric 2 - below hole ϵ_{xy} comparison

Fig. 6.54-Fig. 6.55 show the results for Metric 3.

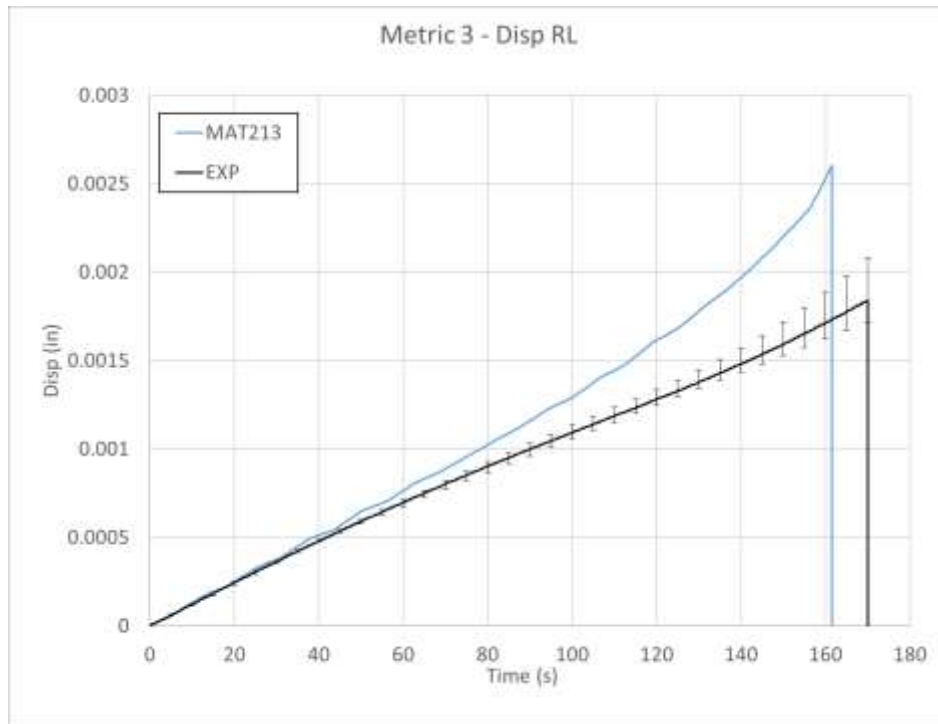


Fig. 6.54. Metric 3 - x-direction displacement

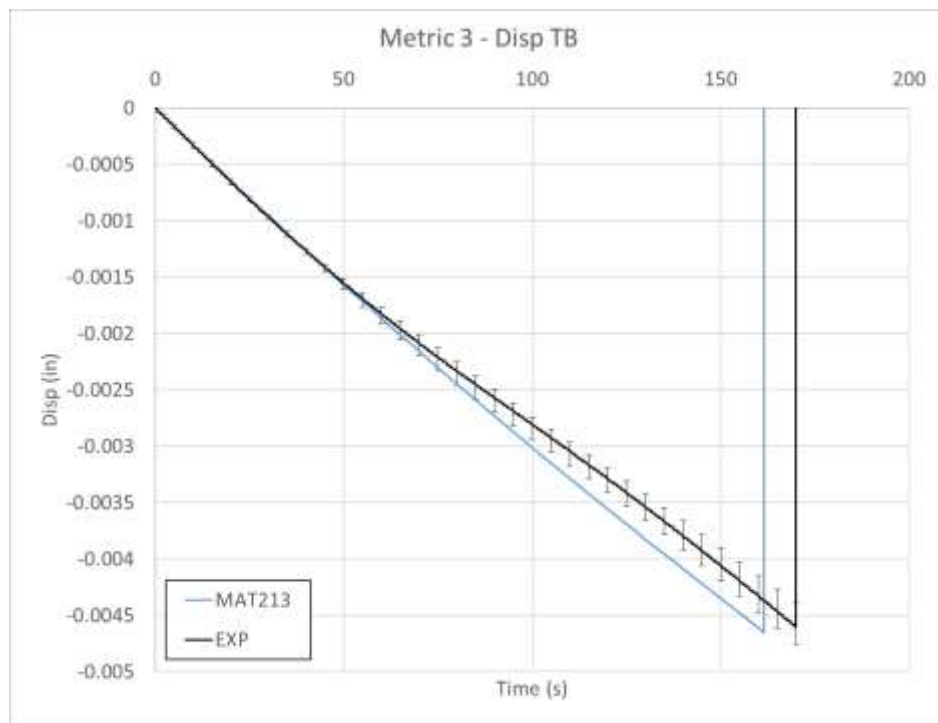
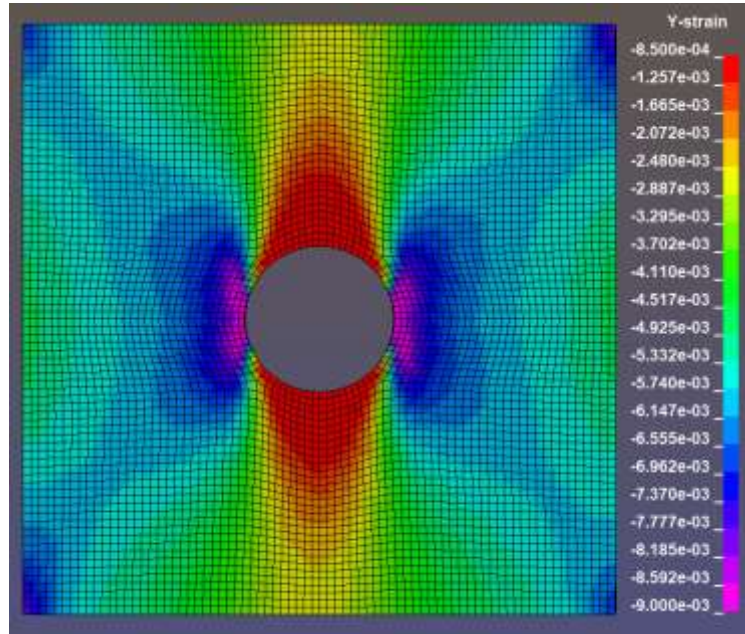
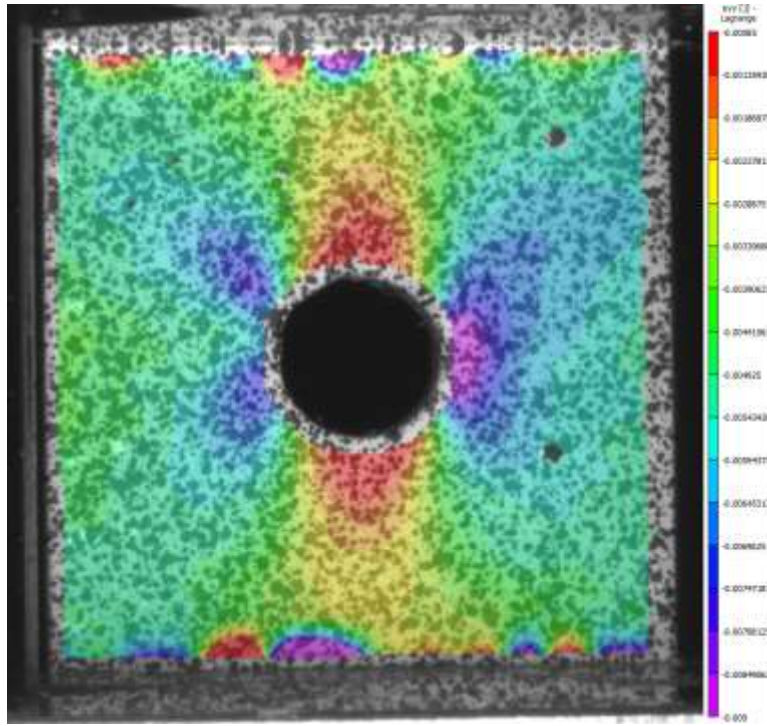


Fig. 6.55. Metric 3 - y-direction displacement

A fringe plot of the y-strain is pictured in Fig. 6.56. The range and color scheme depicting the strain field is identical for the simulation (a) and the experiment (b). The experimental plot shows asymmetry between the right and left side, with less strain concentration directly to the left of the hole. The stress concentrations around the rest of the hole match well between the experiment and simulation.



(a)



(b)

Fig. 6.56. Y-Strain fringe plot of compression-hole test, at $t = 155$ s (a) Simulation (b) Experiment

6.6.4 Discussion

Several of the simulation curves used for comparison had data that was fitted using polynomial regression. The details of the polynomial regressions are shown in Table 6.17.

Table 6.17 Polynomial Regression Fitting of Compression with Hole Simulation Metrics

Metric	Order of polynomial regression	R-squared of regression	Fig. #
Metric 1 – RL Strain exx	Quartic	0.9958	Fig. 6.45
Metric 1 – RL Strain eyy	None	n/a	Fig. 6.46
Metric 1 – RL Strain exy	Quadratic	0.9863	Fig. 6.47
Metric 2 – Top Strain exx	Quadratic	0.9958	Fig. 6.48
Metric 2 – Top Strain eyy	Quadratic	0.9980	Fig. 6.49
Metric 2 – Top Strain exy	Quadratic	0.9995	Fig. 6.50
Metric 2 – Bot Strain exx	Quadratic	0.9928	Fig. 6.51
Metric 2 – Bot Strain eyy	Cubic	0.9982	Fig. 6.52
Metric 2 – Bot Strain exy	Quadratic	0.9995	Fig. 6.53
Metric 3 – Disp RL	None	n/a	Fig. 6.54
Metric 3 – Disp TB	None	n/a	Fig. 6.55

Metric 1 indicated that the MAT213 simulation predicted the longitudinal and shear strain to the right and left of the hole within the experimental values. The transverse strain predicted by MAT213 had a similar magnitude to the experimental values, but the simulation values were negative while the experimental values were positive.

Metric 2 indicated that the MAT213 simulation under-predicted the transverse and longitudinal strain above and below the hole by a factor of approximately one half compared to the experimental values. The shear strain was predicted by MAT213 within the experimental values.

Metric 3 indicated that the MAT213 simulation very closely predicted the y-direction displacement while it over-predicted the x-direction displacement compared to the experimental values. The x-direction displacement simulated values were within the experimental values for approximately a third of the duration of the test, at which time it began to over-predict the displacement in that direction.

The overestimation of the displacements around the hole in the x-direction could be due to errors in the simulated delamination around the hole. This result was similar to that of the stacked-ply tension with hole test. The differences between the simulation and experimental result could be amended as the cohesive zone parameters are tuned.

7. SEM Imaging for MAT213 Model Validation

7.1 Objective

The purposes of the examination of untested, damaged, and failed specimens of the T800/F3900 composite included to observe and understand the underlying structure of the composite. Another purpose was to observe the behavior of the composite at the micro level once it has been loaded, including loading levels cause failure at the coupon level. To fulfill these objectives, tested coupons were obtained from the QS-RT tests detailed in the experimental report produced by Khaled et al. [35]. These previously tested coupons were engaged in a process of cutting, grinding, polishing and imaging to determine the damage and failure patterns at the micro-level.

Four samples were put through this procedure to obtain SEM images. The samples used in this procedure are presented in Table 7.1.

Table 7.1. SEM Image Samples

Sample Name	Original Test Name	Original Test Type
Virgin	-	-
Damaged	TFC2T2C-7	2 direction, tension and compression coupled damage
Failed	TFC2-13	Compression – 2 direction
Failed - Shear	TFS12-8	Shear – 12 plane

The objective of the study was to determine if there was damage at the micro-level that would result in the coupon-level damage or failure that was demonstrated in the original experimental procedure.

Types of micro-level damage that were searched for and discovered include: fiber damage, fiber-matrix debonding, fiber interface damage, matrix damage, and interlayer delamination.

7.2 Procedure

All samples were preserved under room temperature conditions from experimental test date until procured for the imaging procedure.

Cutting

SEM chamber sizes restricted the allowable sample size and required the specimens first be cut into smaller pieces. Specimens were cut with a Dynacut¹¹ high speed saw manufactured by National Scientific Company. The blade used for cutting was a silicon carbide abrasive wheel, #10-1146 14" X 1/16" X 3/4" Arbor - Grade 1527.

Specimens were cut at a minimum of 50 mm away from the area of interest to be used for imaging. This minimum distance prevented damaged induced in the specimen at the area of interest by the cutting process.

Embedding

The samples were embedded in epoxy to preserve their post-test state during the grinding and polishing process. The epoxy was a two-part EpoxySet¹² manufactured by Allied High Tech Products. The epoxy is shown in Fig. 7.1.

¹¹ <http://www.dynacut.com/diam.htm>

¹² <https://consumables.alliedhightech.com/EpoxySet-p/epxyst.htm>



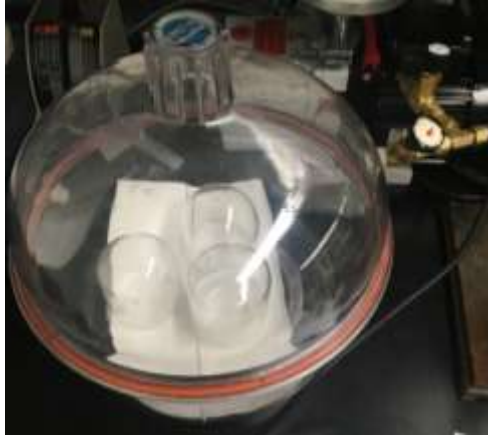
(a)



(b)

Fig. 7.1. Epoxy set components (a) Resin (b) Hardener

The embedding process utilized a vacuum chamber that ensured air bubbles were extracted from the mixed epoxy set. This vacuum chamber is shown in Fig. 7.2(a). The mixed epoxy set was then poured into a cylindrical fixture containing the sample, as shown in Fig. 7.2(b).



(a)



(b)

Fig. 7.2. Epoxy embedding equipment (a) Vacuum chamber (b) Sample holder

Vacuum grease was used in the fixture to allow the embedded sample to be extracted from the fixture once the epoxy had cured.

Grinding and Polishing

Once the epoxy set had cured, the sample was extracted and applied in a grinding and polishing process to prepare it for microscopy. A Multiprep Polishing System¹³ was used to grind the sample to the location near the point of interest and then polish it for detailed microscope images. The Multiprep system is shown in Fig. 7.3(b). The fixture used with this machine is shown in Fig. 7.3(b). This fixture ensured a level viewing surface on the sample.

¹³ <http://www.alliedhightech.com/Equipment/multiprep-polishing-system-8>



(a)



(b)

Fig. 7.3. Grinding and polishing equipment (a) Allied machine specimen holder (b) Allied machine

In addition to silicon carbide discs and water, a few materials were needed for the finer polishing steps. These are shown in Fig. 7.4 and are detailed in Table 7.2.



(a)



(b)



(c)

Fig. 7.4. Polishing materials (a) RedLube (b) Diamond suspension (c) Colloidal silica suspension

Six types of discs were used with the Multiprep machine to reach the area of interest and polish it to the desired level. Each step and its specifications for use with the Multiprep machine are detailed in Table 7.2.

Table 7.2. Grinding and Polishing Procedure

Grinding/ Polishing Step #	Abrasive	Type	Carrier	Coolant	Platen Speed (RPM) / Direction	Force (N)	Time (min)
1	P-800	Silicon Carbide	Abrasive Disc	Water	300/Comp	25	To area of interest
2	P-1200	Silicon Carbide	Abrasive Disc	Water	300/Comp	25	2
3	P-2400	Silicon Carbide	Abrasive Disc	Water	300/Comp	25	2
4	P-4000	Silicon Carbide	Abrasive Disc	Water	300/Comp	25	2
5	1 μm	Diamond	Diamond Suspension ¹⁴	RedLube ¹⁵	150/Comp	30	5
6	0.04 μm	Colloidal Silica	Colloidal Silica Suspension ¹⁶	Water	150/Comp	30	2

*Note: Comp: Platen and sample holder rotate in same direction

As an example of the importance of the polishing process, Fig. 7.5 shows a specimen that has been partly polished. This specimen was slightly un-level, which allowed the right side to be polished well with all six steps from Table 7.2, while the left half was only polished with the first couple of steps.

¹⁴ <https://consumables.alliedhightech.com/Diamond-Suspensions-Polycrystalline-Water-Based-p/diaawtr-poly.htm>

¹⁵ <https://consumables.alliedhightech.com/RedLube-p/redlub.htm>

¹⁶ <https://consumables.alliedhightech.com/Colloidal-Silica-Suspension-Non-Stick-Formula-p/collsil04.htm>

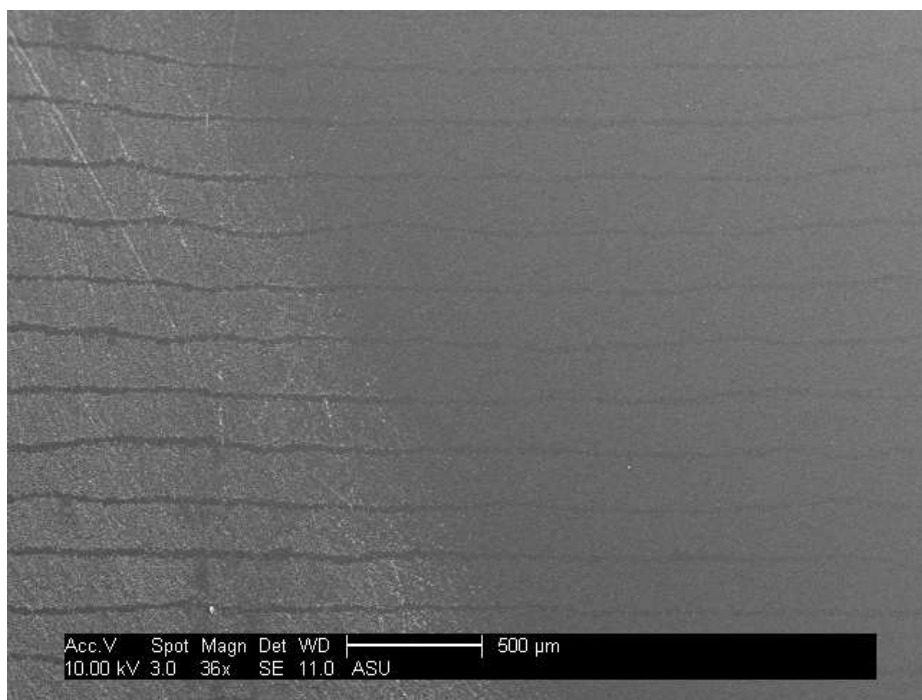


Fig. 7.5. Example of half polished specimen

In Fig. 7.5, the unpolished (left) side shows large scuffs on the surface. These can be seen streaking across the surface of the specimen. The polished (right) side has no such streaks and is smooth throughout.

Imaging

Polished samples were coated with gold/palladium using a Denton Vacuum Desk II Sputter Coater¹⁷. The gold/palladium deposition rate was nearly 10 nm for 120 seconds. The samples were placed in the machine for a duration of 60 seconds to accumulate a deposition of approximately 5 nm. The sputter coater is shown in Fig. 7.6(b).

¹⁷ <https://www.dentonvacuum.com/>

The samples were then examined with a Phillips Environmental Scanning Electron Microscope XL30 ESEM FEG¹⁸. This SEM featured a Schottky Field Emission Source and was used at voltages between 10 and 20 kV. The SEM is shown in Fig. 7.6(a).

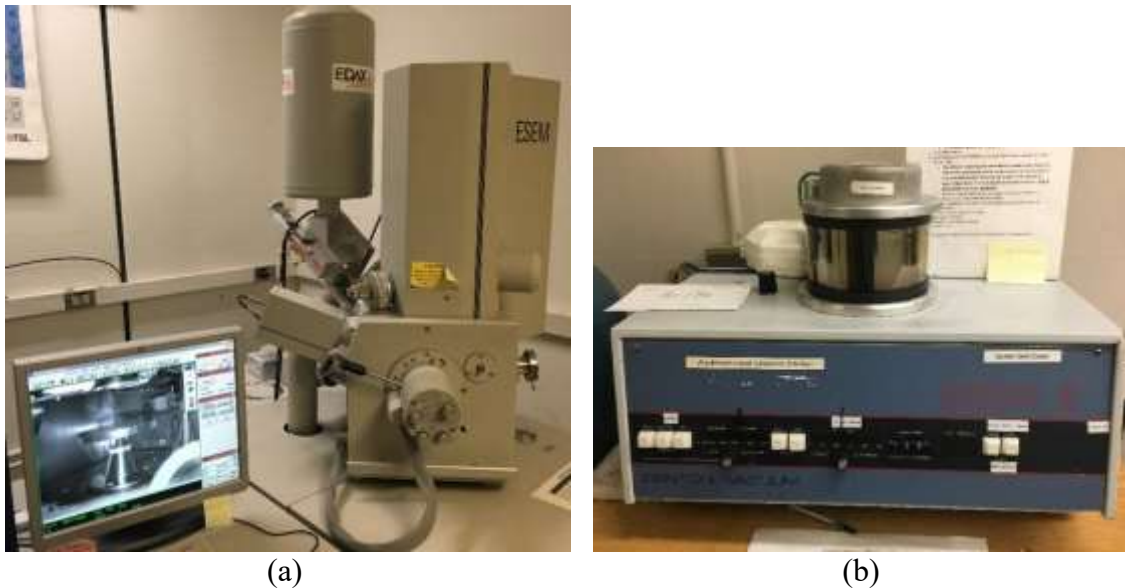


Fig. 7.6. SEM imaging equipment (a) XL30 ESEM FEG (b) Sputter coater

7.3 Results

7.3.1 Virgin Sample

The untested sample before the cutting process is shown in Fig. 7.7.

¹⁸ <https://le-csss.asu.edu/equipment/xl30-environmental-feg-fei>

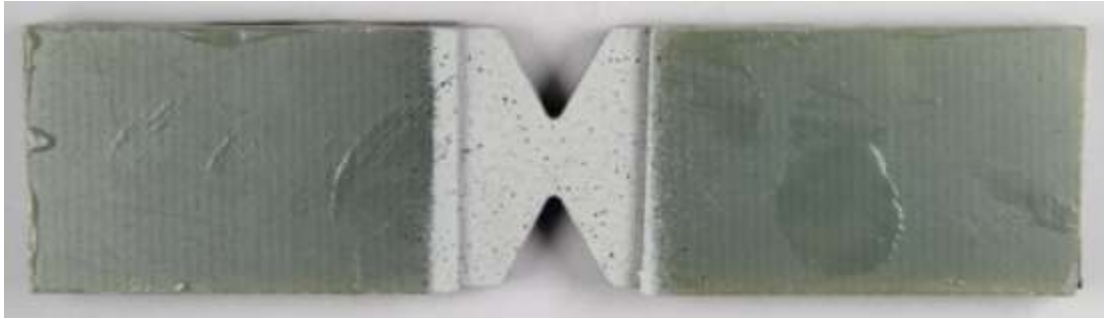


Fig. 7.7. Virgin sample before cutting

The schematic of the cut lines and polishing area is shown in Fig. 7.8. The sample was polished in the hatched region of this figure, up to the imaging plane.

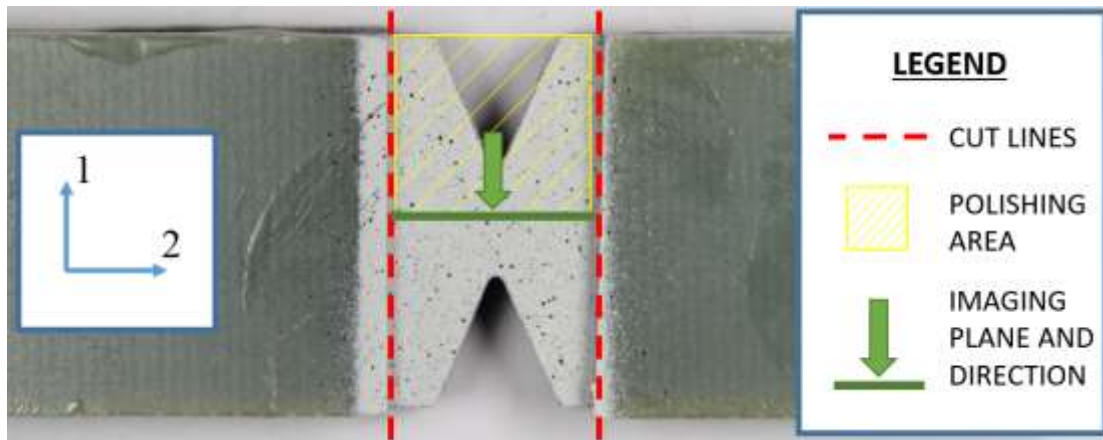


Fig. 7.8. Virgin sample cutting layout

The interface of the interlaminar layer and two layers of the fiber composite is shown in Fig. 7.9. No damage was found in this image.

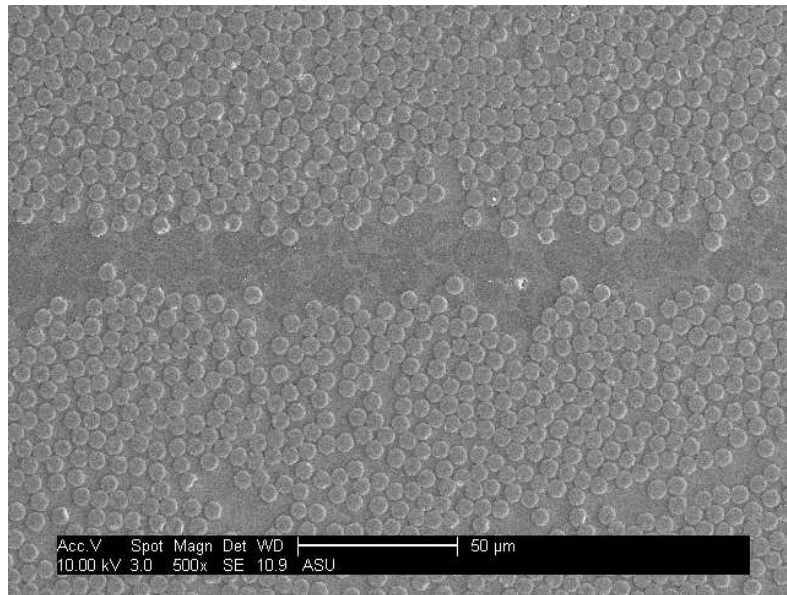
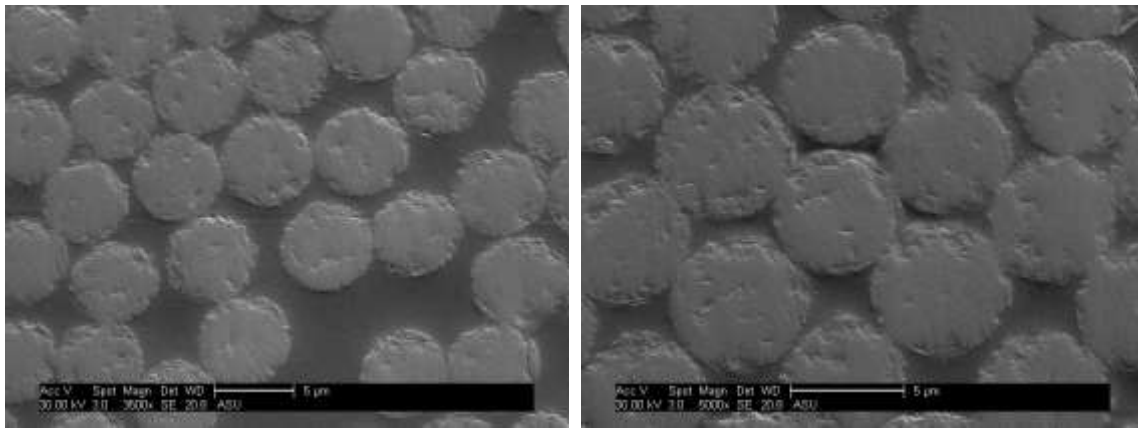


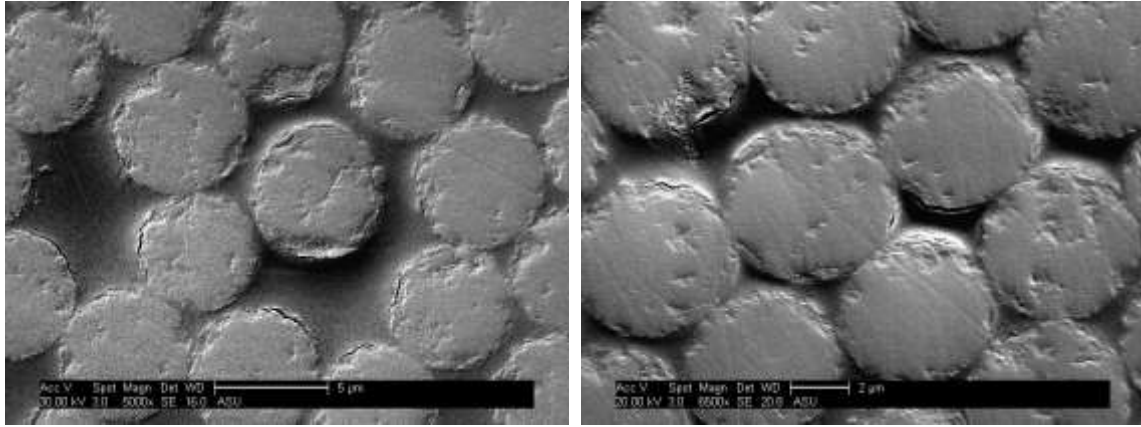
Fig. 7.9. Virgin sample 500x

The majority of the surface area of the viewing plane showed no damage to the fibers or matrix. Fig. 7.10 shows two images of undamaged areas of the sample at different magnifications.



(a) (b)
Fig. 7.10. Virgin sample (a) 3500x (b) 5000x

Though it was uncommon, there were some areas of the virgin sample that showed damage. The only damage visible on the sample was interfacial damage between fibers and matrix. Fiber debonding is shown in Fig. 7.11.



(a) (b)
Fig. 7.11. Virgin sample (a) 5000x (b) 6500x

Though there was debonding as shown in the images of Fig. 7.11, the maximum portion of the perimeter debonded was approximately 1/8 of the total perimeter of the fiber. The debonding ratio refers to the ratio of the fiber perimeter length that is still bonded with the surrounding matrix to the fiber perimeter length that has become detached with the surrounding matrix. Thus, the fibers in Fig. 7.11 have a maximum debonding ratio of 1/8 or 12.5%. It was undetermined whether this damage was inflicted during the manufacturing process or during the grinding and polishing of the sample. In either case, the virgin sample established a baseline for the amount of damage expected to be seen in an untested specimen.

7.3.2 Damaged Sample

The post-test sample before the cutting process is shown in Fig. 7.12.

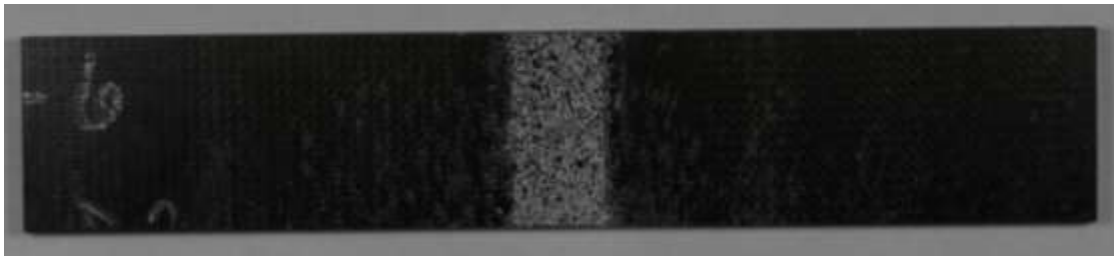


Fig. 7.12. Damaged sample before cutting

The schematic of the cut lines and polishing area is shown in Fig. 7.13. The sample was polished in the hatched region of this figure, up to the imaging plane.

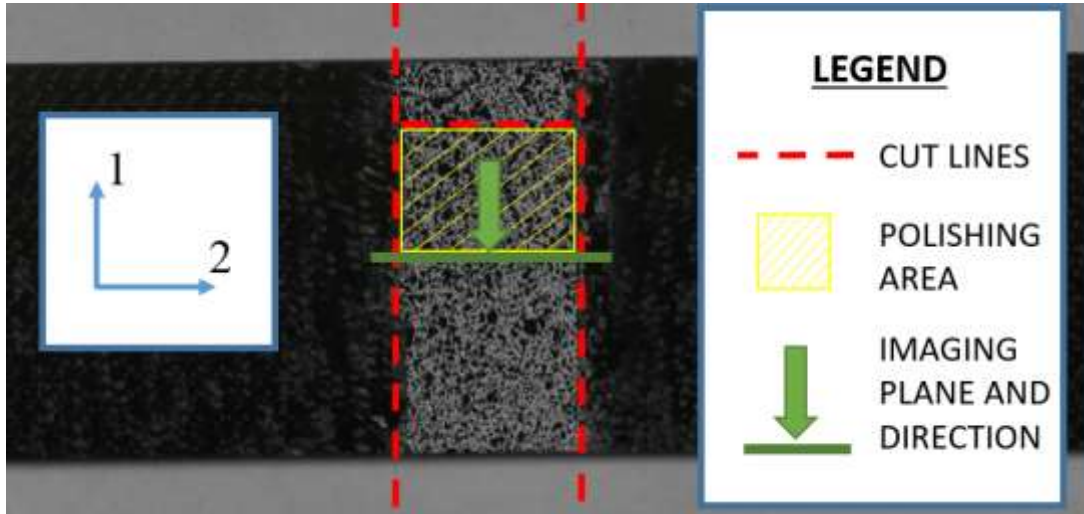
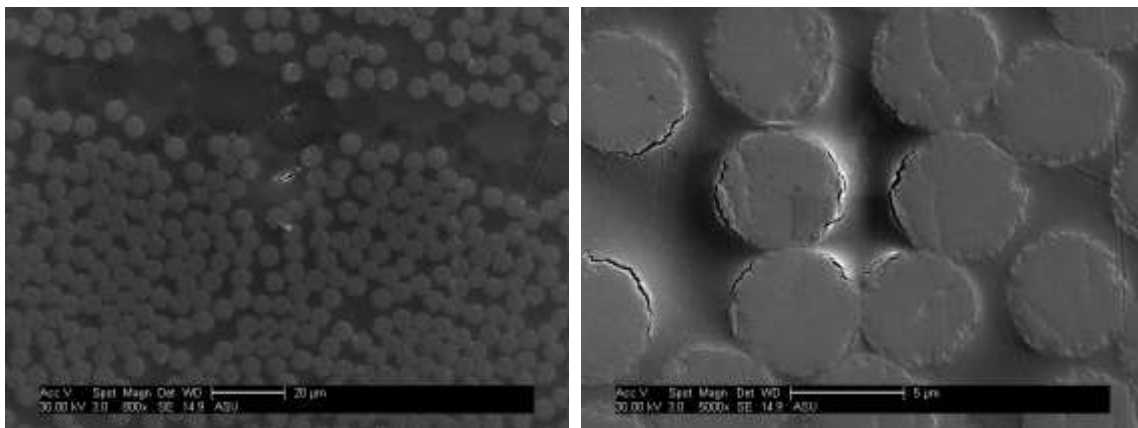


Fig. 7.13. Damaged sample cutting layout

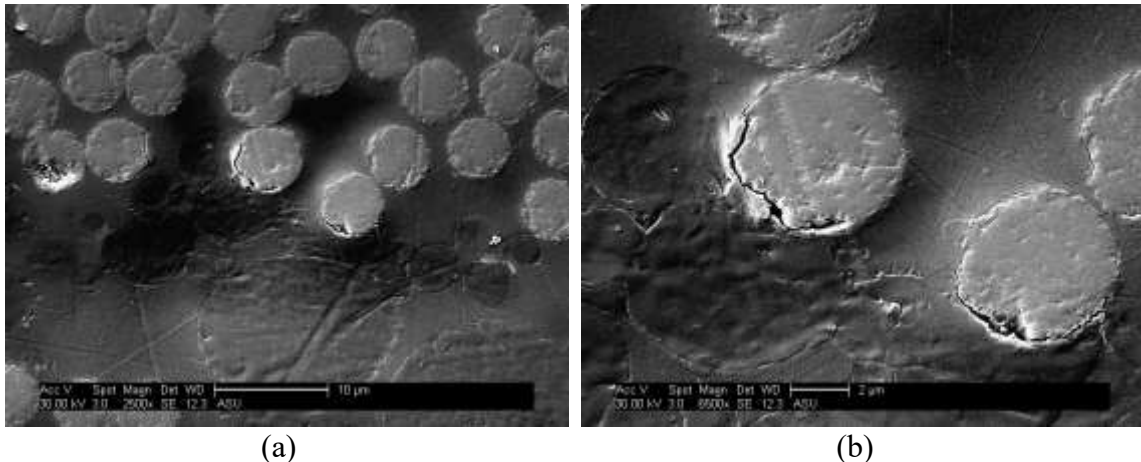
This sample showed more frequent and higher degree damage than the virgin sample in some areas, but the majority of the surface area of the imaging plane still showed no damage. The types of damage seen in the damaged sample were fiber debonding and matrix cracking



(a) (b)
Fig. 7.14. Damaged sample (a) 800x (b) 5000x

Fig. 7.14(a) shows a small crack that had formed near the interlaminar layer. The crack is near the center of the image and is highlighted in white due to a charging effect of the SEM. Fig. 7.14(b) shows an example found in the sample of fiber debonding. Comparing the fiber debonding in this image to that of Fig. 7.11, it can be seen that the damaged sample sustained a larger degree of fiber debonding from the surrounding matrix. Some of these fibers had a debonding ratio of nearly 1/2 with the entire perimeter.

Fig. 7.15 shows another example of fiber debonding that appeared to be more extensive than the fiber debonding of the virgin sample.



(a) (b)
Fig. 7.15. Damaged sample (a) 2500x (b) 6500x

The images of Fig. 7.15 depict the same feature, with (a) providing a more magnified view. This image shows one of the fibers had debonded with a ratio of approximately 1/2 from the entire fiber perimeter.

7.3.3 Failed Sample

The post-test sample before the cutting process is shown in Fig. 7.16.

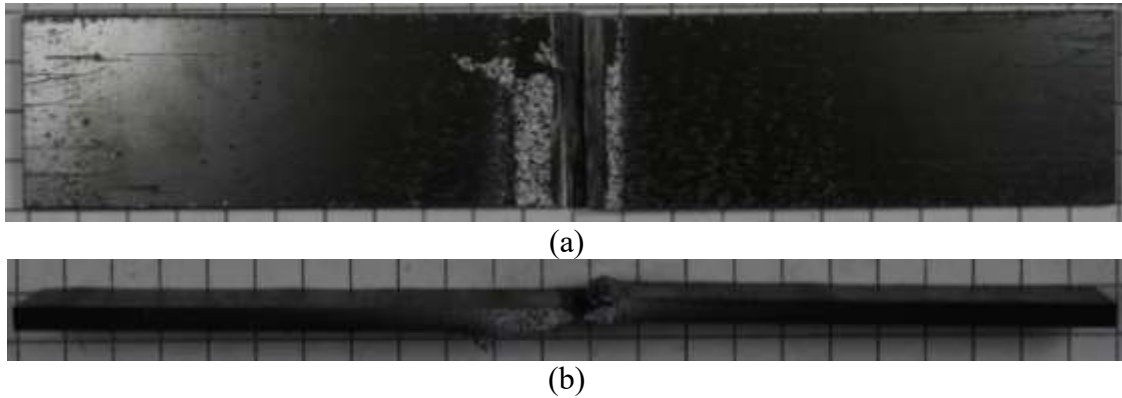


Fig. 7.16. Failed sample before cutting (a) Width (b) Through thickness

The schematic of the cut lines and polishing area is shown in Fig. 7.17. The sample was polished in the hatched region of this figure, up to the imaging plane. This specimen was completely fractured, thus there were two pieces that were used for imaging.

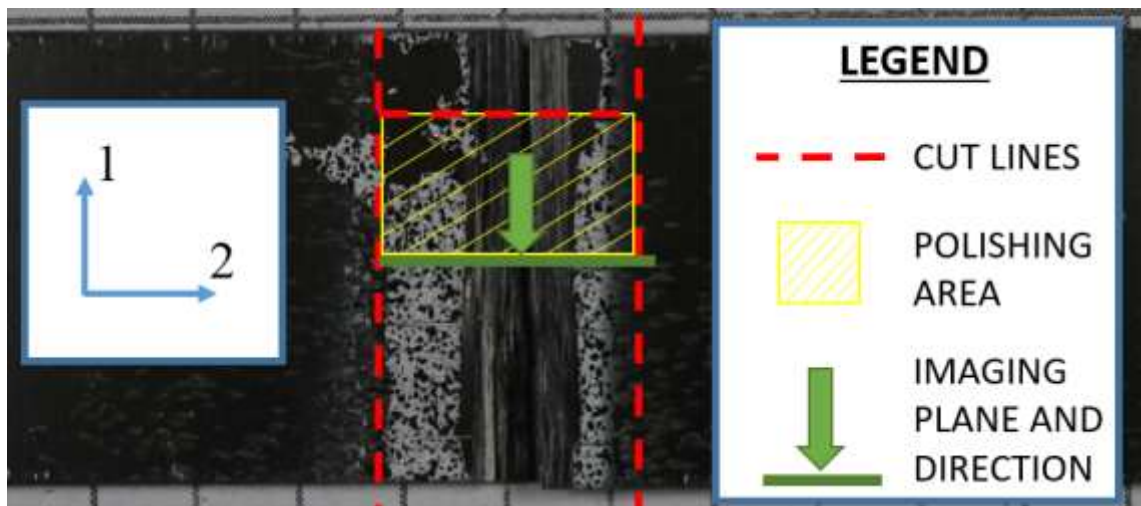


Fig. 7.17. Failed sample cutting layout

Fig. 7.18 shows the failed sample at the location near one of the cut lines from Fig. 7.17. The image shows that a large crack formed and propagated almost entirely through the thickness of the specimen. Some of the crack filled with epoxy during the

specimen embedding process. Air voids in the epoxy during curing left some of the crack void of any material (these are the darker spots surrounded by a white layer in Fig. 7.18). The original test of this coupon was a 2-direction compression test, thus this large crack may have formed as a result of buckling of the composite.

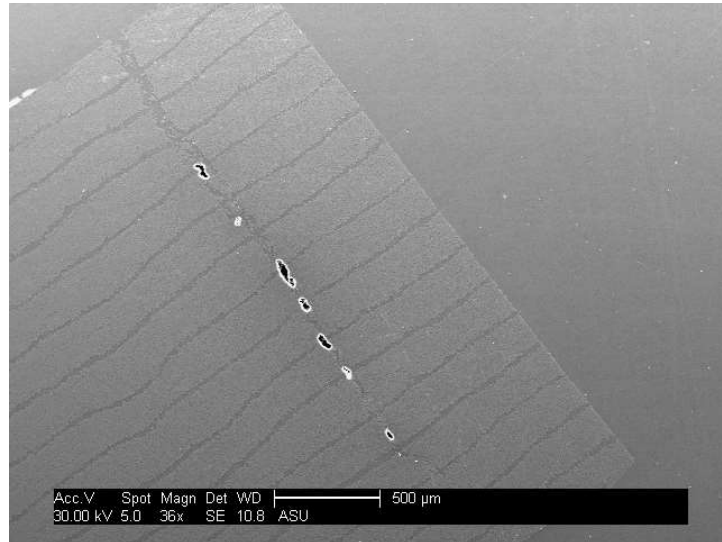


Fig. 7.18. Failed sample 36x damage away from complete fracture zone

The failed specimen showed extensive damage of all kinds. Matrix damage included large cracks and openings between fibers, both interlaminar and intralaminar. Fig. 7.19 shows extensive matrix damage. Fig. 7.19(a) shows a large crack and opening occurring as intralaminar matrix damage. Fig. 7.19(b) shows a variety of inter and intralaminar cracking.

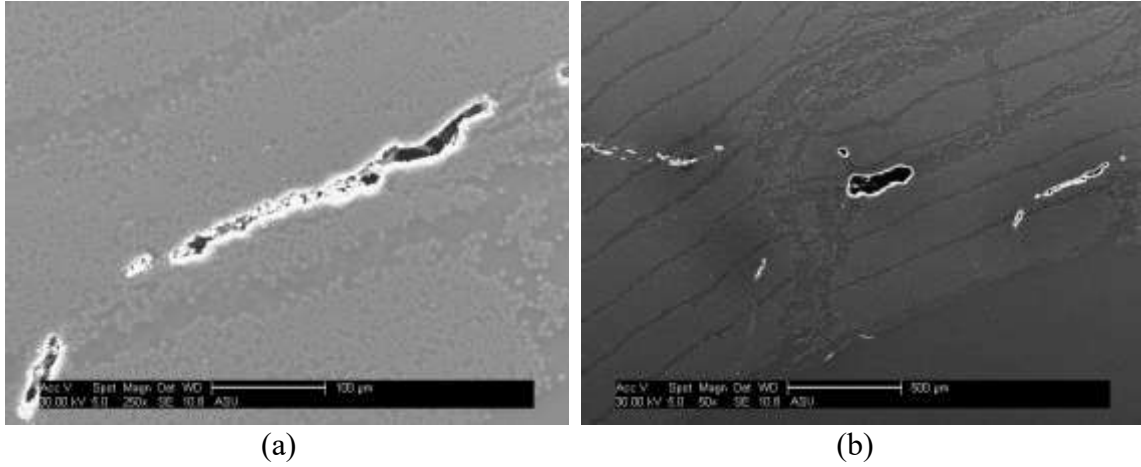


Fig. 7.19. Failed sample (a) 250x (b) 50x

Large cracks also formed perpendicular to the composite layers and extended over multiple layers. Fig. 7.20 shows this perpendicular crack formation.

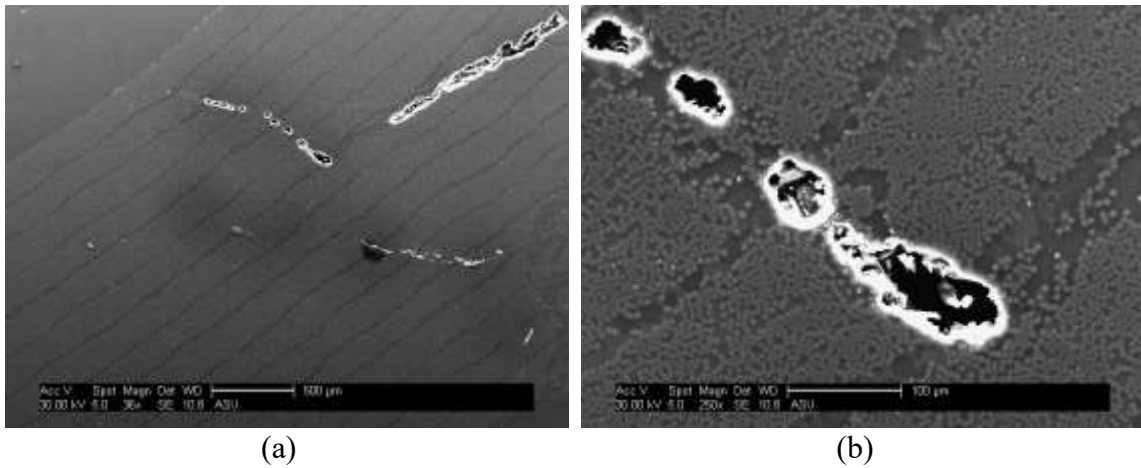


Fig. 7.20. Failed sample (a) 36x (b) 250x

In addition to the cracks that formed large openings between fibers. Matrix cracking also occurred that took the form of thin cracks between fibers. Fig. 7.21 shows this type of matrix crack. Fig. 7.21(a) depicts the crack from a lower magnification and shows that it is parallel with the composite layers. Fig. 7.21(b) shows the crack at a

higher magnification. This figure shows that the crack primarily winds around fibers, but there are some fibers which the crack splits.

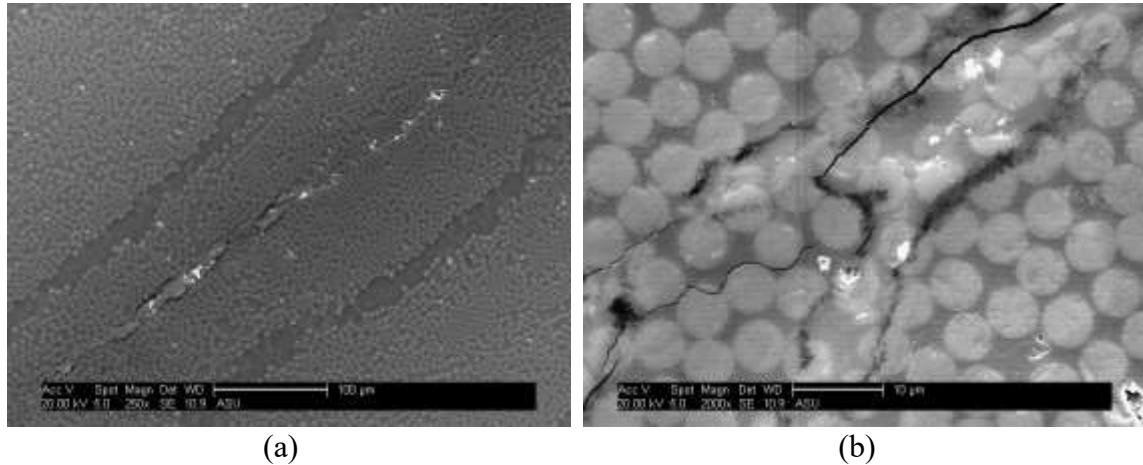


Fig. 7.21. Failed sample (a) 250x (b) 2000x

This thin type of crack shown in Fig. 7.21 as occurring parallel to the composite layers also occurred at an angle to the composite layers. Fig. 7.22 shows a think crack at different levels of magnification that occurred at an angle of approximately 45° to the composite layers.

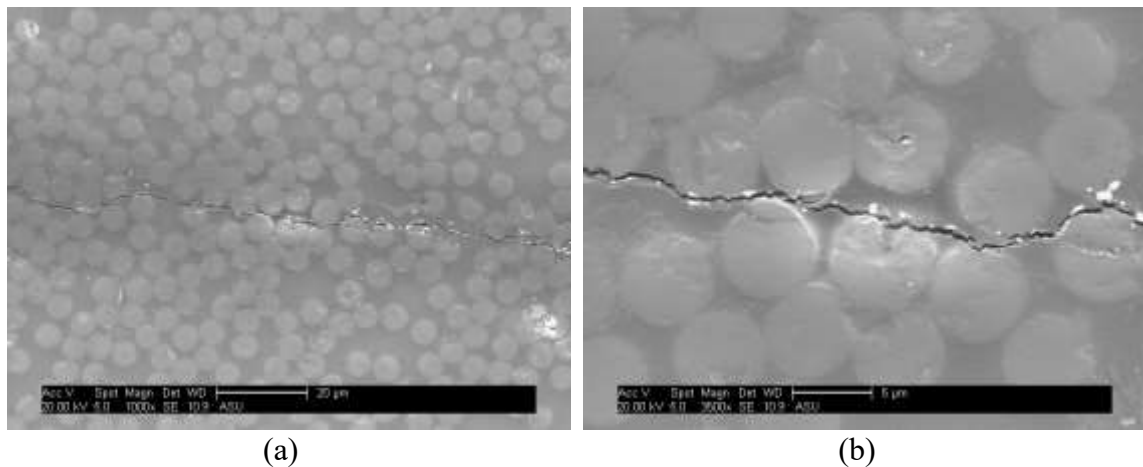


Fig. 7.22. Failed sample (a) 1000x (b) 3500x

The angle of the crack in Fig. 7.22 is known because it was taken at the same angle with the composite as in Fig. 7.21, where the layers are approximately at a 45° angle with the image frame. Since the crack shown in Fig. 7.22 is nearly horizontal compared to the image frame, the crack and composite layers were approximately at a 45° angle with each other.

7.3.4 Failed – Shear Sample

The post-test sample before the cutting process is shown in Fig. 7.23.

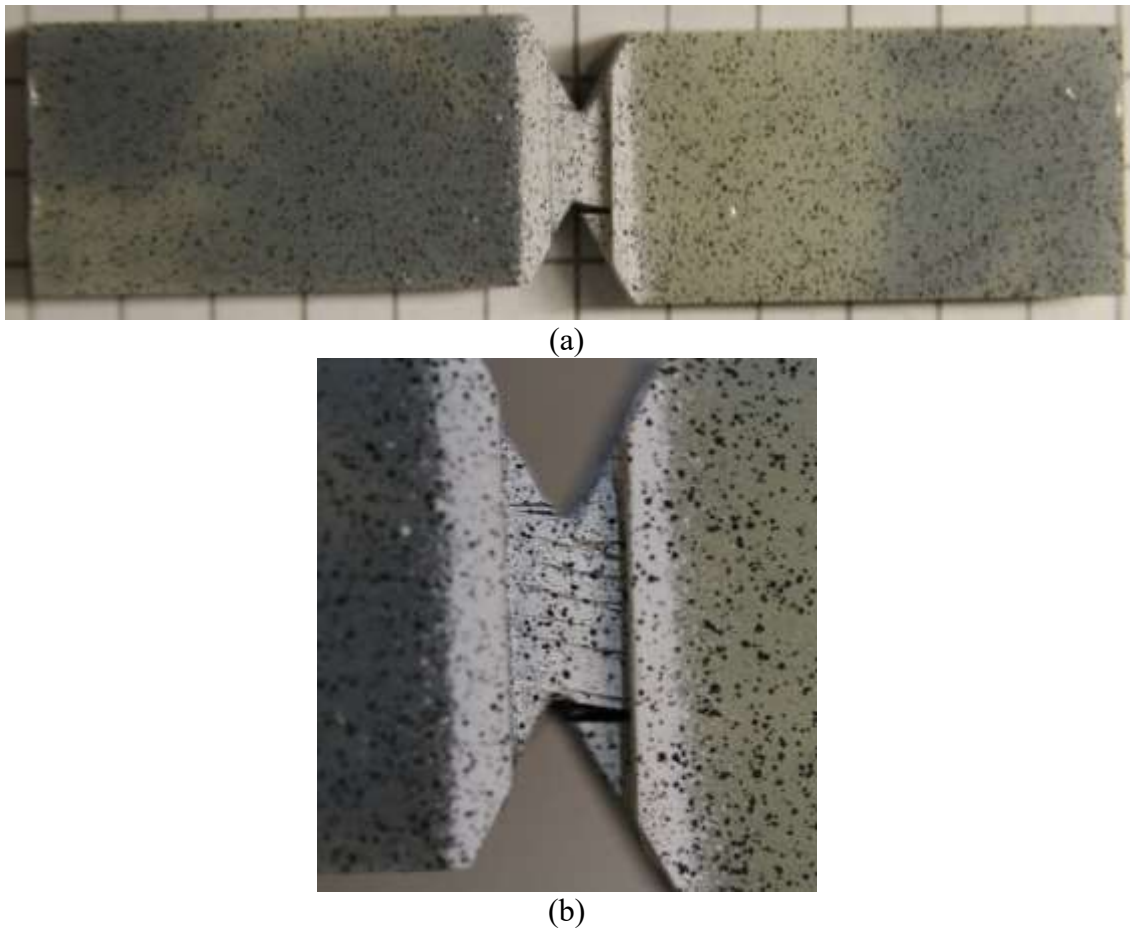


Fig. 7.23. Failed-shear sample before cutting (a) Whole specimen (b) Gage area

The schematic of the cut lines and polishing area is shown in Fig. 7.24. The sample was polished in the hatched region of this figure, up to the imaging plane.

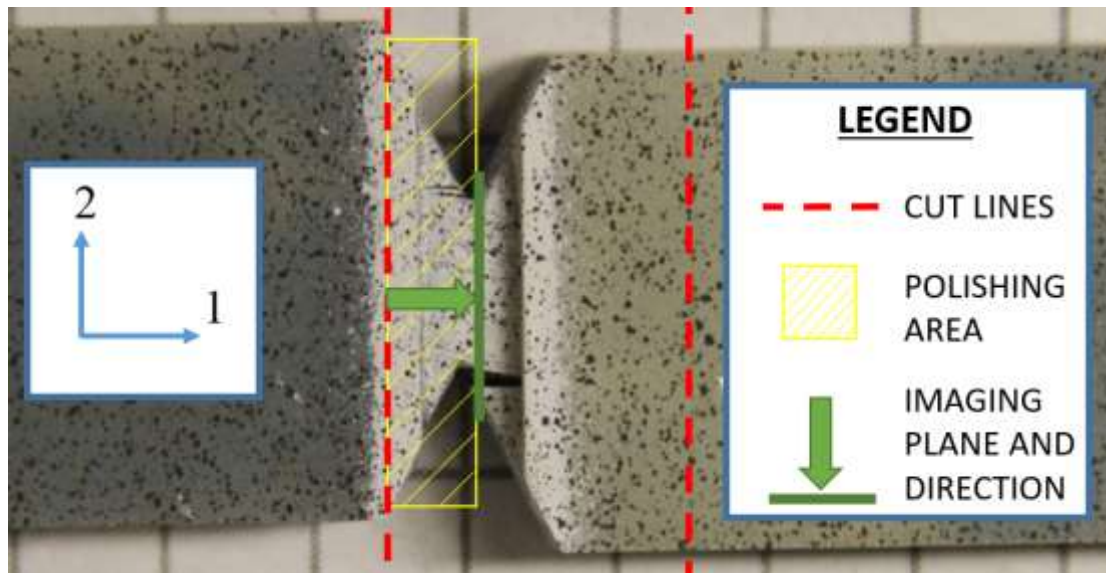
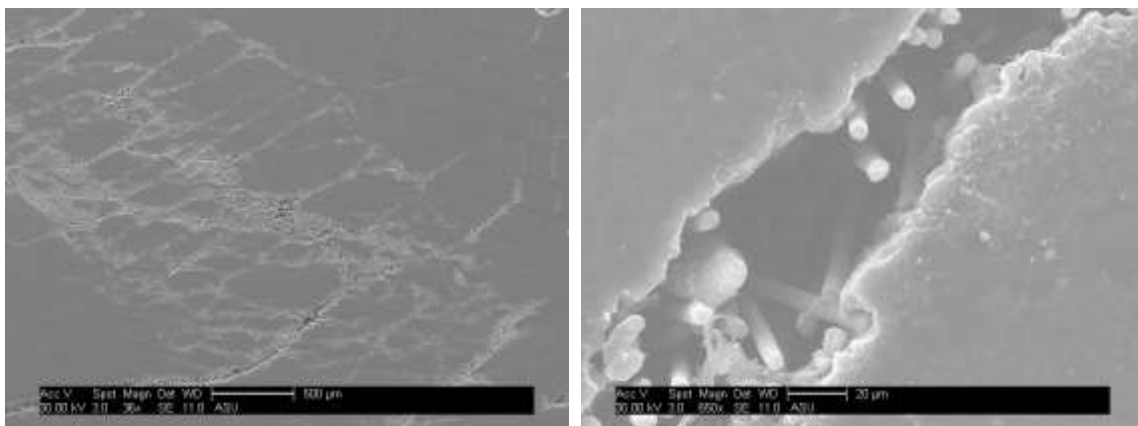


Fig. 7.24. Failed-shear sample cutting layout

The failed-shear sample showed extensive damage in different forms than the other specimens. Fig. 7.25(a) shows the overall specimen with an overall damage pattern at an approximately 30° angle with the composite layers. Extensive interlaminar matrix cracking is shown at a low magnification. Fig. 7.25(b) shows that unlike the other test coupons, the fiber orientation changed during the test. Instead of only seeing the top surface of the fibers, they are seen to be at an angle with the image and extend into the image to some depth.



(a) (b)
Fig. 7.25. Failed-shear sample (a) 36x (b) 650x

Fig. 7.26 shows more examples of fibers skewed at an angle. Generally the fibers appear to be skewed parallel with the composite layers. This was towards the direction of loading during the shear test.

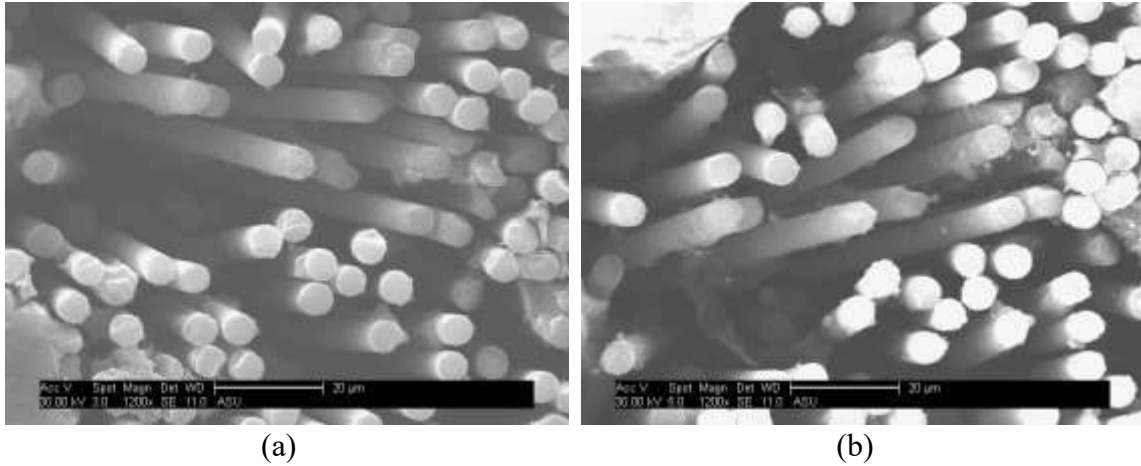
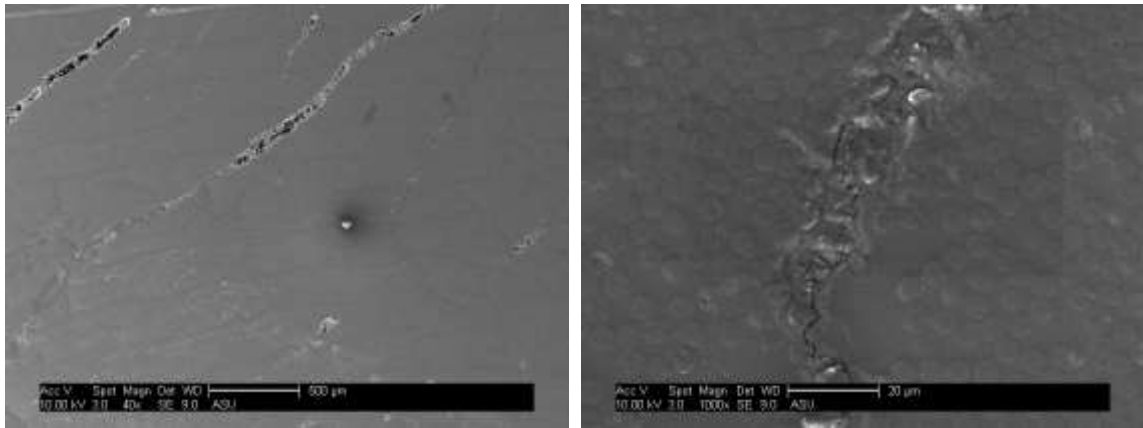


Fig. 7.26. Failed-shear sample (a) 1200x (b) 1200x

The skewed angle of the fibers was expected as the material strength of the composite increased near the end of the shear test. The expectation was that the fibers were re-orientated so that they were in tension at the end of the test. This theory was confirmed with the images of Fig. 7.25 and Fig. 7.26.

Matrix cracking was another type of damage seen extensively in the failed-shear specimen. Fig. 7.27 depicts matrix cracking that led to large openings between fibers (Fig. 7.27(a)) and thin matrix cracking winding between fibers (Fig. 7.27(b)).



(a) (b)
Fig. 7.27. Failed-shear sample (a) 40x (b) 1000x

8. Concluding Remarks

This report summarized the details of the stacked-ply validation tests for MAT213 conducted at room temperature and at quasi-static loading conditions. Comparison metrics between experimental and simulated results included stress-strain relationships, strain profiles, and displacements.

Higher magnitude stresses and strains induced in the direction of loading were well predicted by MAT213 simulations. Lower magnitude strains induced in the transverse direction showed larger differences when compared to MAT213 simulations. In some cases, the MAT213 simulated results under predicted transverse strains measured in the experiments.

Initiation G_C values were obtained from ENF and DCB tests for mode I and mode II fracture of the interlaminar layers of the fiber reinforced material. Pre-cracked values were used from both tests as the critical energy release rate in cohesive zone models for interlaminar layers. The average experimental G_{IIC} value from the ENF tests was 10.50 psi-in. The average experimental G_{IC} value from the DCB test was 2.65 psi-in using the maximum load definition of crack initiation and the compliance calibration method of calculation. The ENF and DCB tests were modeled in LS-DYNA and used to calibrate other cohesive zone parameters to match experimental data.

SEM analysis revealed that some damage existed in untested specimens from either the manufacturing process or from grinding and polishing of the sample. However, a sample from a test coupon of the damage characterization tests revealed that there was more damage in this specimen in the form of matrix cracking and fiber interface decohesion.

References

1. Goldberg Robert K.; Carney Kelly S.; DuBois Paul; Hoffarth Canio; Harrington Joseph; Rajan Subramaniam; Blankenhorn Gunther Development of an Orthotropic Elasto-Plastic Generalized Composite Material Model Suitable for Impact Problems. *J. Aerosp. Eng.* **2016**, *29*, 04015083, doi:10.1061/(ASCE)AS.1943-5525.0000580.
2. Harrington Joseph; Hoffarth Canio; Rajan Subramaniam D.; Goldberg Robert K.; Carney Kelly S.; DuBois Paul; Blankenhorn Gunther Using Virtual Tests to Complete the Description of a Three-Dimensional Orthotropic Material. *J. Aerosp. Eng.* **2017**, *30*, 04017025, doi:10.1061/(ASCE)AS.1943-5525.0000737.
3. Hoffarth, C.; Rajan, S. D.; Goldberg, R. K.; Revilock, D.; Carney, K. S.; DuBois, P.; Blankenhorn, G. Implementation and validation of a three-dimensional plasticity-based deformation model for orthotropic composites. *Compos. Part Appl. Sci. Manuf.* **2016**, *91*, 336–350, doi:10.1016/j.compositesa.2016.10.024.
4. Bruyneel, M.; Delsemme, J. P.; Goupil, A. C.; Jetteur, P.; Lequesne, C.; Naito, T.; Urushiyama, Y. DAMAGE MODELING OF LAMINATED COMPOSITES: VALIDATION OF THE INTRA_LAMINAR LAW OF SAMCEF AT THE COUPON LEVEL FOR UD PLIES. **2014**, *9*.
5. Ladeveze, P.; LeDantec, E. Damage modelling of the elementary ply for laminated composites. *Compos. Sci. Technol.* **1992**, *43*, 257–267, doi:10.1016/0266-3538(92)90097-M.
6. Achard, V.; Bouvet, C.; Castanié, B.; Chirol, C. Discrete ply modelling of open hole tensile tests. *Compos. Struct.* **2014**, *113*, 369–381, doi:10.1016/j.compstruct.2014.03.031.
7. Clay, S. B.; Knoth, P. M. Experimental results of quasi-static testing for calibration and validation of composite progressive damage analysis methods. *J. Compos. Mater.* **2017**, *51*, 1333–1353, doi:10.1177/0021998316658539.
8. Zabala, H.; Aretxabaleta, L.; Castillo, G.; Aurrekoetxea, J. Dynamic 4 ENF test for a strain rate dependent mode II interlaminar fracture toughness characterization of unidirectional carbon fibre epoxy composites. *Polym. Test.* **2016**, *55*, 212–218, doi:10.1016/j.polymertesting.2016.09.001.
9. Kageyama, K.; Kikuchi, M.; Yanagisawa, N. Stabilized End Notched Flexure Test: Characterization of Mode II Interlaminar Crack Growth. In *Composite Materials: Fatigue and Fracture (Third Volume)*; ASTM International, West Conshohocken, PA, 1991; pp. 210–225.
10. Schuecker, C.; Davidson, B. Effect of Friction on the Perceived Mode II Delamination Toughness from Three- and Four-Point Bend End-Notched Flexure

Tests. In *Composite Structures: Theory and Practice*; Grant, P., Rousseau, C., Eds.; ASTM International: 100 Barr Harbor Drive, PO Box C700, West Conshohocken, PA 19428-2959, 2001; pp. 334-334–11 ISBN 978-0-8031-2862-0.

11. O'Brien, T. K.; Johnston, W. M.; Toland, G. J. *Mode II Interlaminar Fracture Toughness and Fatigue Characterization of a Graphite Epoxy Composite Material*; 2010;
12. *ASTM D5528-13 Standard Test Method for Mode I Interlaminar Fracture Toughness of Unidirectional Fiber-Reinforced Polymer Matrix Composites*; ASTM International, West Conshohocken, PA, 2013;
13. Yoshihara, H.; Satoh, A. Shear and crack tip deformation correction for the double cantilever beam and three-point end-notched flexure specimens for mode I and mode II fracture toughness measurement of wood. *Eng. Fract. Mech.* **2009**, *76*, 335–346, doi:10.1016/j.engfracmech.2008.10.012.
14. Sun, C. T.; Zheng, S. Delamination characteristics of double-cantilever beam and end-notched flexure composite specimens. *Compos. Sci. Technol.* **1996**, *56*, 451–459, doi:10.1016/0266-3538(96)00001-2.
15. Nuggehalli Nandakumar, P. Rate sensitivity of the interlaminar fracture toughness of laminated composites. Thesis, Wichita State University, 2010.
16. Tamuzs, V.; Tarasovs, S.; Vilks, U. Progressive delamination and fiber bridging modeling in double cantilever beam composite specimens. *Eng. Fract. Mech.* **2001**, *68*, 513–525, doi:10.1016/S0013-7944(00)00131-4.
17. Wasseem H.S., M.; Kumar N., K. FEM for Delamination Analysis of Double Cantilever Beam | Fracture Mechanics | Fracture Available online: <https://www.scribd.com/document/270149618/FEM-for-Delamination-Analysis-of-Double-Cantilever-Beam> (accessed on Jun 27, 2018).
18. Experimental Calibration of Cohesive Zone Models Available online: <http://www.veryst.com/project/cohesive-zone-model-calibration> (accessed on Jun 27, 2018).
19. Arrese, A.; Boyano, A.; De Gracia, J.; Mujika, F. A novel procedure to determine the cohesive law in DCB tests. *Compos. Sci. Technol.* **2017**, *152*, 76–84, doi:10.1016/j.compscitech.2017.09.012.
20. Meo, M.; Thieulot, E. Delamination modelling in a double cantilever beam. *Compos. Struct.* **2005**, *71*, 429–434, doi:10.1016/j.compstruct.2005.09.026.
21. Jollivet, T.; Peyrac, C.; Lefebvre, F. Damage of Composite Materials. *Procedia Eng.* **2013**, *66*, 746–758, doi:10.1016/j.proeng.2013.12.128.

22. LLorca, J.; González, C.; Molina-Aldareguía, J. M.; López, C. S. Multiscale Modeling of Composites: Toward Virtual Testing ... and Beyond. *JOM* **2013**, *65*, 215–225, doi:10.1007/s11837-012-0509-8.
23. Li, Q.; Zhao, X.; Xu, S.; Leung, C. K.; Wang, B. Multiple impact resistance of hybrid fiber ultra high toughness cementitious composites with different degrees of initial damage.
24. Schmidt, N. Experimental Procedures and Data Analysis of Orthotropic Composites, Arizona State University: Tempe, AZ, 2016.
25. Correlated Solutions Available online: <http://correlatedsolutions.com/> (accessed on Jun 27, 2018).
26. *ASTM D3039/D3039M-17 Standard Test Method for Tensile Properties of Polymer Matrix Composite Materials*; ASTM International, West Conshohocken, PA, 2017;
27. *ASTM D6641/D6641M-16e1 Standard Test Method for Compressive Properties of Polymer Matrix Composite Materials Using a Combined Loading Compression (CLC) Test Fixture*; ASTM International, West Conshohocken, PA, 2016;
28. *ASTM D3410/D3410M-16 Standard Test Method for Compressive Properties of Polymer Matrix Composite Materials with Unsupported Gage Section by Shear Loading*; ASTM International, West Conshohocken, PA, 2016;
29. *ASTM D5766/D5766M-11 Standard Test Method for Open-Hole Tensile Strength of Polymer Matrix Composite Laminates*; ASTM International, West Conshohocken, PA, 2011;
30. *ASTM D6484/D6484M-14 Standard Test Method for Open-Hole Compressive Strength of Polymer Matrix Composite Laminates*; ASTM International, West Conshohocken, PA, 2014;
31. LIVERMORE SOFTWARE TECHNOLOGY CORPORATION LS-DYNA KEYWORD USER'S MANUAL VOLUME II Material Models.
32. T. C. M. America Available online: <https://www.toraycma.com>.
33. *ASTM D7905/D7905M-14 Standard Test Method for Determination of the Mode II Interlaminar Fracture Toughness of Unidirectional Fiber-Reinforced Polymer Matrix Composites*; ASTM International, West Conshohocken, PA, 2014;
34. Deivanayagam A.; Vaidya A.; Rajan S. D. Enhancements to Modeling Dry Fabrics for Impact Analysis. *J. Aerosp. Eng.* **2014**, *27*, 484–490, doi:10.1061/(ASCE)AS.1943-5525.0000350.

35. Khaled, B.; Shyamsunder, L.; Schmidt, N.; Hoffarth, C.; Rajan, S. *Experimental Tests to Characterize the Behavior and Properties of T800-F3900 Toray Composite*; Arizona State University;
36. Sasser, D. Structural Analysis of Carbon Fiber-Epoxy Composite Surfaces with Polar Stacking Sequences. Thesis, 2015.
37. Hongkarnjanakul, N.; Bouvet, C.; Rivallant, S. Validation of low velocity impact modelling on different stacking sequences of CFRP laminates and influence of fibre failure. *Compos. Struct.* **2013**, *106*, 549–559, doi:10.1016/j.compstruct.2013.07.008.
38. Serra, J.; Pierré, J. E.; Passieux, J. C.; Périé, J. N.; Bouvet, C.; Castanié, B.; Petiot, C. Validation and modeling of aeronautical composite structures subjected to combined loadings: The VERTEX project. Part 2: Load envelopes for the assessment of panels with large notches. *Compos. Struct.* **2017**, *180*, 550–567, doi:10.1016/j.compstruct.2017.08.055.
39. León Becerra, J.; González-Estrada, O. A.; Pertuz, A. Influence of the boundary condition on the first ply failure and stress distribution on a multilayer composite pipe by the finite element method. 2017.
40. Chiu, L. N. S.; Falzon, B. G.; Chen, B.; Yan, W. Validation of a 3D damage model for predicting the response of composite structures under crushing loads. *Compos. Struct.* **2016**, *147*, 65–73, doi:10.1016/j.compstruct.2016.03.028.